May 2019

Photo-Physical Properties of Novel GUMBOS for Optoelectronic Applications

Thenahandi Prasanthi Deepthika De Silva
Louisiana State University and Agricultural and Mechanical College

PHOTO-PHYSICAL PROPERTIES OF NOVEL GUMBOS FOR OPTOELECTRONIC APPLICATIONS

A Dissertation

Submitted to the Graduate Faculty of the
Louisiana State University and
Agricultural and Mechanical College
in partial fulfillment of the
requirements for the degree of
Doctor of Philosophy

in

The Department of Chemistry

by
Thenahandi Prasanthi Deepthika De Silva
B.Sc., University of Kelaniya, Kelaniya, 2006
M.Sc., University of Sri Jayewardenepura, Sri Jayewardenepura, 2011
M.Sc., Sam Houston State University, Huntsville, 2013
August 2019

Dedicated to:

My parents Ananda and Elizabeth De Silva,

My loving husband David A. Donkor,

My parents-in-law Samuel and Juliana Donkor

My sisters Kanchana and Esther

My brother Daniel

My good friends Sky and Alain

My relatives, friends, and well-wishers

ACKNOWLEDGEMENTS

I am deeply appreciative and grateful to,

- Prof. Isiah M. Warner, for the excellent mentorship, guidance, encouragement, and financial support provided for my research. The experiences that I have gained in the Warner laboratory will tremendously help me to succeed in my future endeavors.
- My collaborators, for helping me to explore new horizons and for their invaluable contributions. Particularly, I am very grateful for the contributions of Dr. Evgueni E. Nesterov, Dr. Sang Gil Youm, Dr. George G. Tamas, Dr. Boqian Yang, Dr. Frank R. Fronczek, and Chun-Han Wang.
- Dissertation committee members, Dr. Megan A. Macnaughtan, Dr. Louis H. Haber, and Dr. Tammy R. Dugas for their constant support and guidance.
- Polymer analysis laboratory and shared instrumental facility, LSU, for providing resources to perform TGA, DSC, and PXRD experiments.
- Warner group post-docs, past and present, for continuous support in numerous forms including proofreading, providing different forms of valuable advice, and for knowledge-sharing.
- Warner group members, past and present, for valuable discussions and suggestions.
- National Aeronautics and Space Administration (NASA), National Science Foundation (NSF), and Louisiana State University Leveraging Innovation for Technology Transfer ($LIFT^2$) program for financial support.
- My family and friends for their emotional, moral, and financial support.

TABLE OF CONTENTS

ACKNOWLEDGEMENTS iii

LIST OF TABLES vi

LIST OF FIGURES vii

LIST OF SYMBOLS AND ABBREVIATIONS x

ABSTRACT xiv

CHAPTER I. INTRODUCTION 1
1.1. Organic Light Emitting Diodes (OLEDs) - A Brief Overview 1
1.2. Working Principle of OLEDs 4
1.3. OLED Classification 5
1.4. Blue Emitters in OLED Displays 7
1.5. Exciton Harvesting Mechanisms 8
1.6. Molecular Design 11
1.7. EML Design 15
1.8. OLED Fabrication 17
1.9. Analytical Techniques Used in This Research 19
1.10. The Scope of this Dissertation 29
1.11. References 30

CHAPTER II. PYRENYLPYRIDINES: SKY-BLUE EMITTERS FOR ORGANIC LIGHT EMITTING DIODES 38
2.1. Introduction 38
2.2. Experimental Section 41
2.3. Synthesis and Characterization 44
2.4. Results and Discussion 45
2.5. Conclusions 60
2.6. References 61

CHAPTER III. PYRENE-BENZIMIDAZOLE DERIVATIVES AS NOVEL BLUE EMITTERS FOR OLEDS 66
3.1. Introduction 66
3.2. Experimental Section 69
3.3. Synthesis and Characterization 71
3.4. Results and Discussion 72
3.5. Conclusions 86
3.6. References 87

CHAPTER IV. INFLUENCE OF ANION VARIATIONS ON PHOTO-PHYSICAL PROPERTIES OF THE PROPIDIUM LUMINOPHORE 92
4.1. Introduction 92

4.2. Experimental Section 95
4.3. Synthesis and Characterization. 96
4.4. Results and Discussion 98
4.5. Conclusions 110
4.6. References 111

CHAPTER V. CONCLUSIONS AND FUTURE WORK 119

APPENDIX A. SUPPORTING INFORMATION FOR CHAPTER 2 119

APPENDIX B. SUPPORTING INFORMATION FOR CHAPTER 3 125

APPENDIX C. SUPPORTING INFORMATION FOR CHAPTER 4 130

APPENDIX D. LETTERS OF PERMISSION 139

VITA 140

LIST OF TABLES

Table 2.1. Summary of conformational and thermal properties of pyrenylpyridines. 47

Table 2.2. Absorption data for pyrenylpyridines. 53

Table 2.3. Summary of emission properties of pyrenylpyridines. 54

Table 2.4. Quantum yields and fluorescence lifetimes of pyrenylpyridines. 56

Table 2.5. Electronic properties of pyrenylpyridines 58

Table 3.1. Thermal decomposition onset temperatures (T_{onset}) of compounds A, B, and C. 77

Table 3.2. Absorption data summary for compounds A, B, and C. 79

Table 3.3. Summary of emission properties of compound A, B, and C. 81

Table 3.4. Quantum yields and lifetimes of compounds A, B, and C. 82

Table 3.5. Summary of the electronic properties of compounds A, B, and C. 84

Table 4.1. Onset of decomposition (T_{onset}) and percentage photobleaching in DCM for [P][I] and PGUMBOS. 100

Table 4.2. Absorption maxima (A_{max}), FWHM, molar extinction coefficients (ε) in methanol for [P][I] and PGUMBOS. 102

Table 4.3. Emission maxima and full widths at half -maxima (FWHM) for [P][I] and PGUMBOS in methanol. 103

Table 4.4. Fluorescence lifetime and PLQY data for [P][I] and PGUMBOS in different solvents 107

Table 4.5. Experimental HOHO-LUMO energies and energy gaps of [P][I] and PGUMBOS. 108

LIST OF FIGURES

Figure 1.1. Global share of OLED market forecast by region (A), by display application type (B), and by lighting application type (C). 2

Figure 1.2. Consumer electronics and lighting applications based on OLED technology. 3

Figure 1.3. Schematic representation of a state-of-the-art multi-layered OLED design indicating the flow of charges under an applied electric field. 5

Figure 1.4. Bottom emitting (A), inverted top emitting (B), and transparent (C) OLED architectures. 6

Figure 1.5. Exciton harvesting mechanisms, molecular designs, and emissive layer designs employed to optimize the longevity, efficiency, and spectral purity of blue OLED emitters in electronic displays. 7

Figure 1.6. Modified Jablonski diagrams displaying exciton harvesting mechanisms, conventional fluorescence and phosphorescence (A), thermally activated delayed fluorescence (TADF, B), and triplet-triplet annihilation (TTA, C). 9

Figure 1.7. Examples of common luminophores used for syntheses of blue emitters..... 12

Figure 1.8. Schematic representation of an amorphous GUMBOS derived from a crystalline salt by counterion variation. 15

Figure 1.9. Energy transfer mechanisms between a donor molecule (M_D) and an acceptor molecule (M_A). 16

Figure 1.10. A simplified schematic diagram of a typical VTE system. 18

Figure 1.11. Schematic diagram of a double beam UV-vis spectrophotometer 20

Figure 1.12. A simplified schematic diagram of a spectrofluorometer with sample holder options. Sample holder set-up for fluorescence (A), absolute quantum yield (B), and OLED prototype performance testing (C). 22

Figure 1.13. Schematic diagram of CV instrumentation (A) and a typical voltammogram for a single electron redox process (B). 24

Figure 1.14. Schematic diagram of an X-ray diffractometer. 25

Figure 1.15. The RGB primary color stimuli response (tristimulus values) curves (A) and the 1931 CIE chromaticity coordinates diagram (B). 26

Figure 1.16. Sub-pixel designs of electronic screens, conventional RGB (A) and novel RGB_1B_2 (B) designs. 27

Figure 1.17. Photopic response curve for the human eye. 28

Figure 2.1. Chemical structures of pyrenylpyridines evaluated in this study. 45

Figure 2.2. Two-dimensional GIWAXS image of a 2,4,6-TPP thin film on a quartz substrate (top) and vertical linecut of the GIWAXS data of the film (bottom). 48

Figure 2.3. HOMO (A) and LUMO (B) of 2,4,6-TPP. 49

Figure 2.4. Normalized absorption spectra of pyrenylpyridines in chloroform solution and as thin films on quartz. 52

Figure 2.5. Normalized emission spectra of pyrenylpyridines in chloroform solution and as thin films on quartz. 54

Figure 2.6. Normalized absorbance, excitation, and emission spectra of 2,4,6-TPP in chloroform solution. 55

Figure 2.7. A simplified schematic of the device architecture (A) and OLED performance plots (B) for the OLED prototype with 2,4,6-TPP as the emissive layer. 59

Figure 2.8. A photograph showing electroluminescence of the OLED prototype with 2,4,6-DPP as the emissive layer. 60

Figure 3.1. Synthesis schemes of pyrene-benzimidazole derivatives 73

Figure 3.2. Time-dependent relative photoluminescence intensity fluctuation curves of compounds A, B, and C thin films over a time period of 100 min. 76

Figure 3.3. Normalized UV-vis absorption (Abs.) and photoluminescence (PL) spectra of compound B and its parent compounds: pyrene derivative (P_1) and benzimidazole derivative (P_2) in DCM. 78

Figure 3.4. Normalized UV-vis absorption and fluorescence spectra of compound A, B, and C in DCM (1 μM, solid lines) and neat films (dashed lines). 80

Figure 3.5. A simple schematic diagram of the OLED prototype (A) and a photograph of actual OLED showing blue emission at 3 V (B). 85

Figure 3.6. Normalized photoluminescence (PL) from solution and solid states, and electroluminescence from the OLED prototype recorded for compound B. 86

Figure 4.1. Synthesis scheme of PGUMBOS. 97

Figure 4.2. TGA profiles of [P][I] and PGUMBOS..... 99

Figure 4.3. Time-dependent relative photoluminescence intensity of [P][I] and PGUMBOS in solution over a time period of 3000 s. 102

Figure 4.4. Normalized absorbance of [P][I] and PGUMBOS in methanol solution. 103

Figure 4.5. Normalized photoluminescence spectra of [P][I] and PGUMBOS in solution when excited at A_{max1} (A) and A_{max2} (B) wavelengths..... 104

Figure 4.6. Normalized absorption and photoluminescence spectra of [P][BETI] solid film. ... 105

Figure 4.7. Calculated distributions of molecular orbitals near the energy gap for the propidium luminophore. 109

LIST OF SYMBOLS AND ABBREVIATIONS

λ	Wavelength
λ_{abs}	Absorption maximum
λ_{edge}	Absorption onset at higher wavelength
λ_{max}	Emission maximum
A	Absorbance
ACN	Acetonitrile
AIE	Aggregation induced emission
Alq_3	Tris(8-hydroxyquinolinato)aluminium
AMOLED	Active-matrix organic light emitting diode
BCP	Bathocuproine (2,9-dimethyl-4,7-diphenyl-1,10-phenanthroline
CBP	4,4'-Bis(N-carbazolyl)-1,1'-biphenyl
CE	Current efficiency
CFL	Compact fluorescent light
CIE	Commission Internationale de L'Eclairage
CIF	Crystallographic information file
CV	Cyclic voltammetry
DCM	Dichloromethane
DMF	Dimethylformamide
DMPPP	1,1'-(2,5-Dimethyl-1,4-phenylene)dipyrene
DMSO	Dimethyl sulfoxide
DPPs	Dipyrenylpyridines

EA	Ethyl acetate
EBL	Electron blocking layer
EBPVD	Electron-beam physical vapor deposition
E_g	HOMO-LUMO energy gap
EIL	Electron injection layer
EML	Emissive layer
EMS	Electromagnetic spectrum
ESI-MS	Electrospray ionization-mass spectrometry
ETL	Electron transport layer
EQE	External quantum efficiency
eV	Electronvolt
Fc/Fc^+	Ferrocene/ferricenium redox couple
FRET	Förster resonance energy transfer
FWHM	Full width at half maximum
GIWAXS	Grazing-incidence wide-angle X-ray scattering
GUMBOS	Group of uniform materials based on organic salts
ISC	Inter system crossing
ITO	Indium tin oxide
IQE	Internal quantum efficiency
HBL	Hole blocking layer
HIL	Hole injection layer
HOMO	Highest occupied molecular orbitals
HTL	Hole transport layer

LCD	Liquid crystal display
LUMO	Lowest unoccupied molecular orbitals
MALDI-MS	Matrix-assisted laser desorption ionization-mass spectrometry
MeOH	Methanol
NMR	Nuclear magnetic resonance
NPB	N,N′-di(1-naphthyl)-N,N′-diphenyl-(1,1′-biphenyl)-4,4′-diamine
OLED	Organic light emitting diode
PAH	Polycyclic aromatic hydrocarbons
PLQY	Photoluminescence quantum yield
PMOLED	Passive-matrix organic light emitting diode
PVD	Physical vapor deposition
PXRD	Powder X-ray diffraction
RGB	Red, green, blue
RISC	Reverse inter system crossing
TADF	Thermally activated delayed fluorescence
TCSPC	Time correlated single photon counting
TGA	Thermogravimetric analysis
THF	Tetrahydrofuran
T_{onset}	Decomposition onset temperature
TPBI	1,3,5-Tris(1-phenyl-1H-benzimidazole-2-yl)benzene
TTA	Triplet-triplet annihilation
TTET	Triplet-triplet energy transfer

VTE	Vacuum thermal evaporation
XRD	X-ray diffraction

ABSTRACT

Organic Light Emitting Diodes (OLEDs) are predicted to revolutionize next generation consumer electronics by offering many advantageous device characteristics, including low power consumption, low heat dissipation, a tunable and wider color gamut, high resolution and contrast, light weight, flexibility, and semi-transparency. However, a major limiting factor for OLEDs to reach their full potential is that only a few known blue OLED emitters with substantial spectral purity and longevity are available to date. Therefore, focus of this research is on understanding and addressing limitations of OLED emitters, with an emphasis on improving the characteristics of blue emitters.

The work presented in this dissertation includes understanding structure-property relationships of OLED blue emitters using four structurally related pyrenylpyridines as model compounds (chapter 2), applying these structure-property relationship concepts to synthesize three novel blue emitters derived from pyrene-benzimidazole conjugates with substantially improved spectral properties (chapter 3), as well as synthesizing and characterizing propidium luminophore (3,8-diamino-5-[3-(diethylmethylammonio)propyl]-6-phenylphenanthridinium dication) based GUMBOS (**g**roup of **u**niform **m**aterials **b**ased on **o**rganic **s**alts) to evaluate how these GUMBOS materials can be applied to address the aforementioned limitations of OLED emitters. A number of analytical tools were applied to study the characteristics of these compounds, including morphology, spectroscopy, photothermal stability, and electrochemistry. Also, OLED prototypes were fabricated and characterized with selected compounds to understand the luminance, current, and power relationships of these materials.

CHAPTER I. INTRODUCTION

1.1. Organic Light Emitting Diodes (OLEDs) - A Brief Overview

Organic semiconductors are widely used in optoelectronic applications such as photovoltaics,[1] photodetectors,[2] phototransistors,[3] and light emitting diodes.[3,4] Among these, OLED technology represents one of the most promising means of next generation energy-saving, full-color, flat-panel electronic displays and lighting.[5] Since electronic display and lighting applications are integral to modern life, an estimated global market share of $9.6 billion is expected by the year 2020 for OLEDs, with the highest contribution from the Asia-Pacific region, as depicted in Figure 1.1 (A).[5] Also, the global OLED market share statistics indicate that the largest market segments for OLED displays are held by televisions and laptops/tablets/personal computers (PCs), whereas the largest market segments for OLED lighting are held by residential, commercial, outdoor, and automotive lighting applications, as shown in Figure 1.1 (B and C).[5]

The concept of OLEDs was initiated by observation of electroluminescence from small organic molecules, such as acridine derivatives, by French scientists at the University of Nancy, France, in 1950s.[6] In 1987, Ching W. Tang and Steven A. Van Slyke (Eastman Kodak, USA) reported the first commercially useful OLED prototype, which showed a substantial light emission efficiency at a relatively low voltage (10 V).[7] This breakthrough helped OLEDs to rapidly evolve from a preliminary laboratory concept to a commercially sustainable leading technology. Sony launched the first OLED display, XEL-1 television, in 2007 whereas OSRAM commercialized the first OLED lamp in 2008.[5] Today, companies such as Samsung, Sony, LG, Panasonic, Apple, Dell, and Asus lead the OLED display market. Companies that lead the lighting market include Philips, OSRAM, LG Chem, Konica Minolta Pioneer OLED (KMPO), Seimens, Selux, and Acuity

Brands. Figure 1.2 displays some consumer electronic products and lighting applications based on OLEDs that are available in the current market.[8,9]

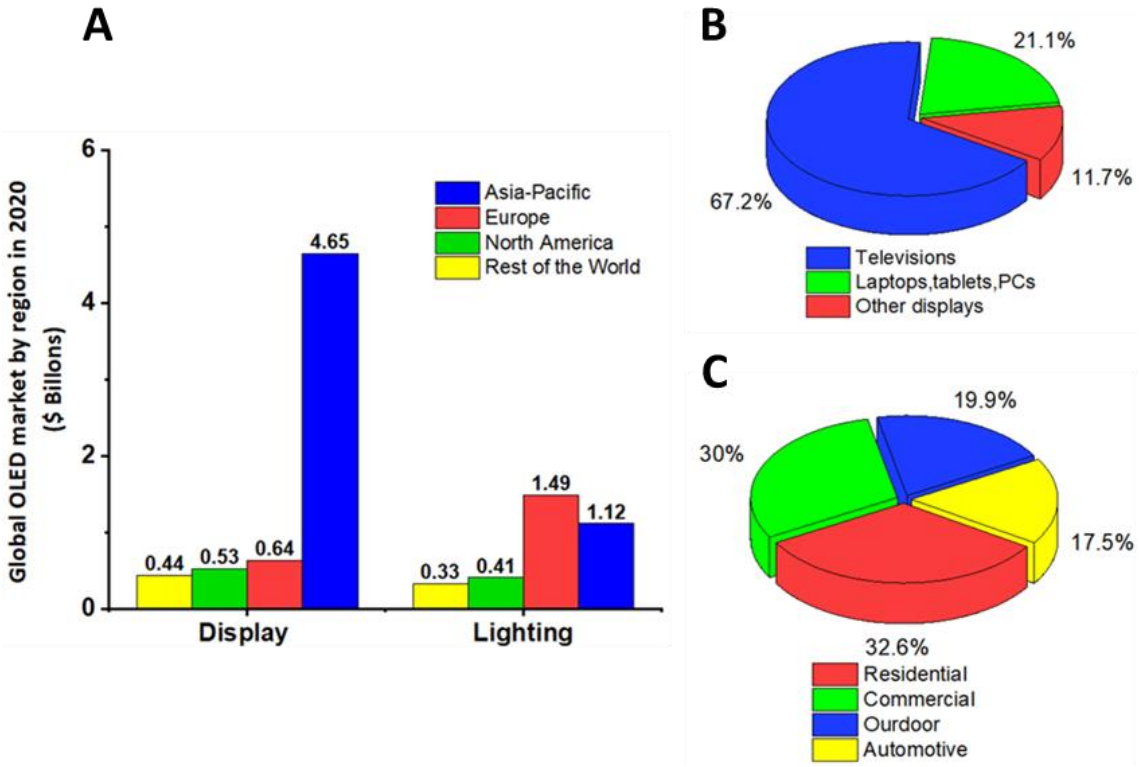

Figure 1.1. Global share of OLED market forecast by region (A), by display application type (B), and by lighting application type (C).

The cutting-edge advantages of OLED display with respect to the competing display technology, liquid crystal display (LCD), are low power consumption, semi-transparency, low weight, flexibility, faster response time, wider viewing angles, wider color range, high resolution, and high contrast.[10,11] Additionally, OLED based lighting panels offer unique advantages. These advantages include the absence of hazardous heavy metals like mercury, which is found in compact fluorescent light (CFL) bulbs, significantly lower heat generation compared to incandescent bulbs, and 'paper-like' thin, light weight, and remarkably malleable structures that provide great design flexibility.[8,9] Also, OLED white light panels emit soft diffused light that resemble natural sun light with insignificant emission of near UV radiation.[12] This is in contrast

to most LED bulbs, which often emit near UV radiation, thus OLED based lighting applications provide more safety and comfort to the eyes.[12]

Panasonic TX-65CZ950 65” curved TV

Asus ProArt PQ22UC 21.6" monitor

Samsung Galaxy A8/A8+ smart phones

Acer Liquid Leap+ smart fitness tracker

Apple smart watches

HTC Vive Pro VR headset

Acuity Brands OLED lighting panels for offices

Audi TT RS OLED tail lights

OSRAM OLED lighting panels for homes

Figure 1.2. Consumer electronics and lighting applications based on OLED technology.

Beyond this point, the main focus of this chapter is to provide an overview of the principles and components of OLED display, since this focus is in line with the broader objective of this research, which is, to improve the characteristics of OLED emitters used in electronic displays.

1.2. Working Principle of OLEDs

OLEDs are solid-state electroluminescent devices consisting of multiple organic semiconducting layers sandwiched between two electrodes (usually an anode and a cathode).[10,11] Therefore, the working principle of OLEDs largely relies on exciton formation and decay.[10] Excitons are mobile quasi-particles, in which an electron and a hole are paired by Coulombic interactions.[10,13] Decaying of excitons formed in the emissive layer (EML) of OLEDs under the influence of an applied electric field generates electroluminescence.[14,15]

As schematically illustrated in Figure 1.3, a simple state-of-the-art OLED design for electronic displays often contains multiple thin layers of task-specific organic materials to optimize the device's performance.[11,16] Under the influence of an applied electric field, holes and electrons are injected from the anode and the cathode into the device. These holes and electrons occupy frontier orbitals of organic semiconducting molecules and move toward oppositely charged electrodes through the organic layer(s) due to Coulombic interactions. Holes hop through the highest occupied molecular orbitals (HOMO, analogues to the valence band of inorganic semiconductors), whereas electrons hop through the lowest unoccupied molecular orbitals (LUMO, analogues to the conduction band of inorganic semiconductors).[10] A fraction of these holes and electrons combine to form excitons in the EML, in which both electrons and holes are found in abundance. Subsequent radiative decay of excitons yield photons. The color of the emitted photons is determined by the HOMO-LUMO energy gap (E_g) of the EML.[10,16] Since red, green, and blue (RGB) colors are indispensable to realizing full-color electronic displays, OLEDs are often designed to emit RGB colors by appropriately tuning the E_g of EML materials.[17] Supporting organic layers (i.e., charge injection layers, charge transport layers, and charge blocking layers) are energetically matched with HOMO and/or LUMO levels of EML to optimize the flux of

charges from electrodes to the EML and maintain the maximum charge concentration within the EML.

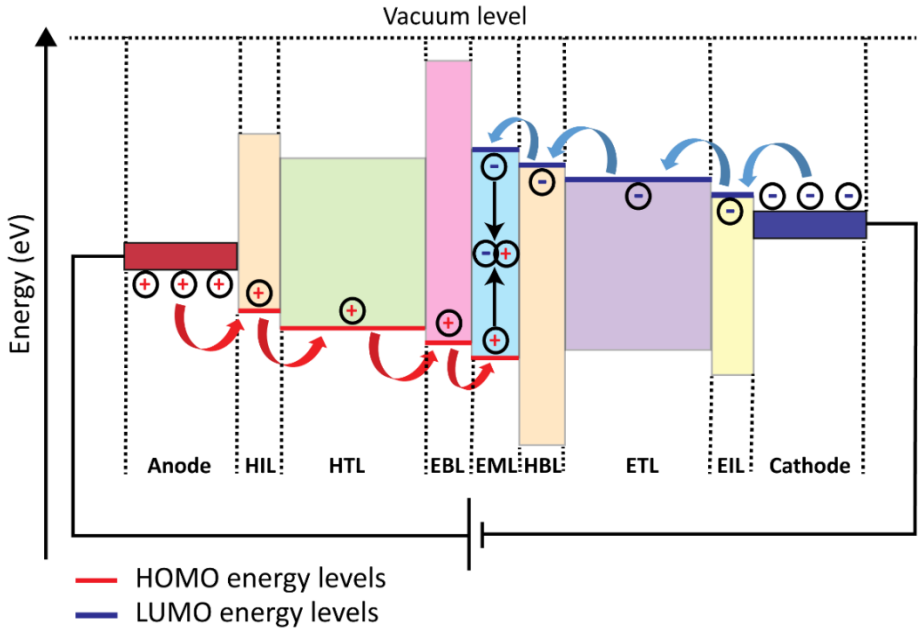

Figure 1.3. Schematic representation of a state-of-the-art multi-layered OLED design indicating the flow of charges under an applied electric field. (*HIL: hole injection layer, HTL: hole transport layer, EBL: electron blocking layer, EML: emissive layer, HBL: hole blocking layer, ETL: electron transport layer, EIL: electron injection layer*).

1.3. OLED Classification

OLEDs are classified as bottom-emitting (conventional), top-emitting (inverted), and transparent, according to the device architectures, as shown in Figure 1.4.[16,18] Bottom-emitting OLEDs transfer light through bottom semi-transparent electrode(s), whereas top-emitting OLEDs transfer light through top semi-transparent electrode(s). In transparent OLEDs, light travels through both top and bottom semi-transparent electrodes.

Indium tin oxide (ITO) is the most widely used semi-transparent electrode material to date, whereas ultrathin films, grids, nanotubes, and nanowires made from materials including metals, graphene, and polymers are also employed as electrode materials.[18] Inverted and transparent OLEDs have advantages such as the ability to use a wide variety of substrates, including flexible

and wearable materials, are easy to integrate with OLED circuitry, and have significantly low wave-guiding losses of light through the substrate.[19,20]

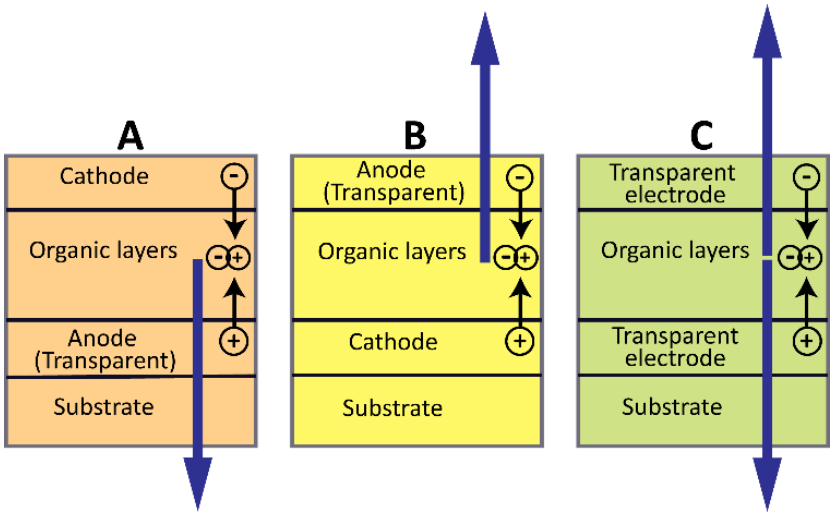

Figure 1.4. Bottom emitting (A), inverted top emitting (B), and transparent (C) OLED architectures.

In electronic screens, OLEDs are often applied as either passive-matrix OLEDs (PMOLEDs) or active-matrix OLEDs (AMOLEDs).[16] PMOLEDs have anode stripes perpendicular to cathode stripes, in contrast to AMOLEDs, in which electrodes are found as complete layers. Also, AMOLEDs contain a thin film transistor plane parallel to the anode.[16,21] Production of PMOLED screens is relatively economical and less complex compared to AMOLED screens. However, PMOLED screens have limitations, such as high power consumption, low resolution, and a low operational lifetime compared to AMOLEDs. Also, PMOLEDs are typically applied to small screens (> 3") that limited to display a few characters or a few small icons.[8] In contrast, AMOLED design is more complex and applicable to large and complex screens, with advantages including low power consumption, a high battery life, and high resolution.[8] Accordingly, PMOLEDs are limited to wearable and/or small devices, while AMOLEDs are used in a wide variety of larger and more complex electronic devices, such as monitors, large-screen televisions, smart phones, electronic signs, and billboards.

1.4. Blue Emitters in OLED Displays

The research work presented in this dissertation focuses mainly on blue OLED emitters. The first blue emitting multi-layer OLED was fabricated by Japanese scientists in 1990.[22] Blue is a primary color that is essential to realizing full-color displays along with red and green emitters. These RGB emitters should ideally yield equivalent color purity, operational lifetime, and efficiency. However, the intrinsically wide HOMO-LUMO energy gap of blue emitters affects efficient charge injection and causes rapid deterioration of EML, particularly upon excitation.[23,24] As a result, blue emitters typically have lower operational lifetimes, lower efficiencies, and lower spectral purities compared to red and green emitters, thus causing a key obstacle for the long-term commercial viability of OLED technology.[23] Accordingly, several strategies were introduced to address the inadequacies that are inherent to blue emitters including optimization of molecular design, optimization of EML design, and improving exciton harvesting mechanism(s).[23-25] Figure 1.5 provides a brief summary of these approaches towards improvement of aforementioned limitations of blue emitters. Also, sections 1.5-1.7 of this chapter further discuss these approaches in detail.

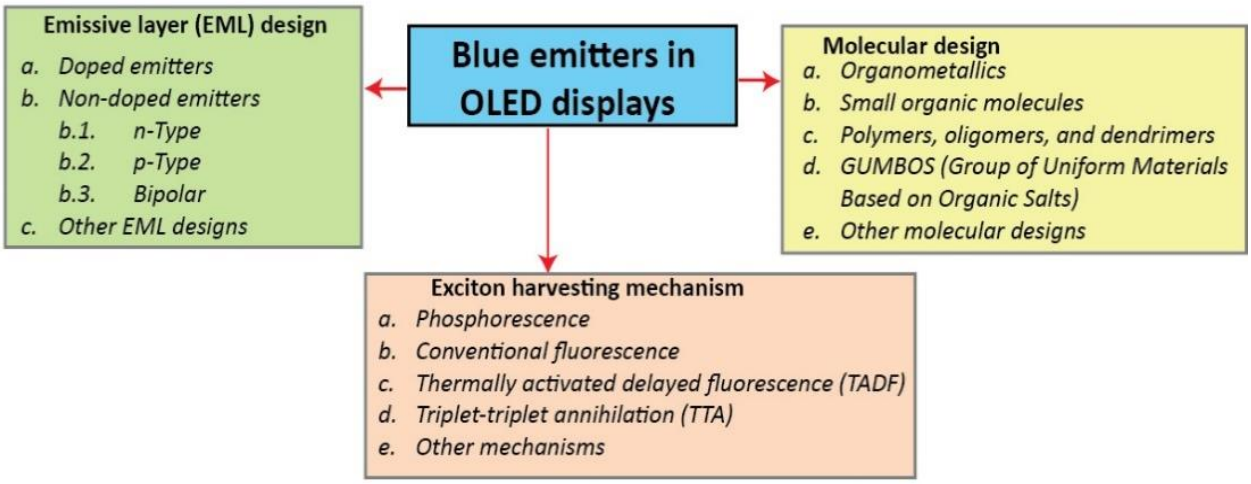

Figure 1.5. Exciton harvesting mechanisms, molecular designs, and emissive layer designs employed to optimize the longevity, efficiency, and spectral purity of blue OLED emitters in electronic displays.

1.5. Exciton Harvesting Mechanisms

The ability to extract photons from OLEDs by the exciton decay process occurs in the EML is known as exciton harvesting.[25,26] The exciton harvesting efficiency of a particular emitter can be quantified using electroluminescence quantum efficiency, which is the ratio of emitted photons to injected charges.[11] Internal quantum efficiency (IQE) is the ratio of the emitted photons generated within the OLED to the number of injected charges, whereas external quantum efficiency (EQE) is the ratio of emitted photons into the viewing direction to injected charges.[11,26] Electroluminescence quantum efficiency of OLEDs is further discussed in section 1.9.5.4 of this chapter. To date, well established mechanisms for harvesting excitons in OLEDs are conventional fluorescence/fluorescence, phosphorescence, thermally activated delayed fluorescence (TADF), and triplet-triplet annihilation (TTA)/triplet fusion.[15,23-28] These exciton harvesting processes are schematically illustrated in Figure 1.6 using modified Jablonski diagrams.

1.5.1. Fluorescence and Phosphorescence

Fluorescence is the radiative transition between electronic states with the same spin multiplicity.[29] Therefore, conventional fluorescence is 'an allowed' transition, which refers to the selection rules stating that the electronic transitions between two electronic states with the same spin multiplicity are allowed.[29] Consequently, conventional fluorescence is a fast process that occurs within nanoseconds.[29] However, only 25% of excitons that are in the singlet state can undergo conventional fluorescence.[15,25] Furthermore, the internal reflection of photons restricts light extraction from OLEDs due to the presence of organic layers, electrodes, and glass substrates.[25,30] Therefore, the EQE of a typical bottom emitting OLED is estimated as 20% of its IQE value.[24,30] As a result, the theoretical upper limit of EQE for a bottom emitting OLED with conventional fluorescence is approximately 5%.[24] Common fluorophores widely used in blue

emitters include anthracene, phenanthrene, fluorene, pyrene, carbazole, triphenylamine, indenopyrazine, benzimidazole, and imidazole.[23-25]

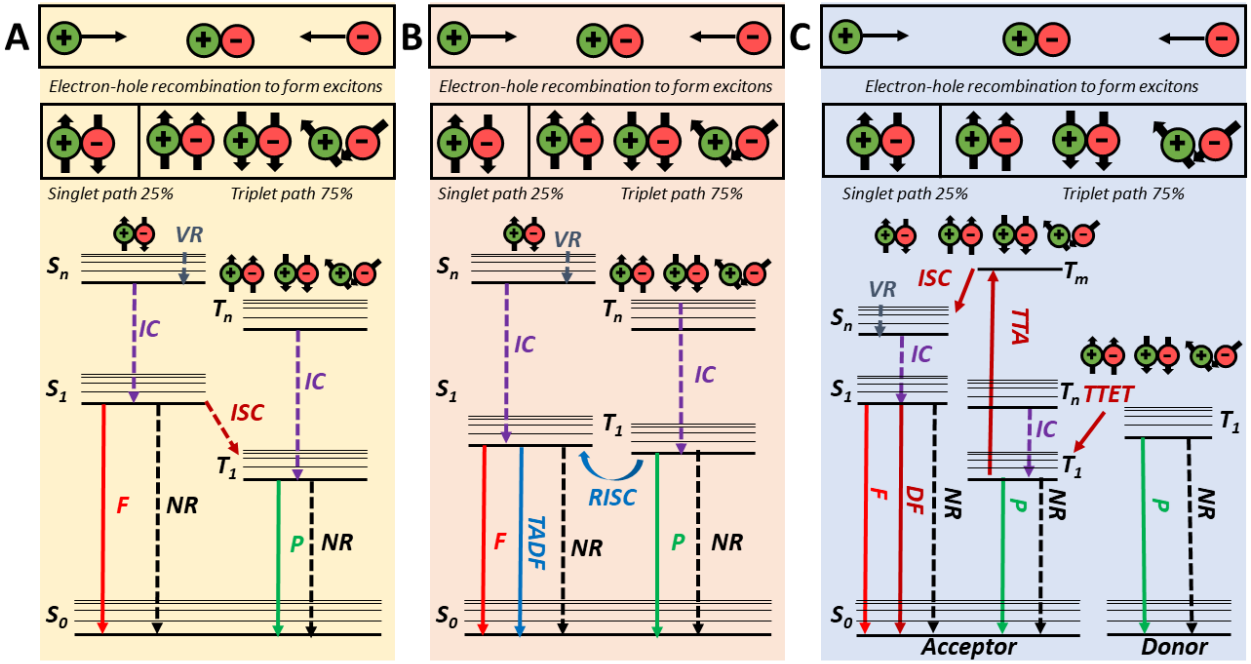

Figure 1.6. Modified Jablonski diagrams displaying exciton harvesting mechanisms, conventional fluorescence and phosphorescence (A), thermally activated delayed fluorescence (TADF, B), and triplet-triplet annihilation (TTA, C). (*F: conventional fluorescence P: phosphorescence, S: singlet state, T: triplet state, NR: non-radiative decay, VR: vibrational relaxation, IC: internal conversion, ISC: inter-system crossing, RISC: reverse inter-system crossing, TTET: triplet-triplet energy transfer*).

Phosphorescence is a radiative transition between states of different multiplicities.[29] Phosphorescence is 'forbidden' in accordance with the selection rule of quantum mechanics.[29] Accordingly, phosphorescence takes a much longer time (microseconds to milliseconds) than fluorescence and is often sensitive to environmental conditions.[29] Phosphorescence can theoretically harvest up to 75% of excitons in the triplet state and is very common in organometallic emitters.[24] Interestingly, some phosphorescent transition metal complexes possess strong spin-orbit coupling with the lowest excited state, causing an accelerated relaxation of excitons from S_1 state to T_1 state via fast inter system crossing (ISC) that occurs within femtoseconds. Simultaneously, these complexes significantly relax the selection rules, and thus

enhance T_1 to S_0 transition of excitons. As a result, phosphorescence in some transition metal complexes can theoretically harvest 100% of excitons generated under electrical excitation regardless of the spin state, yielding nearly 100% IQE.[31-33]

1.5.2. Thermally Activated Delayed Fluorescence (TADF)

TADF based OLED emitters were first reported by Japanese scientists in 2009.[34] TADF upconverts triplet excitons to singlet excitons by thermal activation followed by subsequent harvest of singlet excitons via conventional and delayed fluorescence.[34-37] Delayed fluorescence observed in TADF is caused by reverse inter system crossing (RISC).[35,36] Since S_1 state has a slightly higher energy compared to T_1 state in TADF emitters, the exciton upconversion process is essentially endothermic and the resultant fluorescence intensity is temperature dependent.[35,36] However, some TADF compounds are designed to undergo substantial RISC even at room temperature without providing external heating, thus making TADF emitters easily integrated to OLEDs.[36,37] Since TADF emitters harvest both singlet and triplet excitons, 100% IQE can be theoretically achieved with these emitters.[35] The two most important characteristics of compounds that show TADF are, 1) a small energy gap between S_1 and T_1 states and 2) having a high photoluminescence quantum yield (PLQY), according to the equation 1.1.[36]

$$IQE = N_S.PLQY + \mathrm{N}_S.\mathrm{QY}_{DF} + \mathrm{E}_T.\left(\frac{\mathrm{QY}_{DF}}{\mathrm{QY}_{ISC}}\right) \quad (1.1),$$

where N_S is the efficiency of singlet exciton generation (≤ 0.25), E_T is the efficiency of triplet exciton generation (≤ 0.75). PLQY, QY_{DF}, and QY_{ISC} are quantum yields of photoluminescence, delayed fluorescence, and inter-system crossing, respectively.[36] Companies such as Kyulux (Japan) and Cynora (Germany) are forerunners in the development of TADF based OLEDs.

1.5.3. Triplet-Triplet Annihilation (TTA)

TTA is another method of harvesting triplet excitons that was first reported in the 1960s by British scientists.[38] TTA is also an upconversion process of excited triplet excitons to excited singlet excitons, as in TADF.[38-40] However, unlike TADF, TTA utilizes a bimolecular process, in which, the fusion of two T_1 excitons generates two singlet excitons in S_0 and S_1 states (also see section 1.7 in this chapter for further details). Accordingly, an IQE of 62.5% can be achieved in theory for TTA based emitters.[39] The crucial step in TTA is the radiationless triplet-triplet energy transfer (TTET) occurring between the donor and the acceptor in close proximity (< 10 Å), which is usually a bimolecular Dexter energy transfer process.[39] Other requirements to obtain efficient TTA upconversion include lower triplet energy of the acceptor than the donor (to facilitate an efficient energy transfer), high PLQY for the acceptor, and an efficient ISC of the donor (to adequately populate the donor triplet state).[40,41]

1.6. Molecular Design

The first OLED design reported by Ching W. Tang and Steven A. Van Slyke contained an organometallic compound, tris(8-hydroxyquinolinato)aluminium (Alq_3), as the electron transport and emissive material.[7] Since then, different types of molecules were designed as OLED emitters. According to the chemical structures, these OLED emitters can be classified as organometallics, small organic molecules, oligomers, dendrimers, polymers, and solid-state organic salts known as GUMBOS.

1.6.1. Organometallics as Blue Emitters

Organometallic compounds are widely used as blue emitters in OLEDs from the initial stages of OLED technology.[7,15,31-34] Novel organometallics are mostly phosphorescent emitters with the capability of harvesting both singlet and triplet excitons via effective intersystem crossing induced by strong spin-orbit coupling.[31-34] Accordingly, theoretical IQE of 100% can be achieved by these

organometallic emitters. Noticeably, coordination complexes with iridium (Ir) and platinum (Pt) as central metal ions are well-known organometallic blue emitters for OLEDs.[42-47] Organometallic complexes based on Pt are widely used in OLEDs, although Pt based blue emitters with high efficiency and spectral purity are not as common as in Ir complexes.[24] The main disadvantages of organometallic emitters are the instability of some coordination bonds formed between organic ligands and the central metal ion, which in turn affects the long-term stability of OLED devices, and the high cost of rare metals that are incorporated in these complexes.[36,48]

1.6.2. Small Organic Molecules as Blue Emitters

The research presented in this dissertation is based on OLEDs derived from small molecular organic emitters. To date, numerous small organic molecules with molecular weight less than 1000 Dalton (Da) were reported as blue emitters for OLEDs.[49-53] Electroluminescence of small organic molecules often derive from fluorescence, phosphorescence, TADF, TTA, and/or other mechanisms.[24,49-53] These small organic blue emitters usually contain luminophores such as pyrene, anthracene, fluorene, carbazole, phenanthrene, triphenylamine, and benzimidazole.[23,24,49-53] The basic chemical structures of these luminophores are presented in Figure 1.7.

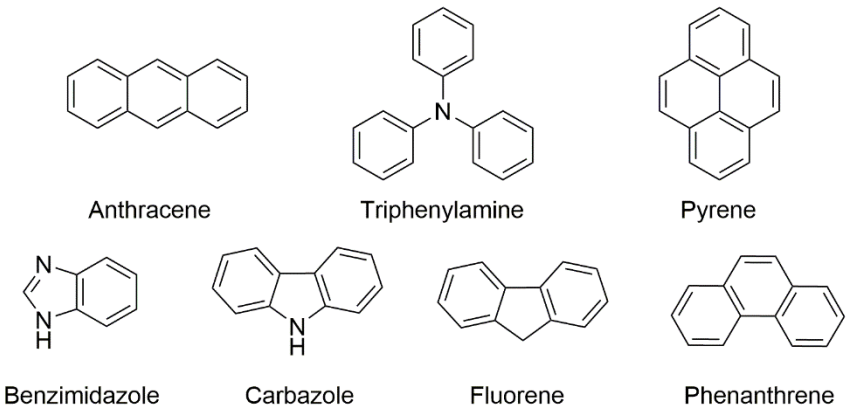

Figure 1.7. Examples of common luminophores used for syntheses of blue emitters.

Some of the unique advantages of small organic molecules that have made them popular are, well-defined chemical structures, modest synthesis, facile purification and modification, high

thermal stability, high spectral purity, substantial quantum yields, and low cost.[23,24] However, many small organic molecules have a great tendency to extensively aggregate (i.e., undergo π-π stacking) in the condensed state and form excimers/exciplexes that often induce undesirable emission band broadening, band-shifting, and aggregation-induced quenching.[23,24,49] The attachment of rigid and bulky moieties to adequately twist intramolecular ring systems as well as the practice of applying host matrices to dilute emitter concentration in the solid-state are two of the most common strategies used to control dye aggregation.[23-25] Additionally, designing emitters that undergo aggregation induced emission (AIE) by restricting intramolecular rotation in the solid-state is applicable for small molecular organic emitters.[54,55] Consequently, AIE based emitters often show an enhanced emission in solid-state than solution state. However, chemical stability of aliphatic double bonds and/or heteroatomic functional groups that are often found in AIE based emitters is typically inferior to that of polycyclic aromatic hydrocarbon (PAH) based conventional small organic molecular emitters.

1.6.3. Polymers, Oligomers, and Dendrimers as Blue Emitters

Polymers with π conjugated backbones have been extensively investigated for their suitability as emissive materials, beginning with the first polymer based OLED fabricated in 1990s by British scientists.[56] Polymers can readily be solution-processed, hence providing an inexpensive and simple means of device fabrication.[23,24] Fluorene derivatives are widely used as the repeating units of polymers owing to high quantum yield, film forming ability, high photothermal stability, and the ease of functionalization.[57,58] However, difficulties associated with polymer reproducibility, purification, and the low preciseness of the chemical structures are some of the restrictions for the application of polymers in OLEDs.[24] A typical polymer backbone is extensively twisted in solid-state due to a random orientation upon film forming, thus limiting the intramolecular interactions

to several repeating units, resembling a series of oligomers. Therefore, researchers focused on blue emitters derived from oligomers and dendrimers, which have precise chemical structures that can be synthesized with high reproducibility and purity, while preserving most of the advantages offered by polymers.[49,59-61] These blue luminescent polymers, oligomers, and dendrimers typically contain same luminophores that are used in small molecules, as showed in Figure 1.7, in their core/backbone.[24,49,59-61]

1.6.4. GUMBOS as Blue Emitters

Solid-state organic salts with melting points in the range of 25-250 ºC are referred to as GUMBOS to distinguish them from liquid state organic salts, i.e., ionic liquids.[62] The key advantage to GUMBOS is their capability for tuning some of the physical, chemical, and spectral properties by incorporating task-specific counterions, thus providing an economical and simple means to improve the characteristics of resultant ionic organic compounds.[62] Such physical and chemical modifications induced by counterion variations include tuning the hydrophobicity/solubility,[63,64] selective chemical sensitivity,[65] tuning spectral characteristics,[66,67] improving photothermal stability,[67] tuning molecular motion,[68] and tuning magnetic behavior.[69] For example, figure 1.8 schematically shows the solid-state morphology of an ionic luminophore changed from crystalline to amorphous by simple counter ion variation process. Noticeably, Warner group has introduced a number of task-specific GUMBOS for a range of applications.[62-67] Among these, the first GUMBOS compounds reported for OLED applications contained a carbazole-imidazole conjugated small organic compound as the cation and three organic counteranions derived from fluoroalkylsulfonates.[67] These imidazoliumcarbazole based GUMBOS are deep blue emitters with improved photothermal stability and significantly high

PLQY than their non-GUMBOS analogues.[67] Furthermore, imidazoliumcarbazole GUMBOS were found predominantly amorphous with improved film forming ability.[67]

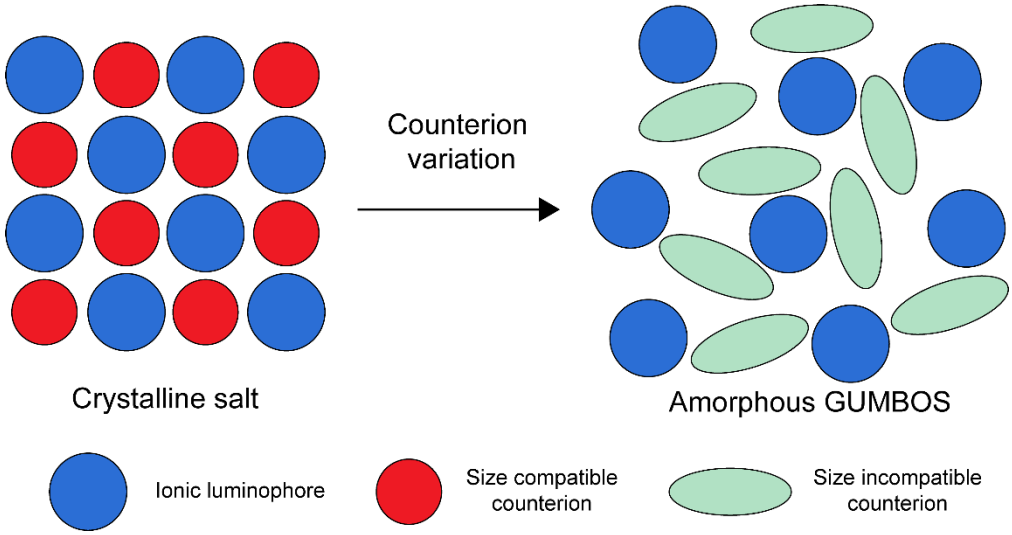

Figure 1.8. Schematic representation of an amorphous GUMBOS derived from a crystalline salt by counterion variation. Note the less compatible stacking in the GUMBOS.

1.7. EML Design

The OLED emitter may be embedded in a host matrix (i.e., doped EML) or used as is (i.e., non-doped/self-host EML).[23] Doping process dilutes emitter concentration in the EML thus effectively reducing aggregation-induced quenching. Also, doping typically improves device performance by inducing energy transfer mechanisms that occur between the host matrix and the emitter. The most common energy transfer processes between a donor/host and an acceptor/emitter in a doped EML are Förster resonance energy transfer (FRET), Dexter energy transfer, and TTA.[29] These energy transfer mechanisms are schematically shown in Figure 1.9.

FRET involves a host molecule (donor) in the excited state that transfers energy to the emitter molecule (acceptor) in the ground state. In order to undergo FRET, the host and the donor should be in close proximity to electronically couple via Coulombic forces and show significant overlap of the host emission spectrum and the acceptor absorption spectrum.[29,70] Dexter energy transfer occurs between a donor and an acceptor, in which, an exciton diffuses from an excited host

molecule (donor) to the ground state emitter (acceptor) in very close proximity and has similar requirements as in FRET.[71] Most common Dexter energy transfers are singlet-singlet and triplet-triplet energy transfers. TTA is a special type of energy transfer mechanism in some phosphorescent emitters, where a triplet excited state donor and a triplet excited state acceptor interact to produce an excited singlet state exciton within the acceptor.

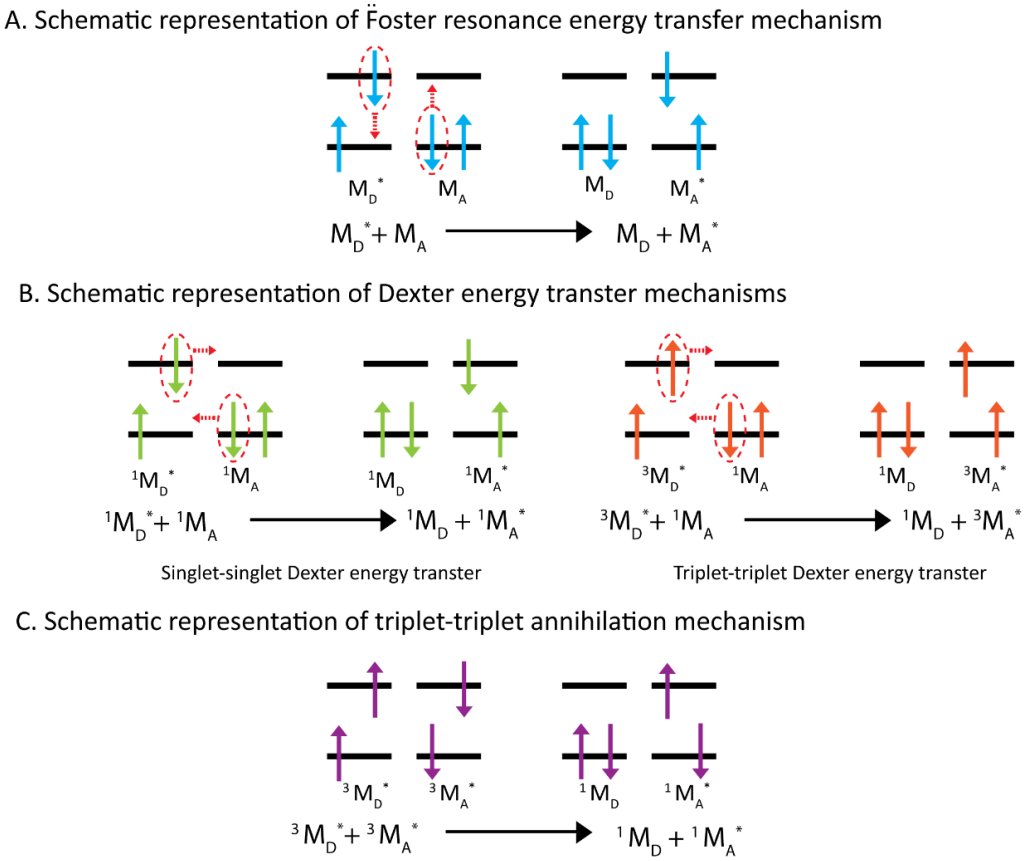

Figure 1.9. Energy transfer mechanisms between a donor molecule (M_D) and an acceptor molecule (M_A).

In the case of blue emitters, compatible hosts require wider band gaps and thus further hinder charge injection to EML.[23,24] Therefore, doped blue EMLs often require additional organic layers to support charge injection and transport. Other disadvantages associated with doping include phase separation induced degradation, limited availability of energetically matching hosts, and complexity of the device fabrication process.[23] Due to these shortcomings of doped EMLs,

numerous OLEDs are fabricated without hosts, which are known as non-doped/self-emitters. These non-doped emitters offer advantages such as relatively simple device architectures and inexpensiveness. Further, the difficulty of charge injection to the EML in blue emitters can be addressed in non-doped emitters by functionalizing the emitters with hole- and/or electron-transport units to yield multifunctional blue emitters.[23] For example, triarylmine and carbazole moieties are often use as the hole-transporting/*p*-type units, whereas indenopyrazine, quinolone, phosphine oxide, oxadiazole, and imidazole moieties are often employed as electron transporting/*n*-type units in multifunctional blue emitters.[23] Bipolar blue emitters contain both *p*- and *n*- type moieties.[23]

1.8. OLED Fabrication

OLEDs are often fabricated by depositing thin films of organic semiconducting materials and metallic electrode materials on substrates using physical vapor deposition (PVD) techniques, i.e., vacuum thermal evaporation (VTE) and electron-beam physical vapor deposition (EBPVD). [11,72,73] Solution processing such as ink-jet printing and spin casting is another OLED fabrication method for heat-sensitive, non-volatile materials and polymers.[11,72,73] This chapter only discusses VTE in detail, since OLED prototypes reported in this dissertation were fabricated exclusively using VTE technique.

VTE is a well-known organic thin film deposition technique heavily used in both academia and industry, particularly for thermally stable and substantially volatile small organic molecules. The first step of OLED fabrication using VTE is loading ultra-pure solid material(s) that needs to be deposited to the sample holder(s), and securing the clean substrate to the substrate holder(s) inside the VTE chamber. Then, the VTE chamber is sealed and an ultra-high vacuum ($< 1 \times 10^{-6}$ Torr) is applied followed by a current flow across an electrical resistive heating element attached

to the sample holder. Consequently, the sample holder is gradually heated and the material starts evaporating/subliming at a pre-determined rate. Then, this evaporated/sublimed material traverses the chamber and deposits on the substrate as a thin film. Organic materials are often deposited at a rate of 1 Å/s or below to achieve defect-free and uniform thin films. Therefore, material evaporation rate and film thickness are precisely monitored. The substrate, which is usually suspended to a substrate holder on the inner chamber roof, is covered by a shutter until the desired material deposition rate is reached, as well as often heated and/or rotated during the deposition process to facilitate the formation of a uniform and defect free thin film. Patterning of deposited organic films is achieved by the use of shadow masks, which are applied to the substrate prior to the deposition process and removed after the deposition.[74] Figure 1.10 shows the basic components of a typical VTE system with multiple sample holders and heating elements, which enables the thermal deposition of several different materials at one time (co-deposition) and/or switches between samples to deposit multiple layers in a single run to save time.

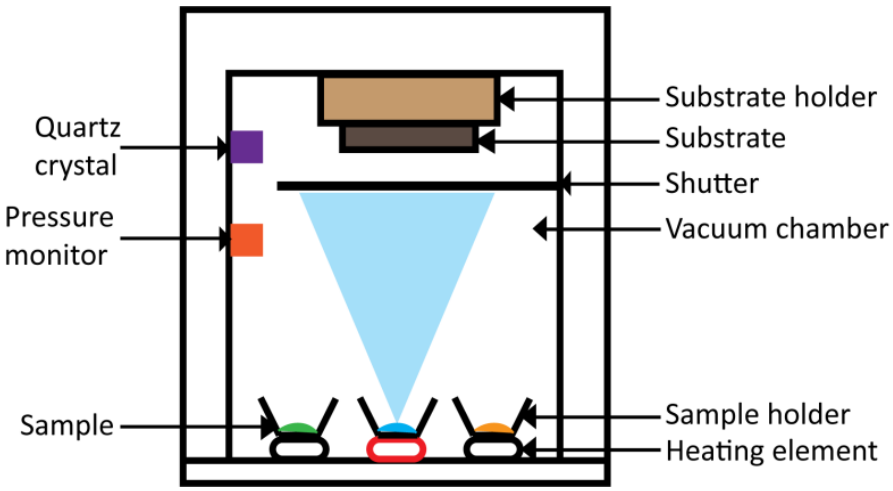

Figure 1.10. A simplified schematic diagram of a typical VTE system.

1.9. Analytical Techniques Used in This Research

1.9.1. Ultraviolet-Visible (UV-vis) Spectroscopy

An organic molecule can absorb UV-vis light of a certain wavelength that provides the energy required to promote ground state electrons to excited states. Common electronic transitions of organic compounds induced by UV-vis light are 1) π bonding (π) to π anti-bonding (π*) 2) non-bonding (n) to π* 3) n to σ anti-bonding (σ*) 4) σ to π*, and 5) σ to σ*.[75] The HOMO-LUMO energy gap of an organic semiconductor is experimentally determined using absorption spectra.[76,77] For this calculation, the onset at the higher wavelength side of the absorption peak (λ_{edge}) is assumed as the minimum energy required to promote a ground state electron to the first excited state, which also represents the HOMO-LUMO energy gap for most organic emitters. Application of λ_{edge} to Planck's equation yields the HOMO-LUMO band gap of the compound, as shown in equation 1.2.[76,77]

$$\text{Energy gap (eV)} = (HOMO - LUMO) = \frac{\text{hc}}{\lambda} = \frac{1240}{\lambda_{edge}}\ (eV) \qquad (1.2),$$

where h is the Planck's constant (6.626 x 10^{-34} Js), c is the speed of light in a vacuum (3.00 x 10^{-8} ms^{-1}), and λ_{edge} is the wavelength of the photons at absorption onset (nm). The value of (h × c) is also a constant that equals 1240 eV. nm.

A double beam UV-vis spectrophotometer, schematically presented in Figure 1.11, is often employed to record absorption spectra. This instrument contains light source(s), a monochromator, and detector(s). Samples in solution state are usually measured in quartz cuvettes, whereas solid-state samples are coated on quartz plates. A monochromator is used to select the light with the required wavelength to transmit through the sample, which is then quantified by the detector with respect to a reference. The absorbance (A) of the sample is determined using equation 1.3.[29]

$$\text{A} = \frac{\log I_0}{\log I} = \epsilon \text{bc} \qquad (1.3),$$

where I_0 is the incident light intensity and I is the transmitted light intensity. For samples in the solution state, the Beer-Lambert law is a correlation of absorption with sample concentration, where ϵ is the molar absorption coefficient ($Lmol^{-1}cm^{-1}$), b is the path length (the length light travels through the sample, cm), and c is the concentration of analyte solution ($molL^{-1}$).

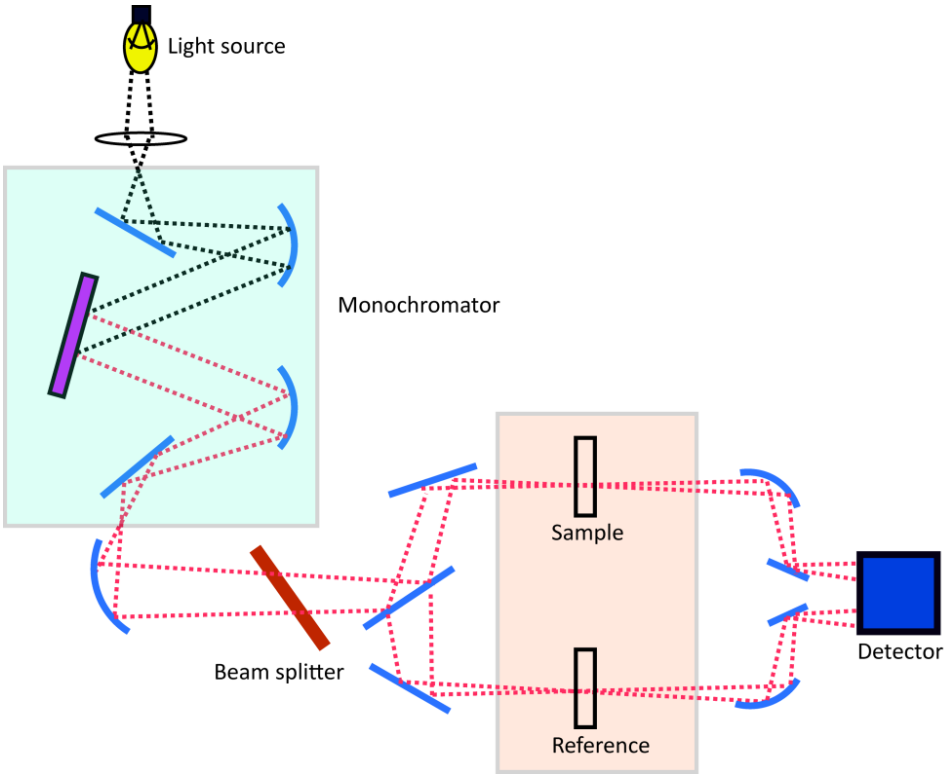

Figure 1.11. Schematic diagram of a double beam UV-vis spectrophotometer.

1.9.2. Fluorescence Spectroscopy

Radiative transitions between states of the same multiplicities is known as fluorescence.[29] Depending upon the excitation energy source, luminescence is further classified as photoluminescence, electroluminescence, chemiluminescence, radioluminescence, thermoluminescence, and etc.[29] Among these luminescence types, evaluation of photoluminescence and electroluminescence for a given emitter are crucial to determining the performance of OLED devices in terms of color purity, efficiency, and lifespan.

The photoluminescence of a compound is measured using a spectrofluorometer, which is schematically presented in Figure 1.12. A typical spectrofluorometer consists of light source(s), two monochromators for excitation and emission, and a detector. The sample in a quartz cuvette or plate is irradiated by using monochromatic light at the excitation wavelength that is specific for a given compound and the resultant photoluminescence is recorded at a right angle to the direction of the excitation light.

Another very important parameter for the evaluation of performance of fluorescence based OLED emitters is PLQY, which is defined as the ratio of emitted photons to absorbed photons.[29] PLQY is determined either relative to a standard (relative PLQY) or without such standard (absolute PLQY).[78,79] For absolute PLQY measurements, an integrating sphere is used as depicted in Figure 1.12.[78] Estimating EQE of OLED prototypes is also performed using the integration sphere.[26] Since OLEDs are self-emitters, EQE measurements are taken without using the light source of the spectrofluorometer, and therefore detecting only the amount of light emitted by the OLED.

Fluorescence lifetime is the average time a fluorophore spends in the excited state before radiatively relaxing to the ground state and can be measured using either frequency domain or time domain techniques.[29] In the time domain method, a sample is illuminated with a short pulse of light at the excitation wavelength, followed by measuring the emission intensity as a function of time, and the fluorophore lifetime is determined using the slope of the decay curve. Time correlated single photon counting (TCSPC) enables simple data analysis by counting at least one photon per excitation pulse, which is correlated to time using a time-to-amplitude converter. In the frequency domain method the sinusoidal modulation of the incident light is required.[29] Since the lifetime of

a fluorophore delays the emission in time with respect to the excitation, phase shift caused by the delay is used to calculate the decay time.

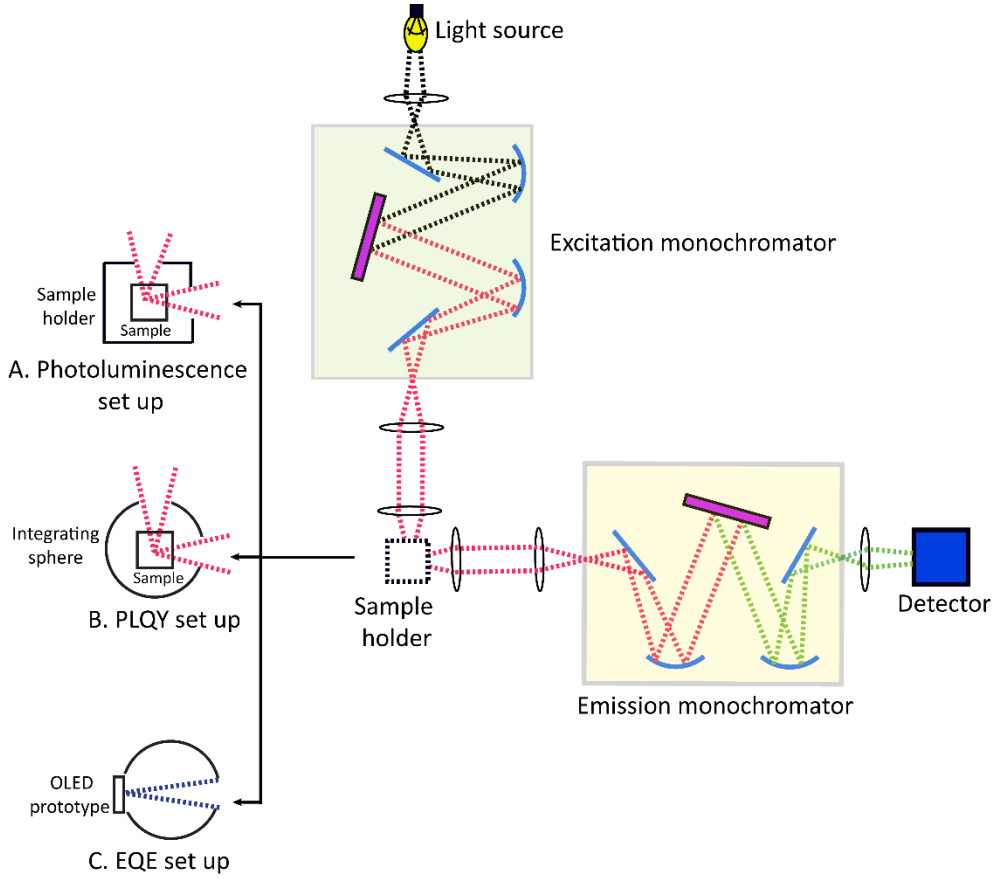

Figure 1.12. A simplified schematic diagram of a spectrofluorometer with sample holder options. Sample holder set-up for fluorescence (A), absolute quantum yield (B), and OLED prototype performance testing (C).

1.9.3. Cyclic Voltammetry (CV)

CV is a versatile electrochemical technique in which electronic properties of an analyte are obtained by measuring the current as a function of an applied voltage. Experimental estimation of the HOMO and LUMO energies of organic semiconductors is achieved by analyzing their CV characteristics.[80] For OLED emitters, the energy of HOMO denotes the minimum energy required to extract an electron (therefore generating a 'hole') from the emitter, which is an oxidation

process. Similarly, the energy of LUMO denotes the minimum energy required to inject an electron into the emitter, which is a reduction process.

A simplified CV set up is illustrated in Figure 1.13 (A), which employs an electrochemical cell containing three electrodes, i.e., working, counter, and reference electrodes. Potentiostat measures the current flow between the working electrode (WE) and the counter electrode (CE), as well as regulates and monitors the difference in potential between the WE and the reference electrode (RE).[80] In a typical CV experiment, the sample to be analyzed is dissolved in a degassed solvent containing an inert supporting electrolyte to effectively conduct current. Then, the electrodes are immersed in this solution. Next, the potential of the WE is ramped linearly to the positive direction and to the negative direction at a given scan rate, while measuring the current between WE and CE.[80] As shown in Figure 1.13 (B), a typical single electron oxidation-reduction (redox) process of a compound produces cathodic and anodic peaks, and the corresponding peak potentials are denoted as the anodic/oxidation peak potential (E_{pa}) and the cathodic/reduction peak potential (E_{pc}). This redox process is often measured relative to ferrocene/ferricenium (Fc/Fc^{+}) redox couple.[76,77] Consequently, the HOMO and LUMO energies of a compound are determined by employing equations 1.4 and 1.5.[76,77] If the compound has a quasi-reversible cyclic voltammogram, equation 1.2 is employed to obtain the energy of the 'non-visible' frontier orbital.

$$HOMO = -1e\left[E_{ox.\ onset\ vs\ Fc/Fc+} + 4.71\right]eV \quad (1.4)$$

$$LUMO = -1e\left[E_{red.\ onset\ vs\ Fc/Fc+} + 4.71\right]eV \quad (1.5),$$

where E_{ox} and E_{red} are onset values of the oxidation and reduction peaks of the compound with respect to Fc/Fc^{+}, and 4.71 eV is the formal potential of the Fc/Fc^{+} redox couple.[76,77]

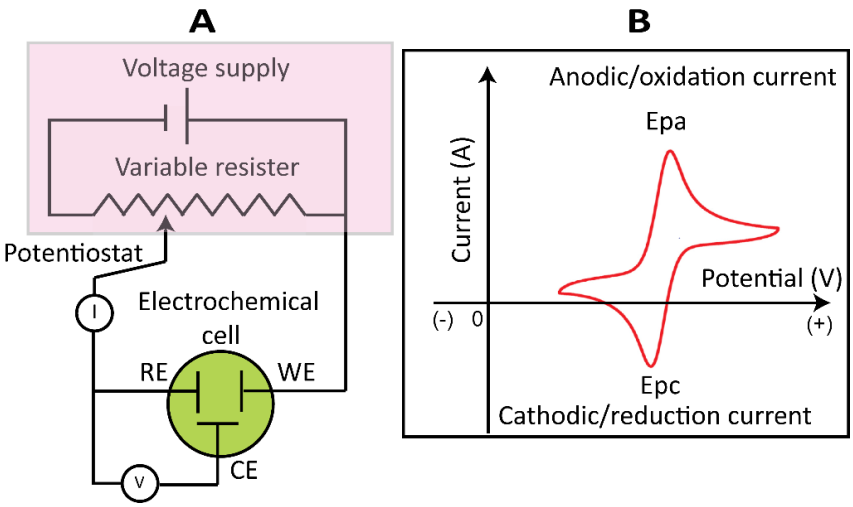

Figure 1.13. Schematic diagram of CV instrumentation (A) and a typical voltammogram for a single electron redox process (B).

1.9.4. X-Ray Diffraction (XRD) Studies

Solid-state/film morphology is a very important piece of information for understanding the photo-physical properties of OLED emitters. Therefore, XRD techniques such as single crystal X-ray diffraction (single crystal XRD), powder X-ray diffraction (PXRD), grazing-incidence small-angle X-ray scattering (GISAXS), and grazing-incidence wide-angle X-ray scattering (GIWAXS) are routinely used to elucidate emitter characteristics.[81-84] X-rays interact with the sample in the form of a single crystal, a powder, or a thin film, and diffract with constructive and destructive interferences determined by Bragg's law, which refers to equation 1.7.[81,82]

$$n\lambda = 2d\ sin\ \theta \qquad (1.6),$$

where n is a positive integer, d is lattice spacing, λ is the wavelength of the incident X-ray, and Θ is the scattering angle.

Figure 1.14 schematically illustrate the components of a typical X-ray diffractometer. XRD patterning is indicative of the electron density of the atoms and bonds within the molecules, and thus, analyzing the diffraction pattern of a compound provides solid-state structural information. Single crystal XRD provides absolute structure and detailed information on molecular packing,

such as bond lengths and angles, and the molecular conformation of compounds in the form of single crystals, whereas PXRD provides the degree of crystallinity of compounds in powder form/crystallites. GIWAXS offers information regarding thin film morphology, therefore providing more realistic information on the morphology of materials when applied in OLED devices as thin films.

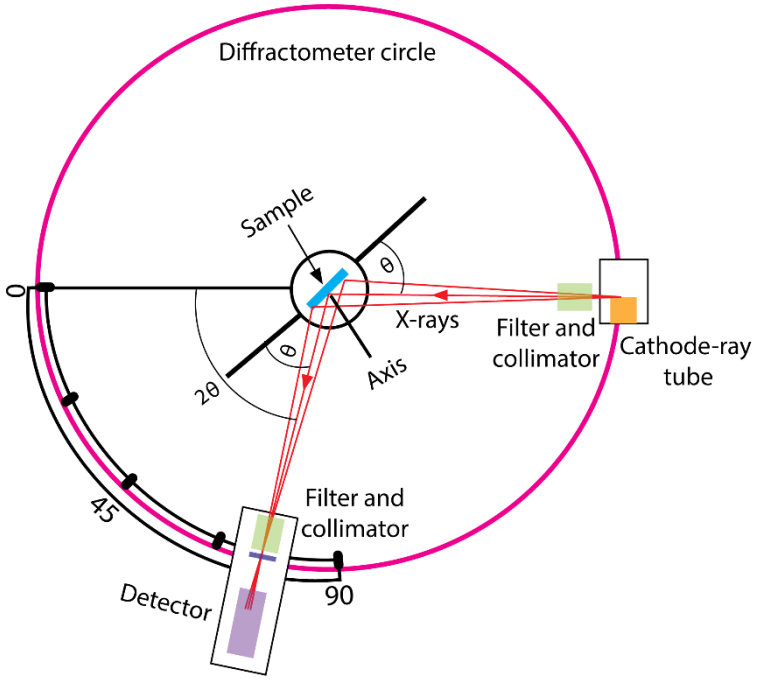

Figure 1.14. Schematic diagram of an X-ray diffractometer.

1.9.5. OLED Performance Characteristics

Since OLEDs are optoelectronics, they are evaluated in terms of both optical and electrical performance metrics. Optical characteristics include the exact color of the electroluminescence observed from device in terms of Commission Internationale de L'Eclairage (CIE) spectral coordinates, luminance, luminous efficiency, and external/internal quantum efficiencies, whereas the electrical properties of OLEDs include current and power efficiencies.[11]

1.9.5.1. CIE 1931 Spectral Coordinates

The color of an object is identified by the human eye in terms of hue, brightness, and saturation.[85,86] For color vision, the human eye utilizes three types of cone photoreceptor cells in the retina corresponding roughly to blue with absorption maximum (λ_{abs}) at 445 nm, green (λ_{abs} 535 nm), and red (λ_{abs} 575 nm).[86] By distribution, approximately 64% of cones are red sensitive, 32% are green sensitive, and only 2% are sensitive to blue.[86] The CIE 1931 spectral coordinates utilizes red, green, and blue primary color stimuli responses (tristimulus values) of the human eye as shown in Figure 1.15 (A) as weighing functions for a given color stimulus.[85-87] Accordingly, the corresponding color for a given color stimulus that can be seen by the human eye is characterized by CIE coordinates based on a two dimensional color space known as the 1932 CIE chromaticity diagram containing all colors that can be distinguished by the human eye as depicted in Figure 1.15 (B).[87]

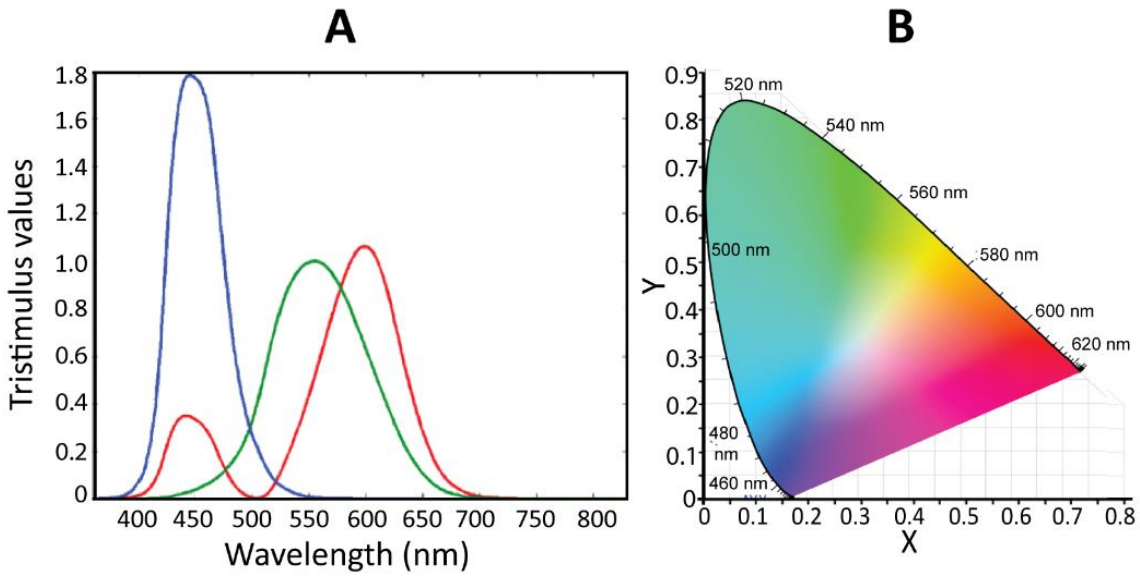

Figure 1.15. The RGB primary color stimuli response (tristimulus values) curves (A) and the 1931 CIE chromaticity coordinates diagram (B).

CIE spectral coordinate criterion for a blue emitter in an electronic display with RGB sub-pixel design is ($y < 0.15$, $(x + y) < 0.30$).[23] However, National Television System Committee (NTSC)

and European Broadcast Union (EBU) require much spectrally pure blue emitters for RGB sub-pixel design based electronic displays, particularly television screens, with CIE coordinates of (0.14, 0.08) and (0.15,0.06), respectively.[24,88] Interestingly, light blue emitters are used in a non-conventional electronic display that contains a sub-pixel design known as red-green-light blue-deep blue (RGB_1B_2) that invented by Universal Display Corporation (USA) as shown in Figure 1.16.[89,90] This novel RGB_1B_2 sub pixel design have advantages including significant power saving, improved device lifespan, and minimum emission of harmful near UV radiation.[90-92]

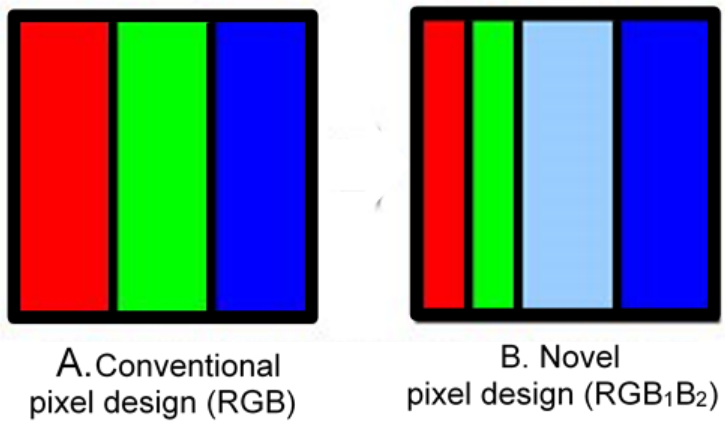

Figure 1.16. Sub-pixel designs of electronic screens, conventional RGB (A) and novel RGB_1B_2 (B) designs.

1.9.5.2. Luminance and Luminance Power Efficiency

OLEDs in electronic screens primarily interact with human eyes. Therefore the amount of light emitted per unit surface area of an OLED is needed to weigh the visual response of the human eye and is termed the luminance.[11,26] In order to weigh OLED light output by the day vision/photopic vision of the human eye, a standardized spectral response curve of an average human eye based on photopic vision, known as the photopic response curve, is used, which was determined by the CIE in 1924 (Figure 1.17).[11,26]

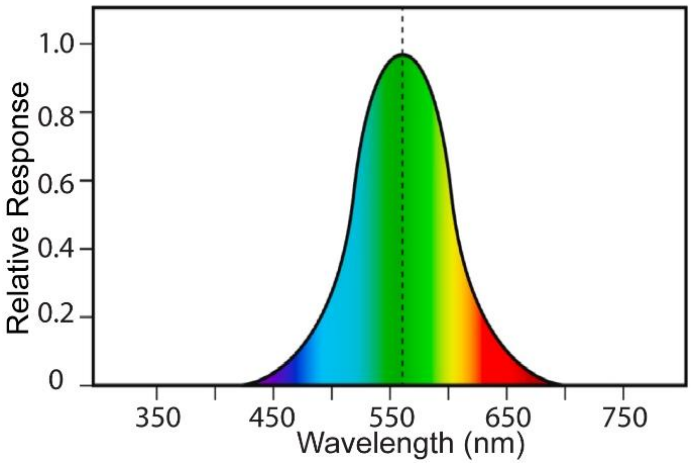

Figure 1.16. Photopic response curve for the human eye (dashed line is showing maximum eye response at 555 nm).

Luminance is often recorded as candelas per square meter (cdm^{-2}).[26] Luminance power/ luminous power efficiency/power efficiency is the ratio of the emitted luminous flux (weighed by the photopic response) to radiant flux.[11,26] Luminous power efficiency provides an insight into the energy consumption of an OLED producing visible light and is often recorded as lumens per Watt (lmW^{-1}). For a Lambertian emitter, luminous power efficiency can be calculated using Equation 1.7.[11,26]

$$\text{Luminous Power Efficiency} = \frac{\pi \times L}{J \times V} \qquad (1.7),$$

where L is the luminance (cdm^{-2}), J is the current density (Am^{-2}), and V is the applied voltage (V).

1.9.5.3. Current Efficiency

Current efficiency provides insight into the light emitting ability of an OLED and is often recorded in units of cdA^{-1}. Current efficiency can be calculated using Equation 1.8.[11,26]

$$\text{Current Efficiency (CE)} = \frac{L}{J} \qquad (1.8),$$

where L is luminance (cdm^{-2}), and J is current density (Am^{-2}).

1.9.5.4. Internal and External Quantum Efficiencies

Quantum efficiency provides an insight into the exciton harvesting efficiency of an OLED and is defined as the ratio of emitted photons to injected charges. The internal quantum efficiency (IQE) is the ratio of the emitted photons generated within the OLED to the number of injected charges, whereas external quantum efficiency (EQE) is the ratio of emitted photons into the viewing direction to injected charges.[26] Therefore, EQE is only a fraction of IQE, and the relationship between IQE and EQE is given by equation 1.9.

$$\mathrm{EQE} = \mathrm{IQE} \times \eta \qquad (1.9),$$

where η is the fraction of light coupled out of the OLED into the viewing direction. For a standard bottom emitting OLED, η is typically considered as 0.2.[26,30,89] However, EQE is more useful than IQE, since the human eye can only utilize the light extracted out from the OLED. Furthermore, IQE measurements can be more tedious and less accurate, especially if the emitted photons are re-absorbed and/or re-emitted at a longer wavelength by organic layers.[26]

1.10. The Scope of this Dissertation

This dissertation is focused on the design, synthesis, and characterization of novel OLED emissive materials, with an emphasis on blue emitters for electronic displays derived from small organic molecules and GUMBOS. Accordingly, chapter two includes a novel sky-blue light emitting compound, 2,4,6-tri(1-pyrenyl)pyridine (2,4,6-TPP), and three dipyrenylpyridines, [2,4-di(1-pyrenyl)pyridine (2,4-DPP), 2,6-di(1-pyrenyl)pyridine (2,6-DPP), and 3,5-di(1-pyrenyl)pyridine (3,5-DPP)], which were systematically evaluated for solution and solid-state characteristics, such as spectroscopy, electrochemistry, photothermal stability, and solid-state morphology. Also, chapter two presents design, fabrication, and a device performance evaluation of a non-doped OLED prototype with 2,4,6-TPP as the emissive layer.

The third chapter describes three novel blue emitters derived from pyrene-benzimidazole conjugates: 2-(1,2-diphenyl)-1*H*-benzimidazole-7-*tert*-butylpyrene (compound A), 1,3-di(1,2-diphenyl)-1*H*-benzimidazole-7-*tert*-butylpyrene (compound B), and 1,3,6,8-tetra(1,2-diphenyl)-1*H*-benzimidazolepyrene (compound C). These compounds were also evaluated for suitability for OLED applications as blue emitters, and the characterization methods and OLED prototype evaluation are similar to that in chapter 2.

In chapter 4, a well-known red fluorescent dye, propidium iodide (3,8-diamino-5-[3-(diethylmethylammonio)propyl]-6- phenylphenanthridinium diiodide, [P][I]), is converted to GUMBOS by replacing iodide counteranions of [P][I] with three organic anions: trifluoromethanesulfonate/[TfO], bis((trifluoromethyl)sulfonyl)imide/[NTf_2], and bis((perfluoroethane)sulfonyl)imide/[BETI]. Then, the morphological, spectral, physical, chemical, and electronic properties of these novel GUMBOS materials were thoroughly investigated and compared with the parent compound [P][I] to understand the impact of counterion variations on ionic luminophores.

1.11. References

1. Hedley, G. J.; Ruseckas, A.; Samuel, I. D. W.: Light harvesting for organic photovoltaics. *Chemical Reviews* **2017**, *117*, 796-837.

2. Peumans, P.; Yakimov, A.; Forrest, S. R.: Small molecular weight organic thin-film photodetectors and solar cells. *Journal of Applied Physics* **2003**, *93*, 3693-3723.

3. Baeg, K.-J.; Binda, M.; Natali, D.; Caironi, M.; Noh, Y.-Y.: Organic light detectors: photodiodes and phototransistors. *Advanced Materials* **2013**, *25*, 4267-4295.

4. Thejo Kalyani, N.; Dhoble, S. J.: Organic light emitting diodes: Energy saving lighting technology–A review. *Renewable and Sustainable Energy Reviews* **2012**, *16*, 2696-2723.

5. Gupta, A. S.: *Organic Light Emitting Diodes (OLEDs): Technologies and Global Markets*; BCC Research, Massachusetts, USA, **2015**; pp. 7-14, 90-120.

6. Bernanose, A.; Comte, M.; Vouaux, P.: A new method of emission of light by certain organic compounds. *Journal de Chimie Physique et de Physico-Chimie Biologique* **1953**, *50*, 64-68.

7. Tang, C. W.; Van Slyke, S.A.: Organic electroluminescent diodes. *Applied Physics Letters* **1987**, *51*, 913-915.

8. OLED Info: The OLED Experts Official Website. https://www.oled-info.com/devices (accessed January 2, 2018).

9. Acuitybrands Official Website. https://hydrel.acuitybrands.com/sitecore/content/acuitybrandscorporate/home/oled/why-oled (accessed July 12, 2018).

10. Martens, R.: *The OLED Handbook: a Guide to OLED Technology, Industry & Market*; LULU Press, North Carolina, USA, **2014**; pp. 11-36.

11. Su, W. Printed organic light emission and display. In *Printed Electronics*; Editors Cui, Z.; John Wiley & Sons; New York, USA, **2016**; pp. 251-260.

12. LG Official Website. www.lgoledlight.com/blue-light-hazard-for-the-human-eye/ (accessed August 3, 2018).

13. Lin, H.; Bai, F. Electronic process in organic solids. In *Organic Optoelectronics;* Editors Hu, W.; Wiley-VCH Verlag GmbH & Co.; Weinheim, Germany, **2013**; pp 27-29.

14. Petty, M. C.: *Molecular Electronics: From Principle to Practice*, John Wiley & Sons; West Sussex, UK; **2007**, pp. 135-147.

15. Baldo, M. A.; O'Brien, D. F.; You, Y.; Shoustikov, A.; Sibley, S.; Thompson, M. E.; Forrest, S. R.: Highly efficient phosphorescent emission from organic electroluminescent devices. *Nature* **1998**, *395*, 151-154.

16. Koden, M.: *OLED Displays and Lighting*, John Wiley & Sons; West Sussex, UK, **2017**; pp. 1-144.

17. Fröbel, M.; Fries, F.; Schwab, T.; Lenk, S.; Leo, K.; Gather, M. C.; Reineke, S.: Three-terminal RGB full color OLED pixels for ultrahigh density displays. *Scientific Reports* **2018**, *8*, 9684.

18. Cao, W.; Li, J.; Chen, H.; Xue, J.: Transparent electrodes for organic optoelectronic devices: a review. *Journal of Photonics for Energy* **2014**, *4*, 040990.

19. Wu, C.-C.; Chen, C.-W.; Lin, C.-L.; Yang, C.-J.: Advanced organic light-emitting devices for enhancing display performances. *Journal of Display Technology* **2005**, *1*, 248-266.

20. Zhang, Q. S.; Li, J.; Shizu, K.; Huang, S. P.; Hirata, S.; Miyazaki, H.; Adachi, C.: Design of efficient thermally activated delayed fluorescence materials for pure blue organic light emitting diodes, *Journal of the American Chemical Society* **2012**, *134*, 14706-14709.

21. Karzazi, Y.: Organic light emitting diodes: devices and applications. *Journal of Materials and Environmental Science* **2014**, *5*, 1-12.

22. Adachi, C.; Tsutsui, T.; Saito, S.: Blue light-emitting organic electroluminescent devices. *Applied Physics letters* **1990**, *56*, 799-801.

23. Zhu, M.; Yang, C.: Blue fluorescent emitters: Design tactics and applications in organic light-emitting diodes. *Chemical Society Reviews* **2013**, *42*, 4963-4976.

24. Yang, X.; Xu, X.; Zhou, G.: Recent advances of the emitters for high performance deep-blue organic light-emitting diodes. *Journal of Material Chemistry C* **2015**, *3*, 913-944.

25. Jou, J.-H.; Kumar, S.; Agarwal, A.; Lia, T.-H.; Sahoo, S.: Approaches for fabricating high efficiency organic light emitting diodes. *Journal of Materials Chemistry C* **2015**, *3*, 2974-3002.

26. Forrest, S. R.; Bradley, D. D. C.; Thompson, M. E.: Measuring the efficiency of organic light-emitting devices. *Advanced Materials* **2003**, *15*, 1043-1048.

27. Kondakov, D. Y.; Pawlik, T. D.; Hatwar, T. K.; Spindler, J. P.: Triplet annihilation exceeding spin statistical limit in highly efficient fluorescent organic light-emitting diodes. *Journal of Applied Physics* **2009**, *106*, 124510.

28. Nakanotani, H.; Higuchi, T.; Furukawa, T.; Masui, K.; Morimoto, K.; Numata, M.; Tanaka, H.; Sagara, Y.; Yasuda, T.; Adachi, C.: High efficiency organic light-emitting diodes with fluorescent emitters. *Nature Communications* **2014**, *5*, 4016.

29. Lakovicz, J. R.: *Principles of Fluorescence Spectroscopy*; Kluwer Academic/Plenum Publishers: New York, USA, **1999;** pp. 1-23, 95-116.

30. Sun, Y.; Forrest, S. R.: Enhanced light out-coupling of organic light-emitting devices using embedded low-index grids. *Nature Photonics* **2008**, *2*, 483-487.

31. Adachi, C.; Baldo, M. A.; Thompson, M. E.; Forrest, S. R.: Nearly 100% internal phosphorescence efficiency in an organic light-emitting device. *Journal of Applied Physics* **2001**, *90*, 5048.

32. Kawamura, Y.: 100% phosphorescence quantum efficiency of Ir(III)Ir(III) complexes in organic semiconductor films. *Applied Physics Letters* **2005**, *86*, 071104.

33. Xiao, L. X.; Su, S. J.; Agatha, Y.; Lan, H. L.; Kido, J.: Nearly 100% Internal quantum efficiency in an organic blue-light electrophosphorescent device using a weak electron transporting material with a wide energy gap. *Advanced Materials* **2009**, *21*, 1271-1274.

34. Endo, A.; Ogasawara, M.; Takahashi, A.; Yokoyama, D.; Kato, Y.; Adachi, C.: Thermally activated delayed fluorescence from Sn^{4+}-porphyrin complexes and their application to organic

light emitting diodes-A novel mechanism for electroluminescence. *Advanced Materials* **2009**, *21*, 4802-4806.

35. Yang, Z.; Mao, Z.; Xie, Z.; Zhang, Y.; Liu, S.; Zhao, J.; Xu, J.; Chi, Z; Aldred, M. P.: Recent advances in organic thermally activated delayed fluorescence materials. *Chemical Society Reviews* **2017**, *46*, 915-1016.

36. Im, Y.; Kim, M.; Cho, Y. J.; Seo, J.-A.; Yook, K. S.; Lee, J. Y. Molecular design strategy of organic thermally activated delayed fluorescence emitters. *Chemistry of Materials* **2017**, *29*, 1946-1963.

37. Miwa, T.; Kubo, S.; Shizu, K.; Komino, T.; Adachi, C.; Kaji, H.: Blue organic light-emitting diodes realizing external quantum efficiency over 25% using thermally activated delayed fluorescence emitters. *Nature Scientific Reports* **2017**, *2*, 284.

38. Parker, C. A.; Hatchard, C. G.: Delayed fluorescence from solutions of anthracene and phenanthrene. *Proceedings of the Royal Society A, Mathematical and Physical Sciences* **1962**, *269*, 574-584.

39. Kondakov, D. Y.; Pawlik, T. D.; Hatwar, T. K.; Spindler, J. P.: Triplet annihilation exceeding spin statistical limit in highly efficient fluorescent organic light-emitting diodes. *Journal of Applied Physics* **2009**, *106*, 124510.

40. Popovic, Z. D.; Aziz, H.: Delayed electroluminescence in small-molecule-based organic light-emitting diodes: Evidence for triplet-triplet annihilation and recombination-center-mediated light-generation mechanism. *Journal of Applied Physics* **2005**, *98*, 013510.

41. Kondakov, D. Y.: Triplet–triplet annihilation in highly efficient fluorescent organic light-emitting diodes: Current state and future outlook. *Philosophical Transactions of the Royal Society of London A, Mathematical, Physical and Engineering Sciences* **2015**, *373*, 20140321.

42. Adachi, C.; Kwong, R. C.; Djurovich, P.; Adamovich, V.; Baldo, M. A.; Thompson, M. E.; Forrest, S. R.: Endothermic energy transfer: A mechanism for generating very efficient high-energy phosphorescent emission in organic materials. *Applied Physics Letters* **2001**, *79*, 2082-2084.

43. Lee, S.; Kim, S.-O.; Shin, H.; Yun, H.-J.; Yang, K.; Kwon, S, K.; Kim,J.-J.; Kim, Y.-H.: Deep-blue phosphorescence from perfluoro carbonyl-substituted iridium complexes. *Journal of the American Chemical Society* **2013**, *135*, 14321-14328.
44. Chou, H.-H.; Cheng, C.-H.: A Highly efficient universal bipolar host for blue, green, and red phosphorescent OLEDs. *Advanced Materials* **2010**, *22*, 2468-2471.

45. Fleetham, T.; Wang, Z.; Li, J.: Efficient deep blue electrophosphorescent devices based on platinum(II) bis(n-methyl-imidazolyl)benzene chloride. *Organic Electronics* **2012**, *13*, 1430-1435.

46. Fleetham, T.; Li, G.; Wen, L.; Li, J.: Efficient “pure” blue OLEDs employing tetradentate Pt complexes with a narrow spectral bandwidth, *Advanced Materials* **2014**, *26*, 7116-7121.

47. Li, K.; Guan, X.; Ma, C.-W.; Lu, W.; Chen, Y.; Che, C.-M.: Blue electrophosphorescent organoplatinum(II) complexes with dianionic tetradentate bis(carbene) ligands. *Chemical Communications* **2011**, *47*, 9075-9077.

48. Schmidbauer, S.; Hohenleutner, A.; König, B.: Chemical degradation in organic light-emitting devices: Mechanisms and implications for the design of new materials, *Advanced Materials* **2013**, *25*, 2114-2129.

49. Hu, J.-Y.; Yamato, T.: Synthesis and photophysical properties of pyrene-based multiply conjugated shaped light-emitting architectures: Toward efficient organic-light-emitting diodes. In *Organic Light Emitting Diode - Material, Process and Devices*; Editors Ko, S. H.; InTech: Rijeka, Croatia, **2011**; pp 22-54.

50. Tao, S.; Zhou, Y.; Lee, C.-S.; Zhang, X.; Lee, S.-T.: High-efficiency nondoped deep-blue-emitting organic electroluminescent device, *Chemistry of Materials* **2010**, *22*, 2138-2141.

51. Xing, X.; Xiao, L.; Zheng, L.; Hu, S.; Chen, Z.; Qu, B.; Gong, Q.: Spirobifluorene derivative: a pure blue emitter (CIEy = 0.08) with high efficiency and thermal stability, *Journal of Materials Chemistry* **2012**, *22*, 15136-15140.

52. Ye, J.; Chen, Z.; Fung, M.-K.; Zheng, C.; Ou, X.; Zhang, X.; Yuan, Y.; Lee, C.-S.: Carbazole/sulfone hybrid D-π-A-structured bipolar fluorophores for high-efficiency blue-violet electroluminescence. *Chemistry of Materials* **2013** *25*, 2630-2637.

53. Yu, D.; Zhao, F.; Zhang, Z.; Han, C.; Xu, H.; Li, J.; Ma, D.; Yana, P.: Insulated donor–p–acceptor systems based on fluorene-phosphine oxide hybrids for non-doped deep-blue electroluminescent devices. *Chemical Communications* **2012**, *48*, 6157-6159.

54. Zhao, Z.; Chen, S.; Lam, J. W. Y.; Wang, Z.; Lu, P.; Mahtab, F.; Sung, H. H. Y.; Williams, I. D.; Ma, Y.; Kwok, H. S.; Tang, B. Z.: Pyrene-substituted ethenes: aggregation-enhanced excimer emission and highly efficient electroluminescence. *Journal of Materials Chemistry* **2011**, *21*, 7210-7216.

55. Zhang, Y.; He, B.; Liu, J.; Hu, S.; Pan, L.; Zhao, Z.; Tang, B. Z.: Aggregation-induced emission and the working mechanism of 1-benzoyl and 1-benzyl pyrene derivatives. *Physical Chemistry Chemical Physics* **2018**, *20*, 9922-9929.

56. Burroughes, J. H.; Bradley, D. D. C.; Brown, A. R.; Marks, R. N.; Mackay, K.; Friend, R. H.; Burns, P. L.; Holmes, A. B.: Light-emitting diodes based on conjugated polymers. *Nature* **1990**, *347*, 539-541.

57. Giovanella, U.; Botta, C.; Galeotti, F.; Vercelli, B.; Battiato, S.; Pasini, M.: Perfluorinated polymer with unexpectedly efficient deep blue electroluminescence for full-colour OLED displays and light therapy applications. *Journal of Materials Chemistry C* **2013**, *1*, 5322-5329.

58. Zhu, Y.; Gibbons, K. M.; Kulkarni, A. P.; Jenekhe, S. A.: Polyfluorenes containing dibenzo[a,c]phenazine segments: Synthesis and efficient blue electroluminescence from intramolecular charge transfer states. *Macromolecules* **2007**, *40*, 804-813.

59. Liu, F.; Lai, W.-Y.; Tang, C.; Wu, H.-B.; Chen, Q.-Q.; Peng, B.; Wei, W.; Huang, W.; Cao, Y.: Synthesis and characterization of pyrene-centered starburst oligofluorenes. *Macromolecular Rapid Communications* **2008**, *29*, 659-664.

60. Zhen, C. G.; Dai, Y. F.; Zeng, W. J.; Ma, Z.; Chen, Z. K.; Kieffer, J.: Achieving highly efficient fluorescent blue organic light-emitting diodes through optimizing molecular structures and device configuration. *Advanced Functional Materials* **2011**, *21*, 699-707.

61. Liu, C; Li, Y.; Li, Y.; Yang, C.; Wu, H.; Qin, J.; Cao, Y.: Efficient solution-processed deep-blue organic light-emitting diodes based on multibranched oligofluorenes with a phosphine oxide center.: *Chemistry of Materials* **2013**, *25*, 3320-3327.

62. Warner, I. M.; El-Zahab, B.; Siraj, N.: Perspectives on moving ionic liquid chemistry into the solid phase. *Analytical Chemistry* **2014,** *86*, 7184-7191.

63. Magut, P. K. S.; Das, S.; Fernand, V. E.; Losso, J.; McDonough, K.; Naylor, B. M.; Aggarwal, S.; Warner, I. M.: Tunable cytotoxicity of rhodamine 6G via anion variations. *Journal of the American Chemical Society* **2013**, *135*, 15873-15879.

64. Al Ghafly, H.; Siraj, N.; Das, S.; Regmi, B. P.; Magut, P. K. S.; Galpothdeniya, W. I. S.; Murray, K. K.; Warner, I. M.: GUM BOS matrices of variable hydrophobicity for matrix-assisted laser desorption/ionization mass spectrometry. *Rapid Communications of Mass Spectrometry* **2014**, *28*, 2307-2314.

65. Regmi, B. P.; Galpothdeniya, W. I. S.; Siraj, N.; Webb, M. H.; Speller, N. C.; Warner, I. M.: Phthalocyanine- and porphyrin-based GUMBOS for rapid and sensitive detection of organic vapors. *Sensors and Actuator B-Chemical* **2015,** *209*, 172-179.

66. Jordan, A., Das, S.; de Rooy, S. L.; Li, M.: El-Zahab, B.; Chandler, L.; Baker, G. A.; Warner, I. M.: Anion-controlled morphologies and spectral features of cyanine-based nano-GUMBOS-An improved photosensitizer. *Nanoscale* **2011**, *4*, 5031-5038.

67. Siraj, N.; Hassan, F.; Das, S.; Kiruri, L.; Steege Gall, K. E.; Baker, G. A.; Warner, I. M.: Carbazole-derived group of uniform materials based on organic salts: Solid state fluorescent analogues of ionic liquids for potential applications in organic-based blue light-emitting diodes. *Journal of Physical Chemistry C* **2014**, *118*, 2312-2320.

68. Leontiev, A. V.; Serpell, C. J.; White, N. G.; Beer, P. D. Cation-induced molecular motion of spring-like [2]catenanes. *Chemical Science* **2011**, *2*, 922-927.

69. Del Sesto, R. E.; McCleskey, T. M.; Burrell, A. K.; Baker, G. A.; Thompson, J. D.; Scott, B. L.; Wilkes, J. S., Williams, P. Structure and magnetic behavior of transition metal based ionic liquids. *Chemical Communications* **2008**, *0*, 447-449.

70. Förster, T.: Zwischenmolekulare energiewanderung und fluoreszenz. Annalen Der Physik **1948**, *437*, 55-57.

71. Dexter, D. L.: A theory of sensitized luminescence in solids. *The Journal of Chemical Physics* **1953**, *21*, 836.

72. Lin, W.-C.; Lin, Y.-C.; Wang, W.-B.; Yu, B.-Y.; Lida, S.-I.; Tozu, M.; Hsu, M.-F.; Jou, J.-H.; Shyue, J.-J.: Effect of fabrication process on the microstructure and the efficiency of organic light-emitting diodes. *Organic Electronics* **2009**, *10*, 459-464.

73. Semicore Official Website. https://www.semicore.com/news/71-thin-film-deposition-thermal-evaporation (accessed January 2, 2018).

74. Gaj, M. P. High performance organic light-emitting diodes for flexible and wearable electronics. Ph.D. Dissertation, Georgia Tech University, April 2016.

75. Turro, N. J.; Ramamurthy, V.; Scaiano, J.: *Modern Molecular Photochemistry of Organic Molecules*; University Science Books, Virginia, USA **2010**; pp 109-136.

76. Zhou, Y.; He, Q.; Yang, Y.; Zhong, H.; He, C.; Sang, G.; Liu, W.; Yang, C.; Bai, F.; Li, Y.: Binaphthyl-containing green- and red-emitting molecules for solution-processable organic light-emitting diodes. *Advanced Functional Materials* **2008**, *18*, 3299-3306.

77. Cardona, C. M.; Li, W.; Kaifer, A. E.; Stockdale, D.; Bazan, G. C.: Electrochemical considerations for determining absolute frontier orbital energy levels of conjugated polymers for solar cell applications. *Advanced Materials* **2011**, *23*, 2367-2371.

78. Wurth, C.; Grabolle, M.; Pauli, J.; Spieles, M.; Resch-Genger, U.: Relative and absolute determination of fluorescence quantum yields of transparent samples. *Nature Protocols* **2013**, *8*, 1535-1550.

79. Brouwer, A. M.: Standards for photoluminescence quantum yield measurements in solution (IUPAC technical report). *Pure and Applied Chemistry* **2011**, *83*, 2213-2228.

80. Bard, A. J.; Faulkner, L. R.: *Electrochemical Methods Fundamentals and Applications*; John Wiley & Sons, New York, USA **2001**; pp 56-89.

81. International Union of Crystallography Official Website. https://www.iucr.org/education/pamphlets/2 (accessed July 15, 2018).

82. Waseda, Y.; Mastubara, E.; Shinoda, K.: *X-Ray Diffraction Crystallography; Introduction, Examples and Solved Problems*; Springer-Verlag Berlin Heidelberg: Germany, **2011**; pp 12-45.

83. Busch, P.; Rauscher, M.; Smilgies, D.-M.; Posselt, D.; Papadakis, C.: Grazing incident small-angle x-ray scattering (GISAXS) as a tool for the investigation of thin nanostructured block copolymer films- The scattering cross-section in the distorted wave Born approximation. *Journal of Applied Crystallography* **2006**, *39*, 433-442.

84. Hexemer, A.; Muller-Buschbaum, P.: Advanced grazing-incidence techniques for modern soft-matter materials analysis. *International Union of Crystallography* **2015**, *2* (Pt 1), 106-125.

85. Boynton, R. M. Human color perception. In *Science of Vision*; Editors Leibovic, K. N.; Springer; New York, USA, **1990**, pp. 211-253.

86. Hyperphysics Official Website. https://www.hyperphysics.phy-astr.gsu.edu/hbase/vision/colcon/html#c1 (accessed July 23, 2018).

87. Smith, T.; Guild, J.: The C.I.E. colorimetric standards and their use. *Transactions of the Optical Society* **1932**, *33*, 73-134.

88. Yu, D.; Zhao, F.; Zhang, Z.; Han, C.; Xu, H.; Li, J.; Ma, D.; Yan, P. Insulated donor-π-acceptor systems based on fluorine-phosphine oxide hybrids for non-doped deep-blue electroluminescence devices. *Chemical Communications* **2012**, *49*, 6157-6159.

89. Reineke, S.; Lindner, F.; Schwartz, G.; Seidler, N.; Walzer, K.; Lussem, B.; Leo, K. White organic light-emitting diodes with fluorescent tube efficiency. *Nature* 2009, *459*, 234-238.

90. Hack, M.; Brown, J. J.; Weaver, M. S.; D' Andrade, B. OLED Display Architecture. U.S. Patent 9385167, July 5, 2016.

91. https.//www.oled-info.com/udc-show-new-light-blue-emitter-that-can-be-used-white-oleds-or-four-sub-pixel-displays (accessed February 4, 2019).

92. https.//www.oled-info.com/udc-our-rgb1b2-amoled-architecture-minimizes-blue-light-hazard (accessed February 24, 2019).

CHAPTER II. PYRENYLPYRIDINES: SKY-BLUE EMITTERS FOR ORGANIC LIGHT EMITTING DIODES

2.1. Introduction

OLEDs occupy a significant niche in organic semiconductor-based technology, representing a promising means for next generation electronic displays and solid-state lighting. Accordingly, an estimated global market share of $9.6 billion is expected by the year 2020 for OLEDs.[1] Perceived popularity of OLED displays over LCDs is attributable to numerous cutting-edge advantages offered by OLEDs such as lower power consumption, self-emission, greater color gamut, high resolution, high contrast, light weight, flexibility, transparency, and broader viewing angles.[1,2] Full color OLED displays often require emitters for the three primary colors (red, green, and blue). However, the intrinsically wide HOMO-LUMO energy gap of blue emitters causes it to suffer from inefficient charge injection and rapid deterioration of the emissive layer upon excitation.[3,4] Consequently, blue emitters typically show inferior operational lifetime, efficiency, and color purity than red and green emitters.[1] The limited availability of efficient, photothermally and chemically stable, spectrally pure, and highly processable organic blue emitters constitutes a major challenge for the progress of OLED technology. Unfortunately, this is a prevalent problem among blue emitters with all kinds of molecular designs including polymers, oligomers, dendrimers, organometallics, and small organic molecules.[4] Among these molecular designs, small-molecular organic blue emitters have distinct advantages such as ease of synthesis, purification, characterization, modification, and OLED fabrication.[3,4] Majority of these small-molecular organic blue emitters are derived from PAH based luminophores such as anthracene, phenanthrene, fluorene, pyrene, carbazole, and indenopyrazine.[3-6] Among these luminophores, pyrene has a great potential as a blue emitter in OLEDs owing to high photothermal stability, favorable charge carrier properties, and spectral characteristics.[5,7] Consequently, number of

pyrene derivatives have already been reported as blue/green OLED emitters[7-12] as well as charge injectors/transporters in OLEDs.[7,13-18] More importantly, pyrene derivatives can be designed as multifunctional *p*-type, *n*-type, or bipolar emitters, ensuring efficient and balanced flux of charges to the emissive layer even with relatively simple device architectures.[7,19]

However, a major challenge of many pyrene-based emissive materials is controlling undesirable excimer formation, particularly in the condensed state. The nearly planer aromatic conjugated ring system of pyrene readily undergoes π-π stacking and excimer formation. As a result, emission of most pyrene derivatives significantly red-shifts and often undergo aggregation-induced quenching, which affects color purity and device efficiency.[7,20,21] A notable exception for aggregation-induced quenching of fluorescent dyes is AIE, that shows restriction of intramolecular rotation in the solid-state, thus improves emission efficiency in the solid-state.[22,23] However, our group prefer emitters with much chemically stable PAH based ring systems such as pyrenylpyridines discussed in this chapter than AIE emitters, in which, less chemically stable aliphatic double bonds and/or heteroatomic functional groups are often used.[22,23]

For non-AIE molecules derived from pyrene, mutually twisting pyrene substituents found to show less prevalent π-π stacking, and thus lower the excimer induced fluorescence quenching in solid-state.[17,20,24] For this reason, molecules with multiple pyrenyl moieties are designed in such a way that the pyrene units are attached to rigid bridging molecular platforms such as benzene, calixarene, and octavinylsilsesquioxane.[17,20,24] These molecular designs provide sufficient steric strain to mutually twist the pyrene units into a nearly orthogonal position with respect to each other. These twisted configurations electronically isolate intramolecular pyrene moieties to minimize extended conjugation, as well as reduces solid-state inter-molecular π-π stacking as a result of steric hindrance.[17,20,24] Accordingly, such molecular designs confine the luminophore

emission largely within the blue region of EMS while minimizing aggregation-induced quenching.[17]

In the study reported herein, four pyrenylpyridines were used as model compounds to evaluate the structure-property relationships of pyrene-containing small organic molecules. Among these pyrenylpyridines, 2,4-di(1-pyrenyl)pyridine (2,4-DPP), 2,6-di(1-pyrenyl)pyridine (2,6-DPP), and 3,5-di(1-pyrenyl)pyridine (3,5-DPP), each having two pyrene units, are thus collectively referred to as dipyrenylpyridines (DPPs), whereas 2,4,6-tri(1-pyrenyl)pyridine (2,4,6-TPP) has three pyrene units. Also, molecular symmetry of these structural isomers shows much diversity with 2,4-DPP and 2,4,6-TPP being asymmetric, while 2,6-DPP and 3,5-DPP are symmetric molecules. The pyridine unit is used as the bridging moiety to induce enough steric strain to intramolecularly twist pyrenyl moieties to control dye aggregation.

During the course of studies, it was noted that, despite the significantly twisted conformations of pyrenylpyridines, π-π stacking occurs in the solid-state to different extents, depending on multitude of factors such as molecular symmetry, solid-state conformation, and the extent of inter- and intramolecular interactions between the pyrene units. As a result, solid-state characteristics of pyrenylpyridines including absorption and photoluminescence spectra, fluorescence lifetimes, photoluminescence quantum yields, melting points, thermal decomposition onset temperatures, and the degree of crystallinity were found to be significantly different among these compounds, despite their structural similarity.

It is noted that the dipyrenylpyridine compounds, 3,5-DPP and 2,6-DPP have been previously reported as electron transporting materials, and 2,4-DPP has been previously mentioned in few patents.[13,25,26] However, to the best of our knowledge, these compounds have not been evaluated for suitability as blue OLED emissive materials. Furthermore, 2,4,6-TPP is a novel compound

that has not been described in the literature. This compound exhibited the most favorable characteristics for blue OLED emitters, including the highest photothermal stability and quantum yield, and the lowest degree of crystallinity, among the pyrenylpyridines investigated. Accordingly, a non-doped, bottom-emitting OLED prototype based on 2,4,6-TPP as the emissive layer was fabricated, that showed a sky-blue electroluminescence with a maximum EQE of 6 (±1.2) % at 5 V, which is close to the theoretical maximum limit for OLEDs based on conventional fluorescence.[4]

2.2. Experimental Section

2.2.1. Materials

The compounds, 1-pyrenylboronic acid, 2,4,6-tribromopyridine, 2,4-dibromopyridine, 2,6-dibromopyridine, and 1,3,5-tris(1-phenyl-1H-benzimidazole-2-yl)benzene (TPBI, sublimed grade) were purchased from Tokyo Chemical Industries Co. Ltd. (Portland, OR) and 1,4-dioxane was purchased from Acros Organics (West Chester, PA). Tetrakis(triphenylphosphine) palladium(0), tetrabutylammonium hexafluorophosphate ($TBAPF_6$), ferrocene (Fc), and N,N′-di(1-naphthyl)-N,N′-diphenyl-(1,1′-biphenyl)-4,4′-diamine (NPB, sublimed grade) were purchased from Sigma-Aldrich (St. Louis, MO), whereas 3,5-dibromopyridine was purchased from Alfa Aesar (Ward Hill, MA). Potassium carbonate (K_2CO_3) was purchased from Fisher Scientific (Fair Lawn, NJ). The analytical grade solvents, chloroform ($CHCl_3$), tetrahydrofuran (THF), hexane, acetone, isopropanol, ethyl acetate (EA), methanol (MeOH), dimethyl sulfoxide (DMSO), acetonitrile (ACN), and dichloromethane (DCM), were purchased from Macron (Center Valley, PA). Aluminum (Al) and calcium (Ca) were purchased from Angstrom Engineering Inc. (99.999%, Kitchener, ON). Indium tin oxide (ITO) coated glass (sheet resistance of 8-12 Ohm $square^{-1}$) was purchased from Delta Technologies (Loveland, CO). Column chromatography was

performed on silica gel (Sorbent Technologies, 40-63 μm particle diameter) slurry packed into glass columns.

2.2.2. Instrumentation

All UV-vis absorption spectra of compounds were recorded using a scanning spectrophotometer (UV-3101PC, Shimadzu, Columbia, MD) and quartz cuvettes (Starna Cells, Atascadero, CA) with path lengths of 1 cm (for solutions) or quartz slides (for thin films, Ted Pella, Inc., Redding, CA). Photoluminescence spectra were acquired using a HORIBA Spex Fluorolog-3 spectrofluorometer (model FL3-22TAU3, Jobin-Yvon, Edison, NJ), with entrance and exit slit widths maintained at 3 or 5 nm and using quartz cuvettes (Starna Cells, Atascadero, CA) with path lengths of 0.4 or 1 cm or quartz slides (for thin films, Ted Pella, Inc., Redding, CA). The same fluorometer was used for time-dependent kinetic photostability measurements with a 14 nm entrance slit width, as well as for the absolute photoluminescence quantum yield experiments, by connecting an integrating sphere to the fluorometer (HORIBA Scientific Quanta φ accessory, model FL3-22TAU3, HORIBA Scientific, Edison, NJ). Fluorescence lifetime experiments based on time-correlated single photon counting (TCSPC) were performed using a HORIBA FluoroMax plus fluorometer with a pulsed laser DeltaDiode (375 nm, pulse width 45 ps) and a PPD-850 detector with a transit time spread of 180 ps (Horiba Scientific, Edison, NJ). All CV experiments were performed at room temperature using an Autolab PGSTAT 302 potentiostat (Metrohm, Riverside, FL) with a three-electrode system, i.e., a platinum disk working electrode, a $Ag/AgNO_3$ nonaqueous reference electrode, and a Pt wire counterelectrode (CH Instruments, Austin, TX). The reference electrode was checked against the ferrocene/ferrocenium (Fc/Fc^+) redox couple as the standard. The potentials were quoted relative to the Fc/Fc^+ redox couple. The scan rate was maintained at 0.1 V/s within the potential range of -0.5 to +3.0 V and $TBAPF_6$ (in DCM or ACN,

0.1 M) was used as the supporting electrolyte. Thermal stability studies were performed using a Hi Res Modulated TGA 2950 thermogravimetric analyzer (TA Instruments, New Castle, DE) while single crystal XRD analysis was performed using a Bruker Kappa APEX-II DUO diffractometer (Bruker, Madison, WI). Malvern PANalytical Empyrean multipurpose diffractometer (Westborough, MA) with a copper anode was used for PXRD experiments. Grazing incidence X-ray scattering measurements were performed at beamline 8-ID-E of the Advanced Photon Source at Argonne National Laboratory using an X-ray wavelength of 1.6868 Å.[27] The area detector, a Pilatus 1M pixel array detector (Dectris, Switzerland) was positioned 204 mm from the sample. The sample was measured under vacuum and the scattering measured at two different detector heights for an incident angle of 0.18° and exposure time of 5s. Combining corresponding images eliminated rows of inactive pixels between the detector modules and verified that the samples were not damaged by the synchrotron beam. The acquired data (as two-dimensional images) were further treated and analyzed using GIXSGUI software package.[28]

An ultra-high vacuum thermal evaporation (VTE) system (Angstrom Engineering, Kitchener, ON) was used for OLED prototype fabrication. These OLED prototypes were fabricated in accordance with state-of-the-art protocols.[2,6,29] In summary, OLED prototypes were fabricated using following steps. First, ITO coated glass was ultrasonicated sequentially in detergent solution, DI water, acetone, and isopropanol followed by exposure to UV-ozone under ambient conditions for 20 minutes. Next, the OLED prototypes were fabricated by depositing organic layers on clean ITO coated glass substrates using the VTE system, maintained at a base pressure less than 1×10^{-6} Torr during all depositions. The deposition rates were 0.3 Å/s (Ca), 1 Å/s (NPB, 2,4,6-TPP, and TPBI), and 2 Å/s (Al). Layer thickness calibration was achieved using a Bruker Dektak XT surface profilometer (Bruker, Madison, NJ). Electroluminescence spectra and performance characteristics

of OLED prototypes were obtained using a PTI QuantaMaster4/2006SE spectrofluorometer (Photon Technology International, Edison, NJ), combined with an integrating sphere (Labsphere, North Sutton, NH). The total spectral flux was calibrated using a SCL-050 lamp standard (Labsphere, North Sutton, NJ). Current and voltage of OLED prototypes were controlled and measured using a Keithley 2601 sourcemeter (Tektronix, Inc., Beaverton, OR).

2.2.3. Computational Details

Density functional theory (DFT) computational calculations were performed using hybrid three-parameter non-local exchange functional developed by Becke with Lee–Yang–Parr correlation functional (B3LYP) to obtain energies and geometries of pyrenylpyridines.[30,31] The resolution of the identity (RI) approach was employed to speed up the computation through effective calculation of the two-electron integrals.[32] These calculations were performed using a triple-zeta valence plus polarization basis set (such as def2–TZVP).[33] Vibrational frequencies confirmed the identity of the optimized structures at local minima and the results were obtained by employing the Turbomole program suite (version 4.2).[34]

2.3. Synthesis and Characterization

Four pyrenylpyridine compounds displayed in Figure 2.1, i.e., 2,4-DPP, 2,6-DPP, 3,5-DPP, and 2,4,6-TPP, were synthesized using a one-step Suzuki coupling reaction between respective bromopyridines and 1-pyrenylboronic acid.[35] Synthesis of 2,4,6-TPP is described here as a representative protocol which is applied to the synthesis of all pyrenylpyridines with slight modifications. An Airfree flask was charged with 2,4,6-tribromopyridine (126 mg, 0.40 mmol), 1-pyrenylboronic acid (320 mg, 1.30 mmol), and tetrakis(triphenylphosphine)palladium(0) catalyst (60 mg, 0.05 mmol) inside a glove box. Following this, 1,4-dioxane (60 mL, degassed for 30 min) and aqueous K_2CO_3 (0.2 M, 15 mL, degassed for 30 min) were added to the flask while purging

with argon. The resulting mixture was stirred at 80 °C for 72 h under argon atmosphere, followed by chloroform extraction. The combined organic layer was washed several times with brine solution and DI water, and then dried over anhydrous magnesium sulfate. The solvent was removed under vacuum and the crude product was purified using column chromatography on silica gel (eluent hexanes: ethyl acetate ratio of 9:1 v/v) three times. After solvent evaporation, 2,4,6-TPP was obtained as a light-yellow powder (198 ±16 mg, yield 73 ±6%). In the case of the dipyrenylpyridines, molar ratios of dibromopyridine and 1-pyrenylboronic acid were maintained as 0.53:1.16 to obtain the products (163 ±11 mg, yield 74 ±14%). Characterization data for these compounds using ^{13}C NMR, ^{1}H NMR, (Bruker Avance 400) and ESI-MS (Agilent 6210 ESI-TOF) are presented in Appendix A.

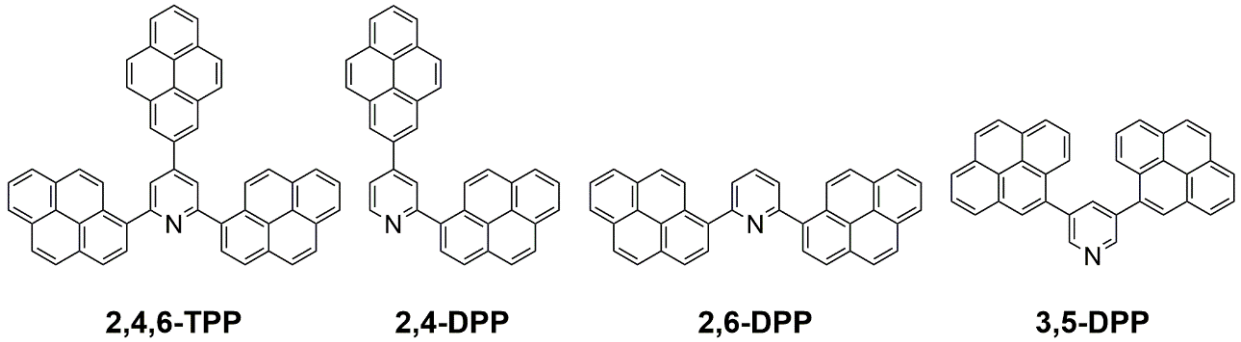

Figure 2.1. Chemical structures of pyrenylpyridines evaluated in this study.

2.4. Results and Discussion

2.4.1. Solid State Packing and Thin Film Morphology

Solid-state conformation often influences molecular aggregation and thin film morphology, thus influencing photo-physical properties of dyes, particularly in the condensed state. Therefore, molecular conformations of DPPs were elucidated with PXRD and single-crystal XRD techniques and presented in Figures A1-A3 in Appendix A. As revealed by PXRD, 2,4,6-TPP has the lowest degree of crystallinity among all four pyrenylpyridines studied (See Figure A2 in Appendix A).

The observed degree of crystallinity variations of pyrenylpyridines is correlated to the conformational changes of these compounds. For example, asymmetric and bulkier 2,4,6-TPP may reduce the packing efficiency in the solid-state than symmetric 2,6-DPP and 3,5-DPP and asymmetric, but less bulkier 2,4-DPP. Except 2,4,6-TPP, all pyrenylpyridines formed high quality single crystals for single-crystal XRD experiments. Crystal structures of three DPP compounds are available in crystallographic information file (CIF) formats, CCDC 1560016 (2,4-DPP), CCDC 1560018 (2,6-DPP), and CCDC 1560019 (3,5-DPP). Intermolecular distances and torsion angles of DPPs derived from single-crystal XRD experiments are listed in Table 2.1. According to single-crystal XRD data, all three DPP compounds adopt significantly twisted conformations in solid-state, with torsion angles between pyrenyl and pyridine moieties ranging from 42(12)° to 47(18)°, suggesting that the intramolecular twisting is significant and occurs more or less to same extents in all DPPs. Computed torsion angle values for DPPs were very close to the experimental values as showed in Table 2.1. The computed average torsion angle in 2,4,6-TPP was 49.58(7)°, confirming a twisted geometry similar to DPPs. However, the addition of the third pyrenyl moiety in 2,4,6-TPP had virtually no effect on the extent of intramolecular twisting of pyrene moieties, since the positioning of three pyrene units around the pyridine moiety in 2,4,6-TPP provided comparable steric effects to inter-molecular pyrene units as in DPPs. Despite this significant intramolecular twisting of pyrenyl units, DPPs managed to arrange in an apparent zig-zag order (Figure A3 in Appendix A), allowing these molecules to undergo significant π-π stacking. The intermolecular distances measured using C-C distances and N-N distances of neighboring DPP molecules in crystals ranged from 6.86 (±3) to 3.63 (±5) Å (for C-C) and 6.86 (±3) to 3.86 (±7) Å (for N-N), as a result of differences in solid-state packing induced by factors including the extent of intramolecular twisting, inter and intra molecular interactions, and molecular symmetry. Based

on intermolecular distances, solid-state packing efficiency of DPPs increases in the following order, 2,4-DPP < 2,6-DPP < 3,5-DPP.

Table 2.1. Summary of conformational and thermal properties of pyrenylpyridines.

Compound	T_m (°C)	T_{onset} (°C)	Intermolecular Distance (Å)	Torsion Angle (°) [c]
2,4-DPP	172	415	6.86(3)[a] 6.86(3)[b]	47.48(18)[d] 52.28(6)[e]
2,6-DPP	273	424	4.72(5) [a] 5.16(11)[b]	42.33(12)[d] 43.75(2)[e]
3,5-DPP	281	429	3.40(3)[a] 3.90(3)[b]	46.74(18)[d] 57.21(1)[e]
2,4,6-TPP	312	510	N/A	49.58(7)[e]

T_m: Melting point, T_{onset}: Decomposition onset temperature, Closest C-C distance [a] and N-N distance [b] between two neighboring pyrenylpyridine molecules in the single crystal, Angle between pyrenyl and pyridine units of pyrenylpyridines.[c] Experimental torsion angles obtained from single-crystal XRD.[d] Torsion angles obtained from DFT computations.[e] N/A: Not available.

Grazing-incidence wide-angle X-ray scattering (GIWAXS) is a very useful technique to study the crystallinity and orientation of organic thin films, which provides more realistic morphological information than PXRD and single crystal XRD techniques.[36] Accordingly, GIWAXS studies on vacuum-deposited thin films of 2,4,6-TPP revealed that there is no distinct diffraction features arising from isotropic/oriented condensed matter (Figure 2.2), as denoted by showing just an amorphous broad scattering at q = 1.51 Å. This diffraction pattern indicates that 2,4,6-TPP thin films were essentially amorphous, with no preferred packing of TPP molecules in thin films. Amorphous properties would be particularly suitable for using this material in thin film electroluminescent devices, since crystalline molecules may undesirably influence thermal stability and solid-state characteristics by the presence of nonlinear properties such as optical activity, conductivity, and photothermal reactivity.[37]

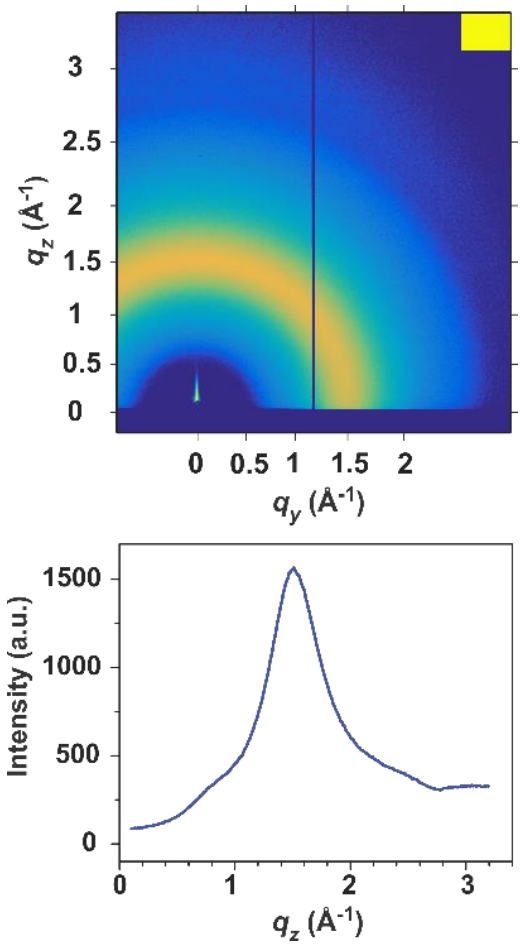

Figure 2.2. Two-dimensional GIWAXS image of a 2,4,6-TPP thin film on a quartz substrate (top) and vertical linecut of the GIWAXS data (bottom).

2.4.2. Computational Studies

Density function theory computational studies were performed to confirm structural and electrochemical characteristics of the pyrenylpyridines. Experimental details of computational calculations are provided in the section 2.2.3. All optimized geometries showed twisted structures with torsion angles between pyrene and pyridine units within each molecule comparable to the experimental torsion angles obtained using single-crystal XRD (Table 2.1). Also, details on frontier molecular orbitals were computationally obtained for all pyrenylpyridines. Noticeably, HOMO of 2,4,6-TPP was distributed over two of the pyrenyl components while LUMO was primarily located on the third, orthogonal pyrenyl moiety (Figure 2.3). The asymmetric 2,4-DPP

also shows a separation of HOMO and LUMO orbitals within the molecule (Figure A4 in Appendix A). In contrast, symmetric molecules, i.e., 2,6-DPP and 3,5-DPP, have HOMO and LUMO orbitals distributed over the same pyrenyl fragments (Figure A4 in Appendix A). Energy gaps obtained from computational studies were slightly higher (approximately 0.1-0.4 eV) than energy gap values obtained from low-energy onsets of the absorption bands of compounds in UV-vis absorption spectroscopy (Table A1 in Appendix A). This difference may due to fact that computational studies were done for the gas phase whereas experimental calculations were based on condensed phase of the compounds.

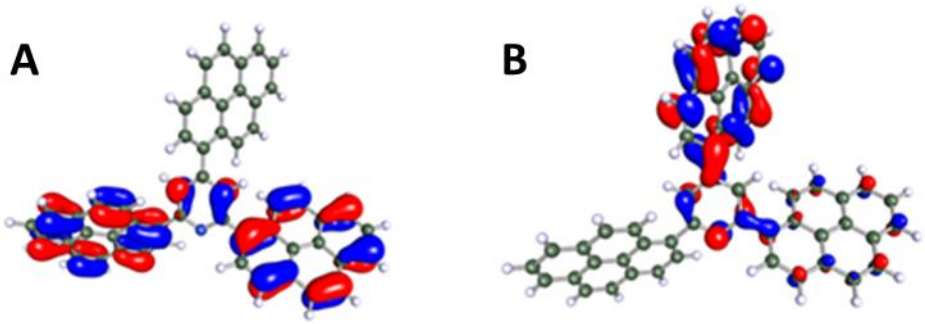

Figure 2.3. HOMO (A) and LUMO (B) of 2,4,6-TPP.

2.4.3. Photothermal Stability

Resistance to thermal degradation is crucial for the longevity of OLED devices.[38,39] In this regard, thermal stability of pyrenylpyridines was evaluated using thermogravimetric analysis (TGA). Typically, TGA experiments were conducted by heating samples of pyrenylpyridines (< 5 mg) in nitrogen atmosphere from 25 to 600 °C at a constant rate (10 °C/min). Since thermal decomposition of organic compounds typically accompanied with the formation of volatile compounds, the temperature in which an onset of weight loss (< 5%) is observed is reported as the onset decomposition temperature of the compound (T_{onset}), which is determined by using a step-tangent method.[40] The resultant TGA profiles of pyrenylpyridines are shown in Figure A5 in Appendix A, and T_{onset} values are listed in Table 2.1. Interestingly, all compounds exhibited high

thermal stabilities with T_{onset} values in the range of 415-510 °C. It is noted that the T_{onset} values of DPPs were distributed in a narrow range of 415-429 °C. The significantly high thermal stability of 2,4,6-TPP with T_{onset} value of 510 °C, which is 18 (±3)% higher than that of DPPs, is attributed to increased inter and intra molecular interactions of 2,4,6-TPP molecules, as a result of having an additional pyrenyl moiety. All pyrenylpyridines are high-melting solids, with melting points (T_m) ranging from 172-312 °C. The melting temperatures of the pyrenylpyridines increase in the following order, 2,4-DPP < 2,6-DPP < 3,5-DPP < 2,4,6-TPP, which parallels the trend in solid-state packing efficiency. For example, 2,4-DPP, which has the lowest packing efficiency (as discussed in the XRD section), shows the lowest T_m (172 °C). Thus, thermal stability of the pyrenylpyridines can be correlated to factors such as molecular symmetry, solid state conformation, and the extent of inter and intramolecular interactions.

Among various degradation processes of organic semiconductors which ultimately lead to device malfunction, photodegradation is one of the possible pathways.[41,42] Although the exact mechanisms involved in these light-induced reversible/irreversible oxidation processes may specific for a given molecule and not fully understood to date, it is suggested that radical dark states might be involved in the photobleaching mechanisms.[42,43] Photostability of pyrenylpyridines was evaluated using a previously reported procedure developed for organic dyes.[44,45] In a typical time dependent kinetic photostability experiment, the compound is intensively irradiated with a monochromatic light of the wavelength set at the absorption maximum for a sufficient time period, while recording the photoluminescence intensity fluctuations at the respective emission maximum of the compound. Typically, photolabile compounds show exponential decrease of emission intensity when intensively irradiated, as a result of photodegradation.[45] Therefore, it is assumed that this decay of emission intensity observed with increased irradiation time is proportional to the

extent of photobleaching. Accordingly, photostability of pyrenylpyridines were determined using Equation 2.1.

$$Photostability\ (\%) = \left(\frac{I}{I_0}\right) \times 100\ \%\ , \qquad (2.1)$$

where I is the emission intensity after the intensive irradiation and I_0 is the observed emission intensity before the intensive irradiation. The resultant time-dependent photoluminescence intensity fluctuation curves of all pyrenylpyridines are presented in Figure A6 in Appendix A. It is noted that all pyrenylpyridines maintained stable photoluminescence, i.e., there is no measurable photobleaching upon intense irradiation under the given experimental conditions. These photobleaching curves of pyrenylpyridines are similar to that of other photostable compounds evaluated by time dependent kinetic photostability experiments reported in literature.[46] The enhanced photostability exhibited by pyrenylpyridines is attributed to pyrenyl moieties which are highly resistant to photodegradation under ambient conditions.

2.4.4. Spectral Properties in Solution and Solid States

UV-vis absorption spectra of pyrenylpyridines were recorded in chloroform solution (5 μM) and in thin solid films. Thin solid films of pyrenylpyridines were formed on quartz slides by electro-spray deposition (1 mM in DCM, flow rate 100 μL/min, applied voltage 2.8 V, and applied current 3 A). The absorption spectra obtained for solution and solid films of pyrenylpyridines are presented in Figure 2.4 and values of absorption maxima and full widths at half maxima (FWHM) are summarized in Table 2.2.

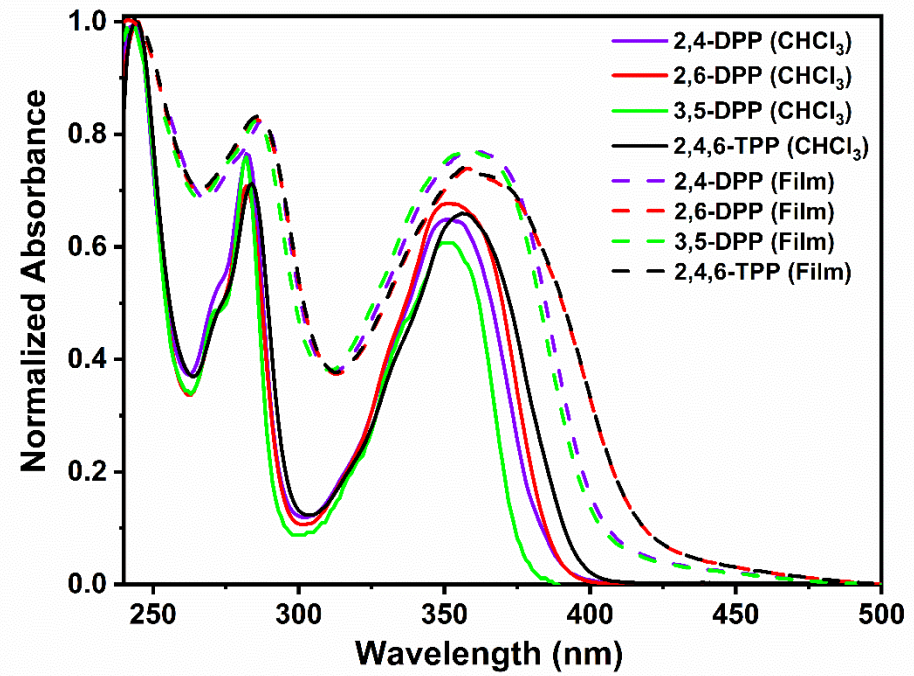

Figure 2.4. Normalized absorption spectra of pyrenylpyridines in chloroform solution and as thin films on quartz.

Accordingly, all pyrenylpyridines showed three broad absorption peaks in both solution and solid states, with absorption peak maxima (A_{max}) at 244 ±1 (A_{max3}), 282 ±2 (A_{max2}), and 353 ±3 (A_{max1}), respectively. Solution and solid-state absorption spectra largely resembled those of pyrene, but were lacking the fine vibronic features characteristic for the pyrene absorption spectrum.[21,47] Considering the molecular design of pyrenylpyridines, in which, pyrenyl groups are relatively good electron acceptors and pyridine group is an electron donor, it is likely to occur intramolecular charge transfer absorption. Accordingly, in solid-state absorption spectra, absorption peaks of pyrenylpyridines were significantly broadened with average FWHM values of 77 (A_{max1}), 43 (A_{max2}), and 58 (A_{max3}) nm in solid films than in solution state (48 for A_{max1}, 24 for A_{max2}, and 19 for A_{max3} nm, respectively) and red-shifted (≤ 7 nm).

Table 2.2. Absorption data for pyrenylpyridines.

Compound	Absorption Maxima (nm)		FWHM (nm)	
	Sol[x]	Film	Sol[x]	Film
2,4-DPP	244	241	19	56
	282	286	25	59
	353	358	46	75
2,6-DPP	245	240	20	64
	282	287	25	37
	352	355	48	74
3,5-DPP	244	243	20	61
	282	286	21	41
	351	358	41	83
2,4,6-TPP	244	244	19	58
	284	286	27	37
	356	361	51	69

[x] In chloroform solution (5 μM)

Photoluminescence spectra of all pyrenylpyridines were recorded in chloroform solutions (1 μM) and in thin solid films prepared by electro-spray deposition as described in previous section. Photoluminescence spectra of pyrenylpyridines are presented in Figure 2.5. Also, emission maxima and FWHM values are summarized in Table 2.3. Emission spectra of all pyrenylpyridines, in both solution and solid states, are largely resembled to pyrene excimer emission with a single broad peak that has no fine vibronic structures.[47] Emission maxima of pyrenylpyridines were found in the range of 392-440 nm in chloroform solution and 463-494 nm for solid films (Table 2.3). Photoluminescence peaks of pyrenylpyridines were broadened (as denoted by increase of FWHM values approximately by 20-30 nm) and red-shifted (as denoted by λ_{max} shifts of approximately 50-90 nm) in solid-state than in solution (Table 2.3), presumably due to dye aggregation.[12] However, dye aggregation was not as extensive as in many cases of pyrene derivatives reported in the literature, in which, solid-state emission was completely shifted to green region of the EMS, with substantial aggregation-induced quenching .[7]

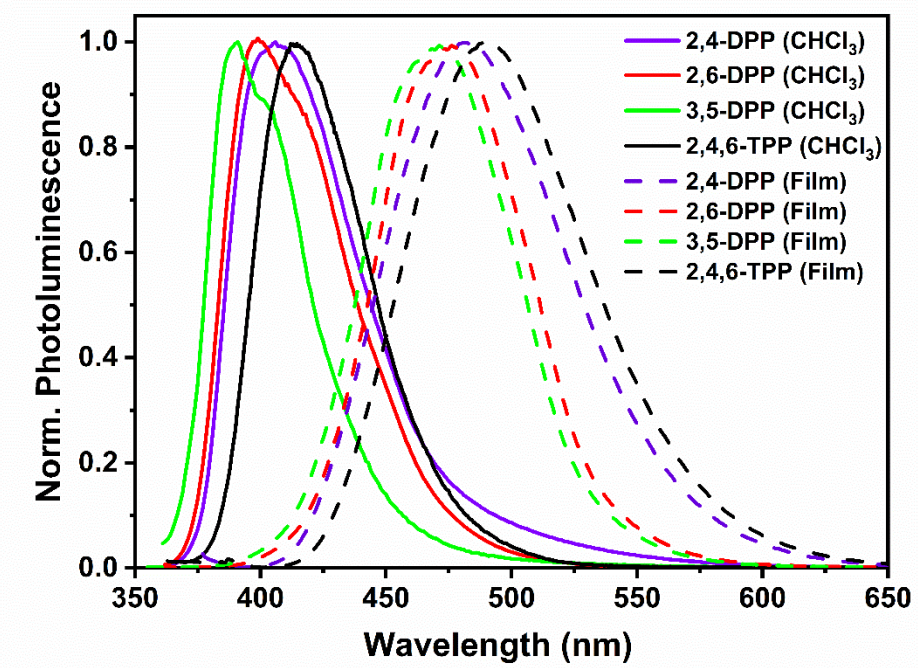

Figure 2.5. Normalized emission spectra of pyrenylpyridines in chloroform solutions and as thin films on quartz.

Photoluminescence of pyrenylpyridines was confined approximately to the violet-blue region of the EMS in solution state and greenish-blue region of the EMS in the solid-state. Accordingly, the color of these compounds has been assigned in accordance to CIE coordinates (Table 2.3) and found in the range of (0.162 ±0.003, 0.04 ±0.016) for solution state and (0.149 ±0.018, 0.235 ±0.09) for solid-state.

Table 2.3. Summary of emission properties of pyrenylpyridines.

Compound	Emission Maxima (nm)		FWHM (nm)		Stokes Shift (nm)		CIE Coordinates (x,y)	
	Sol[x]	Film	Sol[x]	Film	Sol[x]	Film	Sol[x]	Film
2,4-DPP	406	463	59	82	53	107	0.162, 0.062	0.159, 0.279
2,6- DPP	400	468	55	77	48	116	0.159, 0.027	0.135, 0.144
3,5-DPP	392	476	44	69	41	125	0.165, 0.037	0.132, 0.175
2,4,6-TPP	412	494	52	85	56	141	0.160, 0.029	0.170, 0.343

[x] In chloroform (1 µM)

In order to investigate possible solvatochromism, photoluminescence spectra of pyrenylpyridines were recorded in hexane, methanol, and DMSO solvents which have polarity

indices in the range of 0-7.2 (Table A2 of Appendix A). The emission spectra of all four compounds red shifted with increasing solvent polarity from 394 ±2 nm (hexane) to 435 ±10 (DMSO) nm, indicating charge transfer character in photoluminescence. Absorption, excitation, and emission spectra of 2,4,6-TPP in chloroform solution (5 μM) are presented in Figure 2.6, indicating absorbance and excitation spectra of 2,4,6-TPP almost coincide, and the absorption and emission spectra obey 'the mirror image rule', suggesting no major geometrical changes occurring in the excited state.[21]

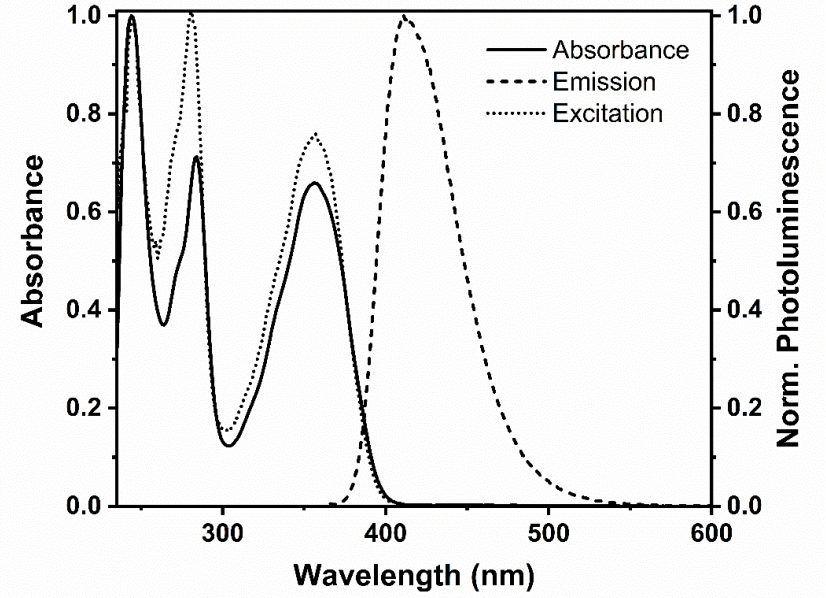

Figure 2.6. Normalized absorbance, excitation, and emission spectra of 2,4,6-TPP in chloroform solution.

2.4.5. PLQY and Lifetimes

High photoluminescence efficiency is an important requirement for OLED emitters, but is not the only criterion to determine the electroluminescence efficiency of OLED emitters. This is because electroluminescence mechanism of an emitter may influence by number of factors that are typically not interfere with photoluminescence mechanisms, including OLED architecture and electrical properties of the OLED.[48,49] Photoluminescence efficiency of an OLED emitter is determined in terms of PLQY, which is defined as the ratio of emitted photons to absorbed

photons.[21] Absolute quantum yields of pyrenylpyridines in chloroform solutions and in thin films were determined using an integrating sphere attached to a spectrofluorometer.[50] Table 2.4 summarized the PLQY values recorded for pyrenylpyridines. Accordingly, 2,4,6-TPP displayed the highest quantum yield in solution (89%) as well as in thin film (64%), likely due to the presence of an additional pyrenyl luminophore as well as much reduced dye aggregation than DPPs. Interestingly, DPPs showed PLQY values in the range of 74-79% in solution and 47-55% in solid films. Accordingly, despite the dye aggregation in the solid-state, substantial PLQY values were observed for all pyrenylpyridines.

Table 2.4. Quantum yields and fluorescence lifetimes of pyrenylpyridines.

Compound	PLQY (%)		Emission lifetime (ns)
	Sol[x]	Film	
2,4-DPP	79	47	7.66
2,6-DPP	74	51	6.28
3,5-DPP	76	55	6.12
2,4,6-TPP	89	64	4.25

[x] In chloroform solution (1μM)

Fluorescence lifetime measurements were performed for each of the studied pyrenylpyridine compounds. Table 2.4 and Figure A7 in Appendix A provide lifetime data summary and decay curves for these compounds in solid-films. Fluorescence decay curves of all four compounds showed single-exponential decays indicating a single pathway for energy transitions, and origination of photoluminescence from the singlet excited state in all cases.[21] The lifetimes of pyrenylpyridines were distributed in the range of 7.66-4.25 ns. Interestingly, 2,4,6-DPP has the shortest lifetime (4.25 ns), thus has a less tendency for non-radiative side reactions in the excited state, as denoted by the observed highest PLQY for investigated pyrenylpyridines.

2.4.6. Electronic Properties

Estimating HOMO and LUMO energies and HOMO-LUMO energy gaps (E_g) of OLED emitters is crucial for designing OLED devices. The E_g value of a material is defined as the separation between maximum energy of the valence band and minimum energy of the conduction band.[51] Typically, semiconducting materials display energy gaps in the range of 0-4 eV.[51] The E_g values of all pyrenylpyridines were experimentally determined using UV-vis absorption spectra, in particular, λ_{edge} values assuming the minimum energy required to promote an electron from the ground state to the first excited state is equal to E_g (Equation 2.3).[44] Accordingly, experimental E_g values obtained by CV were in the range of 3.10 to 3.28 eV as shown in Table 2.5. Also, the HOMO values of pyrenylpyridines were experimentally obtained using CV by employing Equation 2.2.[52,53] All pyrenylpyridines displayed quasi-reversible cyclic voltammograms with measurable oxidation peaks under the stated conditions (Figure A8 in Appendix A). Quasi-reversible behavior is often displayed by redox couples with one state (oxidation or reduction) is not stable in the time scale of the CV experiment.[54] Accordingly, the LUMO values were calculated using Equation 2.3 since E_g values were obtained from UV-vis spectroscopy.[44,45] In Equation 2.2, E_{ox} is the onset potential value of the oxidation peak obtained from the cyclic voltammogram of a compound. The energy values experimentally determined for frontier orbitals of pyrenylpyridines were in the respective ranges of -5.67 to -5.76 eV, and -2.42 to -2.60 eV (Table 2.5).

$$HOMO\ (eV) = -1e\ [E_{ox.} + 4.71]eV \tag{2.2}$$

$$E_g(eV) = [HOMO - LUMO] = \frac{hc}{\lambda_{edge}} = \frac{1240}{\lambda_{edge}}\ eV \tag{2.3}$$

Table 2.5. Electronic properties of pyrenylpyridines

Compound	E_g (eV)	HOMO (eV)	LUMO (eV)
2,4-DPP	3.16	-5.75	-2.60
2,6-DPP	3.16	-5.76	-2.60
3,5-DPP	3.28	-5.70	-2.42
2,4,6-TPP	3.12	-5.67	-2.55

2.4.7. Characterization of OLED Prototype Fabricated with 2,4,6-DPP as the EML

OLED emitters in EML can be embedded in an energetically matching host matrix (doped) or use as it is without such matrices (non-doped/self-host).[3,4] Doped EMLs have distinct advantages such as reduction of aggregation induced quenching and formation of favorable energy transfers between the host and the emitter, which typically improve the device performance.[3,4] However, the disadvantages associated with doping include phase separation induced degradation, limited availability of energetically matching host materials for blue emitters, and the complexity in device fabrication.[3,4] Considering pros and cons of doped EMLs, a non-doped OLED prototype was fabricated for preliminary studies presented in this chapter to reduce the complexity of device fabrication and to understand electroluminescent properties of the pure emitter. Since 2,4,6-TPP displayed the most promising photo-physical characteristics among the pyrenylpyridines investigated (i.e., highest PLQY, highest thermal stability, and the lowest degree of crystallinity), an OLED prototype was fabricated using 2,4,6-TPP as the non-doped emissive layer. These prototypes were fabricated using VTE method, in accordance with the state-of-the-art.[29] The configuration of OLED prototypes were, ITO (140 nm)/ NDB (35 nm)/ 2,4,6-TPP (35 nm)/ TPBI (30 nm)/ Ca (12 nm)/Al (100 nm) as schematically showed in Figure 2.7 (A). These OLED prototypes contained NPB and TPBI as hole transport and electron transport layers, and 2,4,6-TPP as the non-doped emissive layer whereas ITO was employed as the anode and a Ca as the cathode. The device performance metrics were obtained in accordance with previously reported

protocols.[6,55] This device reached maximum EQE of 6.0 (±1.2) % at 5 V with luminance of 36.2 (±4.7) cdm^{-2}, power efficiency of 8.0 (±1.9) lmW^{-1}, and current efficiency of 6.3 (±1.5) cdA^{-1}. Upon gradual increase of voltage, the device showed much brighter electroluminescence, and luminance reached to 100 cdm^{-2} at 7.5 V. At 100 cdm^{-2} luminance, an EQE of 1.2 (±0.1) %, power efficiency of 1.1 (±0.1) lmW^{-1}, and current efficiency of 1.4 (±0.1) cdA^{-1} were obtained. The OLED prototype performance is graphically presented in Figure 2.7 (B).

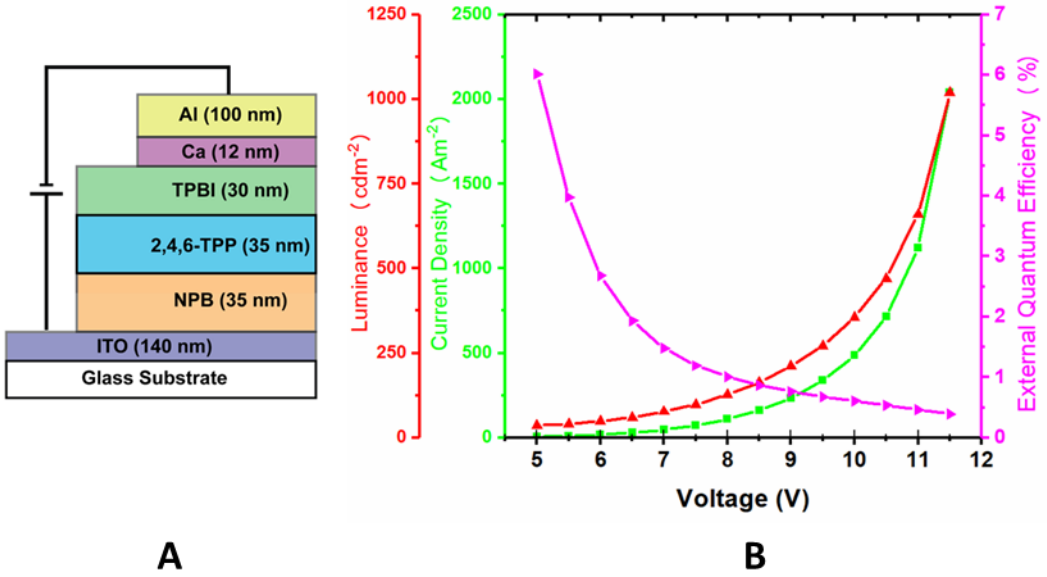

Figure 2.7. A simplified schematic of the device architecture (A) and OLED performance plots (B) for the OLED prototype with 2,4,6-TPP as the emissive layer. (Please note: OLED device is not drawn proportionally).

A sky-blue electroluminescence is observed from this OLED prototype with a turn-on voltage of 4 V as showed in Figure 2.8. The CIE coordinates of the electroluminescence observed from this OLED was (0.154, 0.297), which is analogous to observed photoluminescence from the thin film of 2,4,6-TPP, with peak maximum at 490 nm. Therefore, electroluminescence mechanisms of the 2,4,6-DPP emissive layer are assumed to be based on conventional fluorescence (Figure A9 in Appendix A).[4] This sky-blue OLED emitter can be successfully applied in novel pixel designs that contain a light blue component.[56,57]

Figure 2.8. A photograph showing electroluminescence of the OLED prototype with 2,4,6-DPP as the emissive layer.

2.5. Conclusions

A series of structurally related pyrenylpyridine compounds was successfully synthesized and spectral, physical, and electrical properties of these compounds were thoroughly investigated. Although these pyrenylpyridines are structurally related, aforementioned properties were found to be quite diverse, particularly in the solid-state. These differences stem from factors such as molecular symmetry, extent of inter/intramolecular interactions, and conformational changes of pyrenylpyridines. Pyrenylpyridines exhibited high photothermal stability, PLQY, and electronic properties that are suitable for optoelectronic applications. Among these pyrenylpyridines, 2,4,6-TPP was found to display the highest photothermal stability and the lowest crystallinity in thin films, as well as the highest PLQY. Therefore. prototype OLED device was fabricated with 2,4,6-TPP as the non-doped emissive layer, which showed bright sky-blue electroluminescence, and reached luminance value of 100 cd m^{-2} at 7.5 V, with external quantum efficiency of 1.2 (±0.1) %, power efficiency of 1.1 (±0.1) lmW^{-1} and current efficiency of 1.4 (±0.1) cdA^{-1}. Evaluation of structure-property relationships of the pyrenylpyridines as model compounds related to pyrene aided in understanding the important role of morphology induced inter- and intra- molecular interactions, that are known to tremendously affect the spectral and physical characteristics of

structurally related molecules. Future directions for this research involve fabrication and characterization of OLED prototypes for DPPs and fabrication of OLED prototypes with a doped emissive layer by embedding pyrenylpyridines in a suitable host matrix to further improve device performance.

2.6. References

1. Gupta, A. S.: *Organic Light Emitting Diodes (OLEDs): Technologies and Global Markets*; BCC Research, Massachusetts, USA, **2015**; pp. 7-14, 90-120.

2. Martens, R.: *The OLED Handbook: A Guide to OLED Technology, Industry & Market*; LULU Press: North Carolina, USA, **2014**; pp. 11-36.

3. Zhu, M.; Yang, C.: Blue fluorescent emitters: Design tactics and applications in organic light-emitting diodes. *Chemical Society Reviews* **2013**, *42*, 4963-4976.

4. Yang, X.; Xu, X.; Zhou, G.: Recent advances of the emitters for high performance deep-blue organic light-emitting diodes. *Journal of Material Chemistry C* **2015**, *3*, 913-944.

5. Salunke, J. K.; Sonar, P.; Wong, F. L.; Roy, V. A.; Lee, C. S.; Wadgaonkar, P. P.: Pyrene based conjugated materials: synthesis, characterization and electroluminescent properties, *Physical Chemistry Chemical Physics* **2014**, *16*, 23320-23328.

6. Su, W. Printed organic light emission and display. In *Printed Electronics*; Editors Cui, Z.; John Wiley & Sons; New York, USA, **2016**, pp. 251-260.

7. Hu, J.-Y.; Yamato, T.: Synthesis and photophysical properties of pyrene-based multiply conjugated shaped light-emitting architectures: Toward efficient organic-light-emitting diodes. In *Organic Light Emitting Diode - Material, Process and Devices*; Editors Ko, S. H.; InTech: Rijeka, Croatia, **2011**; pp 22-54.

8. Amarnath, C. A.; Kim, H. K.; Yi, D. K.; Lee, S.; Do, Y. R.; Paik, U.: Novel electroluminescent polymer derived from pyrene-functionalized polyaniline. *Bull. Korean Chem. Soc*., **2011**, *32*(5), 1495-1499.

9. Sonar, P.; Soh, M. S.; Cheng, Y. H.; Henssler, J. T.; Sellinger, A.: 1,3,6,8-tetrasubstituted pyrenes: solution-processable materials for application in organic electronics. *Organic letters* **2010**, *12*, 3292-3295.

10. Okinara, K.; Yamada, N.; Igawa, S.; Kamatani, J.; Yashima, M. Organic light-emitting device. WIPO Patent WO2007072741 A1, June 28, 2007.

11. Yang, C.-H.; Guo, T.-F.; Sun, I.-W.: Highly efficient greenish blue-emitting organic diodes based on pyrene derivatives. *Journal of Luminescence* **2007**, *124*, 93-98.

12. Chercka, D.; Yoo, S.-J.; Baumgarten, M.; Kim, J.-J.; Mullen, K.: Pyrene based materials for exceptionally deep blue OLEDs. *Journal of Materials Chemistry C* **2014**, *2*, 9083-9086.

13. Pu, Y.- J.; Yoshizaki, M.; Akiniwa, T.; Nakayama, K.-I.; Kido, J.: Dipyrenylpyridines for electron-transporting materials in organic light emitting devices and their structural effect on electron injection from Li/Al cathode. *Organic Electronics* **2009**, *10*, 877-882.

14. Jeon, W. S.; Hyoung-Yun, O.; Park, J. S.; Kwon, J. H.: High Mobility Electron Transport Material with Pyrene Moiety for Organic Light-Emitting Diodes (OLEDs). *Molecular Crystals and Liquid Crystals* **2011**, *550* (1), 311-319.

15. Zhou, Y.; Kim, J. W.; Kim, M. J.; Son, W.-J.; Han, S. J.; Kim, H. N.; Han, S.; Kim, Y.; Lee, C.; Kim, S. J.; Kim, D. H.; Kim, J.-J.; Yoon, J.: Novel bi-nuclear boron complex with pyrene ligand: red-light emitting as well as electron transporting material in organic light-emitting diodes. *Organic Letters* **2010**, *12* (6), 1272-1275.

16. Oh, H.-Y.; Lee, C.; Lee, S.: Efficient blue organic light-emitting diodes using newly-developed pyrene-based electron transport materials. *Organic Electronics* **2009**, *10*, 163-169.

17. Wu, K.-C.; Ku, P.-J.; Lin, C.-S.; Shih, H.-T.; Wu, F.-I.; Huang, M.-J.; Lin, J.-J.; Chen, I.-C.; Cheng, C.-H.: The photophysical properties of dipyrenylbenzenes and their application as exceedingly efficient blue emitters for electroluminescent devices. *Advanced Functional Materials* **2008**, *18*, 67-75.

18. Keawin, T.; Prachumrak, N.; Namuangruk, S.; Pansay, S.; Kungwan, N.; Maensiri, S.; Jungsuttiwong, S.; Sudyoadsuk, T.; Promarak, V.: Efficient bifunctional materials based on pyrene- and triphenylamine-functionalized dendrimers for electroluminescent devices. *RSC Advances* **2015**, *5*, 73481-73489.

19. Zophel, L.; Beckmann, D.; Enkelmann, V.; Chercka, D.; Rieger, R.; Mullen, K.: Asymmetric pyrene derivatives for organic field-effect transistors. *Chemical Communications* **2011**, *47*, 6960-6962.

20. Chan, K. L.; Lim, J. P. F.; Yang, X.; Dodabalapur, A.; Jabbour, G. E.; Sellinger, A.: High efficiency pyrene-based blue light emitting diodes: aggregation suppression using a calixarene 3D-scaffold. *Chemical Communications* **2012**, *48*, 5106-5108.

21. Lakovicz, J. R.: *Principles of Fluorescence Spectroscopy*; Springer: New York, USA, **2006**; pp 9-12, 103-124.

22. Zhao, Z.; Chen, S.; Lam, J. W. Y.; Wang, Z.; Lu, P.; Mahtab, F.; Sung, H. H. Y.; Williams, I. D.; Ma, Y.; Kwok, H. S.; Tang, B. Z.: Pyrene-substituted ethenes: aggregation-enhanced

excimer emission and highly efficient electroluminescence. *Journal of Materials Chemistry* **2011**, *21*, 7210-7216.

23. Zhang, Y.; He, B.; Liu, J.; Hu, S.; Pan, L.; Zhao, Z.; Tang, B. Z.: Aggregation-induced emission and the working mechanism of 1-benzoyl and 1-benzyl pyrene derivatives. *Physical Chemistry Chemical Physics* **2018**, *20*, 9922-9929.

24. Lo, M. Y.; Zhen, C.; Lauters, M.; Jabbour, G. E.; Sellinger, A.: Organic-inorganic hybrids based on pyrene functionalized octavinylsilsesquioxane cores for application in OLEDs. *Journal of the American Chemical Society* **2007**, *129*, 5808-5809.

25. Lee, E.-Y.; Hwang, S.-H.; Kim, Y.-K.; Jung, H.-J.; Park, J.-H.; Lim, J.-O.; Han, S.-H.; Jeong, E.-J.; Kim, S.-Y.; Lee, J.-H.: Condensed cyclic compound and organic light-emitting device comprising the same. US 20140183463A1. July 3, 2014.

26. Cho, S.-J.; Lee, C.-M. Condensed cyclic compound and organic light-emitting device including the same. US 20150263290A1. September 17, 2015.

27. Jiang, Z.; Li, X.; Strzalka, J.; Sprung, M.; Sun, T.; Sandy, A. R.; Narayanan, S.; Lee, D. R.; Wang, J.: The dedicated high-resolution grazing-incidence X-ray scattering beamline 8-ID-E at the Advanced Photon Source. *Journal of Synchrotron Radiation* **2012**, *19*, 627-636.

28. Jiang, Z.: GIXSGUI: a MATLAB toolbox for grazing-incidence X-ray scattering data visualization and reduction, and indexing of buried three-dimensional periodic nanostructured films. *Journal of Applied Crystallography* **2015**, *48*, 917-926.

29. Koden, M.: *OLED Displays and Lighting*; John Wiley & Sons, New York, USA, **2017**; pp 12-24, 103-116.

30. Burke, K.; Perdew, J. P.; Wang, Y. In *Electronic Density Functional Theory: Recent Progress and New Directions*; Editors Dobson, J. F.; Vignale, G.; Das, M. P.; Plenum Publishers; New York, USA, **1998**; pp 81-113.

31. Becke, A. D. J.: Density-functional thermochemistry. III. The role of exact exchange. *Chemical Physics* **1993**, *98*, 5648-5652.

32. C. Hättig.: Geometry optimizations with the coupled-cluster model CC2 using the resolution-of-the-identity approximation. *The Journal of Chemical Physics* **2003**, *118*, 7751-7761.

33. Weigend, F.; Ahlrichs, R.: Balanced basis sets of split valence, triple zeta valence and quadruple zeta valence quality for H to Rn: Design and assessment of accuracy. *Physical Chemistry Chemical Physics* **2005**, *7* (18), 3297-3305.

34. Ahlrichs, R.; Bär, M.; Häser, M.; Horn, H.; Kölmel, C.: Electronic structure calculations on workstation computers: the program system turbomole. *Chemical Physics Letters* **1989**, *162*, 165-169.

35. Miyaura, N.; Suzuki, A.: Palladium-catalyzed cross-coupling reactions of organoboron compounds. *Chemical Reviews* **1995,** *7*, 2457-2483.

36. Müller-Buschbaum, P.: The active layer morphology of organic solar cells probed with grazing incidence scattering techniques. *Advanced Materials* **2014**, *26*, 7692-7709.

37. Moorthi, J. N.; Venkatakrishnan, P.; Natarajan, P.; Huang, D.-F.; Chow, T. J.: De novo design for functional amorphous materials: synthesis and thermal and light-emitting properties of twisted anthracene-functionalized bimesitylenes. *Journal of the American Chemical Society* **2008**, *130*, 17320-17333.

38. Kwak, K.; Cho, K.; Kim, S.: Analysis of thermal degradation of organic light-emitting diodes with infrared imaging and impedance spectroscopy. *Optics Express* **2013**, *21*, 29558-29566.

39. Kaya, I.; Aydin, A.: Synthesis and characterization of the polyaminophenol derivatives containing thiophene in side chain: Thermal degradation, electrical conductivity, optical-electrochemical, and fluorescent properties. *Journal of Applied Polymer Science* **2011**, *121*, 3028-3040.

40. Eshetu, G. G.; Jeong, S.; Pandard, P.; Lecocq, A.; Marlair, G.; Passerini, S.: Comprehensive insights into the thermal stability, biodegradability, and combustion chemistry of pyrrolidinium-based ionic liquids. *ChemSusChem* **2017**, *10*, 3146-3159.

41. Vogelsang, J.; Kasper, R.; Steinhauer, C.; Person, B.; Heilemann, M.; Sauer, M.; Tinnefeld, P. A Reducing and Oxidizing System Minimizes Photobleaching and Blinking of Fluorescent Dyes. *Angewandte Chemie International Edition* **2008**, *47*, 5465-5469.

42. Hoogenboom, J. P.; van Dijk, E. M.; Hernando, J.; van Hulst, N. F.; Garcia-Parajo, M. F.: Power-law-distributed dark states are the main pathway for photobleaching of single organic molecules. *Physical Review Letters* **2005**, *95*, 097401.

43. Neumuller, K. G.; Elsayad, K.; Reisecker, J. M.; Waxham, M. N.; Heinze, K. G. Photounbinding of calmodulin from a family of CaM binding peptides. *PLoS ONE* **2010**, 5, e14050.

44. Siraj, N.; Hassan, F.; Das, S.; Kiruri, L.; Steege Gall, K. E.; Baker, G. A.; Warner, I. M.: Carbazole-derived group of uniform materials based on organic salts: solid state fluorescent analogues of ionic liquids for potential applications in organic-based blue light-emitting diodes. *Journal of Physical Chemistry C* **2014**, *118*, 2312-2320.

45. De Silva, T. P. D.; Sahasrabudhe, G.; Yang, B.; Wang, C.-H.; Chhotaray, P. K.; Nesterov, E. E.; Warner, I. M.: Influence of anion variations on morphological, spectral, and physical properties of the propidium luminophore. *Journal of Physical Chemistry A* **2018**, *120*, 5155-5163.

46. Kolic, P. E.; Siraj, N.; Hamdan, S.; Regmi, B. P.; Warner, I. M. Synthesis and characterization of porphyrin-based GUMBOS and nanoGUMBOS as improved photosensitizers. *Journal of Physical Chemistry C* **2016**, *120*, 5155-5163.

47. Valeur, B.: *Molecular Fluorescence: Principles and Applications*; Wiley-VCH Verlag GmbH, Weinheim, Germany, **2001**; pp. 92-98.

48. Song, H.-Z.; Bao, X.-M.; Li, N.-S.; Zhang, J.-Y.: Relation between electroluminescence and photoluminescence of Si^+-implanted SiO_2. *Journal of Applied Physics* **1997**, *82*, 4028.

49. Anderson, M. R.; Yu, G.; Heeger, A. J.: Photoluminescence and electroluminescence of films from soluble PPV-polymers. *Synthetic Metals* **1997**, *85*, 1275-1276.

50. Wurth, C.; Grabolle, M.; Pauli, J.; Spieles, M.; Resch-Genger, U.: Relative and absolute determination of fluorescence quantum yields of transparent samples. *Nature Protocols* **2013**, *8*, 1535-1550.

51. Strehlow, W. H.; Cook, E. L.: Compilation of energy band gaps in elemental and binary compound semiconductors and insulators. *The Journal of Physical Chemistry Reference Data* **1973**, *2*, 163-199.

52. Bard, A. J.; Faulkner, L. R.: *Electrochemical Methods Fundamentals and Applications*; John Wiley & Sons, New York, USA, **2001**; pp 156-261.

53. Zhou, Y.; He, Q.; Yang, Y.; Zhong, H.; He, C.; Sang, G.; Liu, W.; Yang, C.; Bai, F.; Li, Y.: Binaphthyl-containing green- and red-emitting molecules for solution-processable organic light-emitting diodes. *Advanced Functional Materials* **2008**, *18*, 3299-3306.

54. Cardona, C. M.; Li, W.; Kaifer, A. E.; Stockdale, D.; Bazan, G. C.: Electrochemical considerations for determining absolute frontier orbital energy levels of conjugated polymers for solar Cell applications. *Advanced Materials* **2011**, *23*, 2367-2371.

55. Forrest, S. R.; Bradley, D. D. C.; Thompson, M. E.: Measuring the efficiency of organic light-emitting devices. *Advanced Materials* **2003**, *15*, 1043-1048.

56. Hack, M.; Brown, J. J.; Weaver, M. S.; D' Andrade, B. OLED Display Architecture. U.S. Patent 9385167, July 5, 2016.

57. https.//www.oled-info.com/udc-show-new-light-blue-emitter-that-can-be-used-white-oleds-or-four-sub-pixel-displays (accessed February 4, 2019).

CHAPTER III. PYRENE-BENZIMIDAZOLE DERIVATIVES AS NOVEL BLUE EMITTERS FOR OLEDS

3.1. Introduction

OLEDs were developed over the course of 30 years, from a laboratory concept in the pioneering work of Ching W. Tang and Steven A. Van Slyke, to a leading technology in the consumer electronics market.[1,2] Compared to the competing LCD display, OLED display offers advantages such as energy conservation by self-emission, device flexibility for curved electronic displays with broad viewing angles, outstanding picture quality due to the absence of back-lighting, and thin electronic screens with a significantly low weight.[2,3] However, the much shorter lifespan of OLED panels compared to that of LCDs is still a formidable challenge, one caused by inferior performance of blue emitters.[1,2] Blue emitters often suffer from deficiencies such as inefficient charge injection and mobility, lower photo-thermal/chemical stability, and an insufficient spectral purity with respect to red and green emitters in full-color RGB electronic displays.[4-6] The intrinsically wide HOMO-LUMO band gaps of blue emitters make charge injection from the electrodes/supporting organic layers to the emissive layer much harder. Also, blue emitters are susceptible to rapid degradation as a result of side-reactions from the high energy excited state.[4] Therefore, it is important to design novel blue emitters addressing these inadequacies.[4-7] several strategies were employed to address the aforementioned inadequacies of blue emitters. These efforts included optimization of molecular designs, OLED architectures, and exciton harvesting mechanisms.[4,5] Multifunctional molecular designs are recognized as one of the most promising solutions, therein, hole and/or electron transport moieties are incorporated into the blue emitters to facilitate proper flux of charge carriers to the EML.[4] Multifunctional emitters are classified as *p*-type (hole transporters)[8-11], *n*-type (electron transporters),[12-14] and bipolar (electron and hole transporters).[15-17] The use of multifunctional emissive materials could

effectively reduce the number of supporting organic semiconducting layers in OLEDs, thus lowering the cost and the complexity of OLED devices.[4]

This chapter reports the design, synthesis, and characterization of three novel, structurally related, *n*-type multifunctional small organic molecules. These compounds are hybrids of pyrene and benzimidazole derivatives, namely, 2-(1,2-diphenyl)-1*H*-benzimidazole-7-*tert*-butylpyrene (compound A), 1,3-di(1,2-diphenyl)-1*H*-benzimidazole-7-*tert*-butylpyrene (compound B), and 1,3,6,8-tetra(1,2-diphenyl)-1*H*-benzimidazolepyrene (compound C). Pyrene moieties in these compounds serve as the blue luminophores. Pyrene was selected as the luminophore due to a number of favorable characteristics, in particular, its resistance to all sorts of degradations stems from chemically stable PAH structure, substantial quantum efficiency, favorable charge carrier properties, ease of modification, and low cost.[7,18] For these reasons, a vast number of pyrene derivatives have been studied as emissive materials, charge injection materials, and charge transport materials in OLEDs.[7,18] However, pyrene derived pure blue OLED emitters are less common owing to the extensive π-π stacking of the relatively planer pyrene moieties in condensed state, causing massive red-shifts of the pyrene derivatives' emission spectrum, which often results in greenish blue, bluish green, or green emissions.[7] Also, dye aggregation is accounts for aggregation-induced quenching of the emitter, thus reducing the OLED emission efficiency.[3,7] However, a notable exception to this common case is pyrene derivatives exhibiting AIE.[19,20] Interestingly, these AIE based pyrene derivatives show an enhanced emission in the solid-state as a result of restricted molecular motion. Strategies other than AIE to preserve the desirable optical characteristics of pyrene derivatives include twisting the structure to restrict π-π stacking for relatively small molecules,[21,22] designing polymers/oligomers/dendrimers with pyrene moieties

placed in such a way that they cannot aggregate effectively due to steric effects,[23,24] and applying a suitable host matrix to dilute the pyrene derivative concentration in the EML.[25]

The novel compounds discuss in this chapter are not AIE materials. Therefore these compounds are designed with multiple phenyl and/or tertiary butyl groups, which are attached to the pyrene-benzimidazole cores of compounds A, B, and C, to effectively reduce π stacking of pyrenyl moieties in the solid-state by causing substantial steric hindrance. Benzimidazole moieties in these compounds were used to aid in electron transport since benzimidazole is a well-known electron transporter, particularly when conjugated to organic or transition metal electron donors.[16,26,27] Compounds, A, B, and C were systematically evaluated for morphological, photo-thermal, optical, and electrochemical properties to assess the suitability of these molecules as blue OLED emitters. As expected, compounds A, B, and C showed a systematic reduction in the degree of crystallinity, due to the systematic increase of steric hindrance that prevents efficient solid-state aggregation of these compounds. As a result, a significantly pure blue emission is observed from all three compounds in both solution and solid states. The spectroscopic characteristics of these compounds were thoroughly investigated in terms of absorption, photoluminescence, and PLQY. Since compound B showed the best photo-physical properties among the three compounds investigated, a non-doped OLED prototype was fabricated with compound B as the emissive material for preliminary studies. This OLED prototype showed significantly pure blue electroluminescence as expected, with CIE coordinates of (0.1482, 0.1300). Other OLED performance characteristics including power and current efficiencies and EQE were also determined for this OLED prototype.

3.2. Experimental Section

3.2.1. Materials

Tetrakis(triphenylphosphine)palladium(0), 2-bromo-7-*tert*-butylpyrene, 1,3-dibromo-7-*tert*-butylpyrene, 1,3,6,8-tetrabromopyrene, and 1-phenyl-2-[3-(4,4,5,5-tetramethyl-1,3,2-dioxaborolan-2-yl)phenyl]-1*H*-benzimidazole were purchased from Tokyo Chemical Industries Co. Ltd. (Portland, OR). Bathocuproine (2,9-dimethyl-4,7-diphenyl-1,10-phenanthroline, BCP) was purchased from Sigma-Aldrich (St. Louis, MO). The compounds, $TBAPF_6$ and Fc were purchased from Sigma-Aldrich (St. Louis, MO) and K_2CO_3 was purchased from Fisher Scientific (Fair Lawn, NJ). Analytical grade $CHCl_3$, THF, hexane, EA, 1,4-dioxane, acetone, isopropanol, ACN, and DCM were purchased from Macron (Center Valley, PA). The metals, Al and Ca, were purchased from Angstrom Engineering Inc. (99.999%, Kitchener, ON). Glass slides coated with ITO were purchased from Delta Technologies (Loveland, CO). Column chromatography was performed on silica gel (Sorbent Technologies, 40-63 μm particle diameter) slurry packed into glass columns. Deionized water was obtained from an Elga model PURELAB ultra water-filtration system.

3.2.2. Instrumentation

A scanning UV-vis spectrophotometer (UV-3101PC, Shimadzu, Columbia, MD) was used to obtain absorption spectra and a HORIBA Spex Fluorolog-3-spectrofluorometer (FL3-22TAU3, Jobin-Yvon, Edison, NJ) with entrance and exit slit widths maintained at 3 or 5 nm was used to record photoluminescence spectra. The same spectrofluorometer set up was used for photostability experiments with entrance slit width maintained at 14 nm. Quartz cuvettes (Starna Cells, Atascadero, Ca) with path lengths of 0.4/1 cm (for solutions) and quartz slides (for thin solid films, Ted Pella, Inc., Redding, CA) were used for spectroscopic characterizations. Absolute quantum

yields of compounds were obtained by using a Petite Integrating Sphere (Jobin-Yvon, Edison, NJ) mounted to this spectrofluorometer. A Hi Res Modulated TGA 2950 Thermogravimetric Analyzer (TA Instruments, New Castle, DE) was employed to obtain thermal decomposition onset temperatures. An Autolab electrochemical system coupled with a potentiostat (model PGSTAT 302N, Metrohm, Riverview, FL) was used for CV analysis at room temperature, using a three-electrode system consisting of a platinum disk (3 mm diameter) working electrode, an $Ag/AgNO_3$ non-aqueous reference electrode, and a Pt wire counter electrode (CH Instruments, Austin, TX). The Fc/Fc^+ redox couple was used as internal standard against reference electrode. For CV experiments, ACN/DCM containing $TBAPF_6$ (electrolyte, 1 mM) was used as the solvent. A Bruker Kappa APEX-II DUO diffractometer (Bruker, Madison, WI) was employed to carry out single crystal XRD, whereas a PANalytical Empyrean multipurpose diffractometer (Westborough, MA) with a copper anode was employed to obtain PXRD data. Thin films (75 ±7 nm) of compounds A, B, and C were prepared on clean quartz slides by spin coating (Model WE-650MZ-23NPPB, Laurell Technologies Corporation, North Wales, PA). For this first step, compounds were dissolved in chloroform to prepare dilute solutions (0.1-0.5 mM) and filtered through syringe filters (0.1 µm pore size). These solutions were used to spin coat the materials on quartz slides (100 µL solution volume and 1500-2000 rpm, with 2 min spinning duration).

OLED prototypes were fabricated by employing vacuum thermal deposition. An ultra-high vacuum thermal evaporator (VTE, Angstrom Engineering, Kitchener, ON) was used to deposit metal and organic layers on ITO coated glass substrates using a previously reported procedure.[28] In brief, ITO coated glass substrates were cleaned by sequential ultra-sonication in an aqueous detergent solution, DI water, acetone, and isopropanol. Then, these cleaned substrates were dried overnight inside a glove box and subjected to UV-ozone treatment for 20 min under ambient

conditions. The ozone treated ITO coated glass substrates were immediately returned to the glove box to make OLED prototypes by mounting them onto the VTE chamber. Base pressure of the VTE system was maintained at $< 1 \times 10^{-6}$ Torr throughout the entire material deposition process. Deposition of the metals and organic layers was carried out with rates of 1 Å/s (organic compounds), 0.3 Å/s (Ca), and 2 Å/s (Al). A Bruker Dektak XT surface profilometer (Bruker, Madison, NJ) was used to calibrate the OLED layer thicknesses. The electroluminescence of the OLED prototypes were obtained using a PTI QuantaMaster4/2006SE spectrofluorometer (Photon Technology International, Edison, NJ) combined with an integrating sphere (Labsphere, North Sutton, NH). A Keithley 2601 sourcemeter (Tektronix, Inc., Beaverton, OR) was employed to control and record the current and voltage of OLED prototypes. A SCL-050 lamp standard (Labsphere North Sutton, NH) was used to obtain the total spectral flux to obtain OLED prototype performance.

3.3. Synthesis and Characterization

Three novel pyrene-benzimidazole conjugate compounds, namely, 2-(1,2-diphenyl)-1*H*-benzimidazole-7-*tert*-butylpyrene (compound A), 1,3-di(1,2-diphenyl)-1*H*-benzimidazole-7-*tert*-butylpyrene (compound B), and 1,3,6,8-tetra(1,2-diphenyl)-1*H*-benzimidazolepyrene (compound C), were synthesized via a one-step Suzuki coupling between respective mono-, di-, or tetra-bromopyrenes and 1-phenyl-2-[3-(4,4,5,5-tetramethyl-1,3,2-dioxaborolan-2-yl)phenyl]-1*H*-benzimidazole (Figure 3.1). The synthesis of compound A is described here as a representative protocol for the synthesis of all three compounds. In a typical synthesis, an Airfree flask was charged with 2-bromo-7-*tert*-butylpyrene (341 mg, 1.00 mmol), 1-phenyl-2-[3-(4,4,5,5-tetramethyl-1,3,2-dioxaborolan-2-yl)phenyl]-1*H*-benzimidazole (397 mg, 1.01 mmol), and tetrakis (triphenylphosphine)palladium(0) catalyst (120 mg, 0.1 mmol) in a nitrogen atmosphere.

Next, 1,4-dioxane (degassed, 80 mL) and an aqueous potassium carbonate solution (degassed, 0.2 M, 20 mL) were added to the same flask. The reaction mixture was stirred at 60 ˚C in Airfree flask for 24 h in an argon atmosphere. The crude product was precipitated inside the flask as white needles upon cooling the reaction mixture to room temperature. The crude product was isolated by filtering the reaction mixture under vacuum, followed by air-drying in an ambient temperature. A silica gel flash column chromatography purification was carried out for the crude product with ethyl acetate: hexane (4:6) solvent system to isolate the pure compound as colorless needles (332 ±7 nm, yield 63 ±7%). In the case of product B, the molar ratio used for the synthesis of 1,3-dibromo-7-*tert*-butylpyrene and 1-phenyl-2-[3-(4,4,5,5-tetramethyl-1,3,2-dioxaborolan-2-yl)phenyl]-1*H*-benzimidazole was 1.00:2.05. For the synthesis of product C, the molar ratio of 1,3,6,8-tetrabromopyrene and 1-phenyl-2-[3-(4,4,5,5-tetramethyl-1,3,2-dioxaborolan-2-yl)phenyl]-1*H*-benzimidazole was maintained at 1.00:4.05. Compound B was a yellow solid (580 ±71 mg, yield 73 ±9%) and compound C was a light brown solid (893 ±140 mg, yield 70 ±11%). Products A, B, and C were characterized with ESI-MS/MALDI-MS and NMR spectroscopy. This characterization information is provided in Appendix B.

3.4. Results and Discussion

3.4.1. Solid-State Morphology

Photo-physical properties are often swayed by solid-state conformations of the small molecular organic compounds.[10] Therefore, powder and/or single-crystal XRD experiments were performed for compounds A, B, and C and PXRDs of these compounds were presented in Figure B1 in Appendix B. Accordingly, PXRDs indicate that compounds A, B, and C show a systematic reduction in the degree of crystallinity, as denoted by a gradual reduction of the number of sharp peaks observed in PXRDs. The observed crystallinity trend (i.e., A > B > C) is attributed to the

systematic increase of phenyl and/or alkyl substituents in these compounds (i.e., 3, 4, and 8 alkyl/phenyl groups in compounds A, B, and C, respectively), that progressively reduced π stacking of the pyrenyl moieties by increasing steric hindrance. Amorphous organic compounds are typically preferred for optoelectronic applications than crystalline compounds. This is because amorphous compounds lack non-linear optical, thermal, and electronic characteristics stem from anisotropy.[29,30]

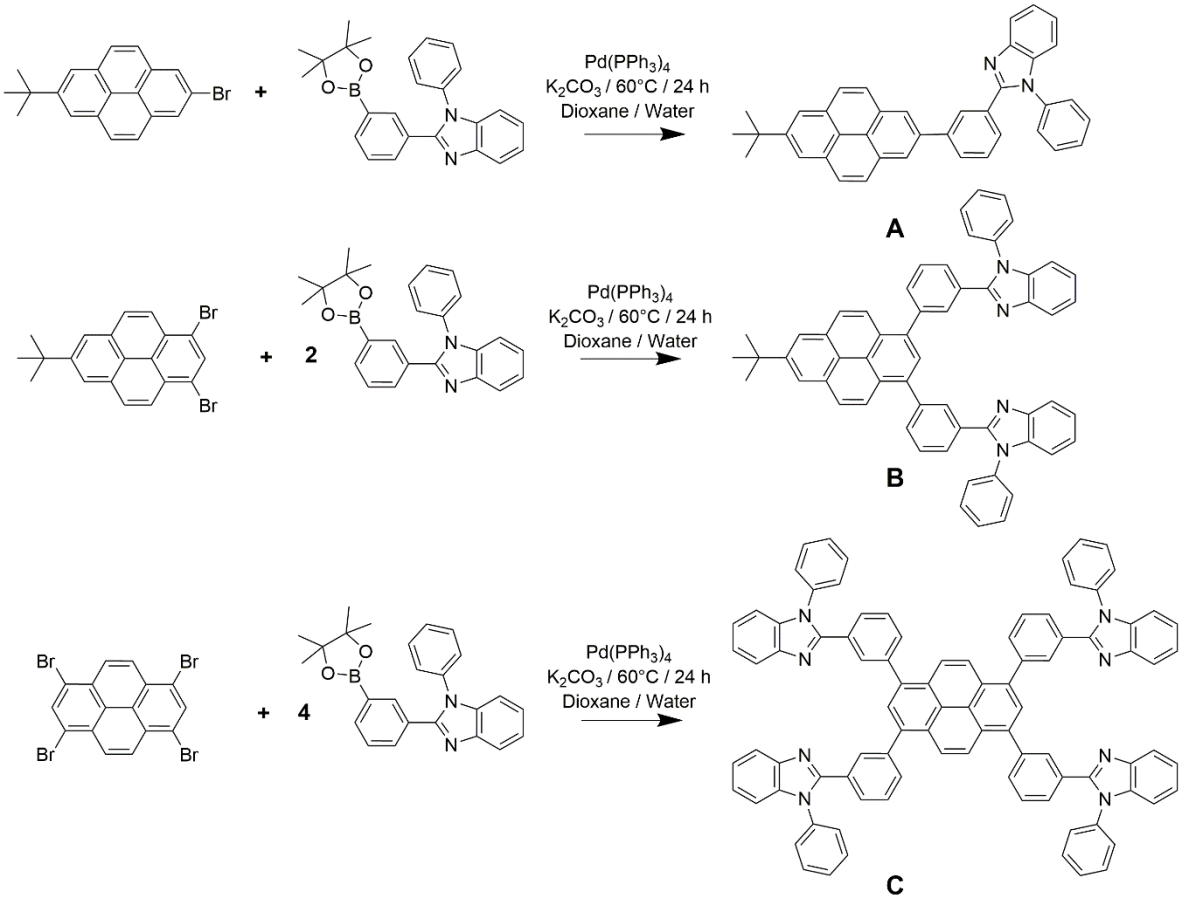

Figure 3.1. Synthesis schemes of pyrene-benzimidazole derivatives, 2-(1,2-diphenyl)-1*H*-benzimidazole-7-*tert*-butylpyrene (compound A), 1,3-di(1,2-diphenyl)-1*H*-benzimidazole-7-*tert*-butylpyrene (compound B), and 1,3,6,8-tetra(1,2-diphenyl)-1*H*-benzimidazolepyrene (compound C).

Since compound A is a highly crystalline compound, single-crystal XRD derived solid-state conformation of compound A was obtained (Figure B2 in Appendix B), and this crystal structure is available in crystallographic information file (CIF) format in the Cambridge Crystallographic

Data Centre (CCDC) under the reference number CCDC 1902159. Interestingly, solid-state packing of compound A (Figure B3 in Appendix B) indicated that two neighboring compound A molecules are paired in head-to-tail fashion, with the closest intermolecular distance between two neighboring benzimidazole N atoms being 5.5 (±3) Å. It is also noted that among aliphatic and aromatic moieties attached to the benzimidazole-pyrene core to induce steric hindrance, the phenyl group which is attached to the N atom of benzimidazole moiety is highly twisted. This phenyl group is positioned nearly orthogonal to the rest of the molecule (Figure B2 in Appendix B), thus causing the highest steric hindrance to prevent dye aggregation in the solid-state. Since the number of this particular phenyl groups increases in compounds A, B, and C systematically, the solid-state packing is drastically affected, as denoted by shifting the molecular morphologies from predominantly crystalline (compound A) to predominantly amorphous (compound C).

3.4.2. Photothermal Stability

Organic blue emitters may undergo various degradation processes to different extents.[31-38] OLED degradation is caused by external factors such as heat, light, moisture, and oxygen and/or internal factors such as design/fabrication errors including formation of pin-holes/deformities, morphological changes of organic layers during operation, and excessive electrical stress in non-optimized designs. For example, it is reported that blue phosphorescent emitters with strong electron withdrawing moieties (i.e., –F, –CN) and with iridium metal centers are more susceptible to degradation, when applied in optoelectronic devices.[31-34] Also, some polymeric blue emitters are susceptible to delamination and/or non-emissive ‘black’ spot forming as a result of morphological changes.[35] Heat generation as a result of biasing of OLEDs due to Joule heating, stems from high resistance of organic layers and non-radiative recombination.[36] Photodegradation of emitters could occur during the material handling, device fabrication, and device operation,

which is induced by light in the presence oxygen.[37,38] Therefore, among the aforementioned factors that induce OLED degradation, susceptibility to photothermal degradation is evaluated for compounds A, B, and C as a preliminary measure to access the stability of these compounds.

The photostabilities of compounds A, B, and C were evaluated using a previously reported time-dependent kinetic fluorescence method.[39] In brief, thin films of compounds A, B, and C on quartz were intensively irradiated with monochromatic light at the respective A_{max} wavelengths for 100 consecutive minutes, while recording the photoluminescence intensity fluctuations at the respective λ_{max} wavelengths. It is assumed that any decrease in the emission intensity recorded with increasing irradiation time is correlated to the extent of photodegradation. Accordingly, the percentage of photodegradation for a compound was estimated using Equation 3.1.

$$Photodegradation\ (\%) = \left(1 - \frac{I}{I_0}\right) \times 100\ \%\ , \qquad (3.1)$$

where I is the emission intensity after the intense irradiation and I_0 is the initial emission intensity (prior to irradiation). Bathocuproine (BCP), which is a well-known electron transport/hole blocking compound, was used as the reference compound. The resultant photodegradation curves were presented in Figure 3.1. Under the aforementioned conditions, BCP showed the highest photodegradation, with approximately a 30% reduction of initial fluorescence intensity under the given experimental conditions (Figure 3.2). This high photobleaching rate observed for BCP is attributed to the high energy excited state, as indicated by the HOMO-LUMO energy gap (Table 3.3), which makes it susceptible to photo-induced side reactions that ultimately lead to substantial photodegradation.[37] Interestingly, compounds A and C showed a 16% and a 14% reduction of relative fluorescence intensity, whereas compound B displayed the minimum photobleaching with only 7% of relative fluorescence intensity decay among tested compounds, under the given experimental conditions. Therefore, it is assumed that compounds A, B, and C were reasonably

photostable than the reference compound. The exact reasons for the observed photostability trend of compounds A, B, and C (A ≤ B < C) is not clear. Photostability fluctuations of these compounds could be attributed to the overall outcome of many complex factors including excited state energy and side reactions, the extent of solid-state molecular interactions, chemical reactivity of materials, particularly towards oxygen[40], and susceptibility to various photobleaching mechanisms that are not fully understood yet.[41]

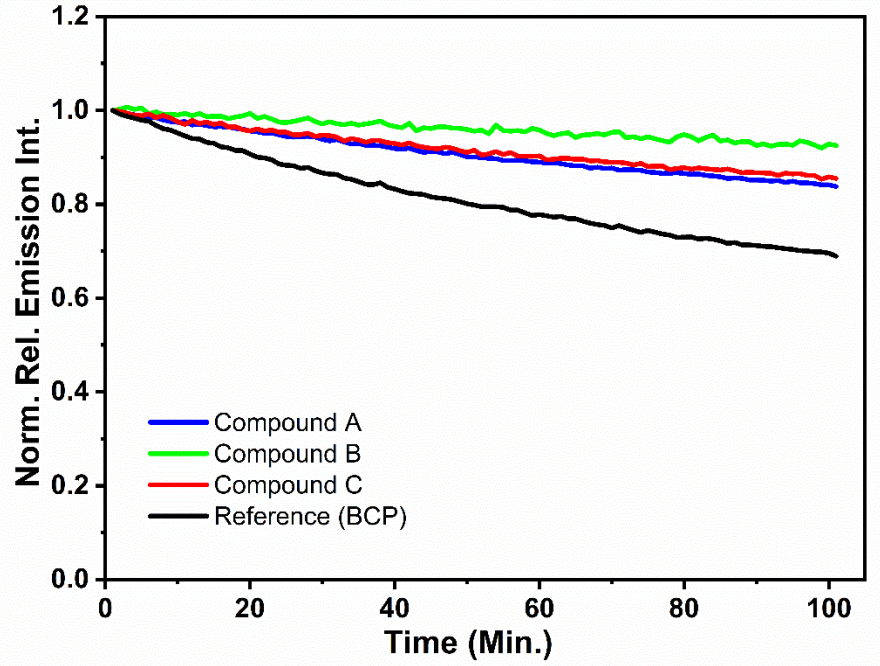

Figure 3.2. Time-dependent relative photoluminescence intensity fluctuation curves of compounds A, B, and C thin films over a time period of 100 min.

Thermal stability of compounds A, B, and C were estimated using TGA.[42] In brief, the compounds (< 5 mg) were gradually heated in the temperature range of 25-600 °C, at a rate of 10 °C/min, in an inert atmosphere. The onset of weight loss (< 5%) is assumed as the onset of thermal decomposition *(T_{onset})*.[42] The resultant TGA profiles of compounds A, B, and C are provided in Figure B4 in Appendix B, and the T_{onset} values are listed in Table 3.1. Accordingly, compounds A, B, and C displayed substantial thermal stabilities with T_{onset} values in the range of 308-467 °C. The T_{onset} trend of the compounds, C < B < A, is attributed to the gradual reduction of highly

thermally stable pyrenyl moiety percentage in compounds A, B, and C (i.e., 38, 25, and 16%, respectively). Accordingly, compound A with the highest percentage of pyrenyl character (38%) showed the highest T_{onset} whereas compound C with the lowest percentage of pyrenyl character (16%) showed the lowest T_{onset} among these three compounds.

Table 3.1. Thermal decomposition onset temperatures (T_{onset}) of compounds A, B, and C.

Compound	T_{onset} (°C)
Compound A	467
Compound B	378
Compound C	308

3.4.3. Spectral Properties in Solutions and in Solid States

Normalized UV-vis absorption and photoluminescence spectra of compound B and parent compounds of compound B, i.e., pyrene derivative (P_1) and benzimidazole derivative (P_2), in DCM solution (5-10 μM), were displayed in Figure 3.3. Similarly, absorption and photoluminescence spectra of compounds A, C, and the parent compounds were recorded in DCM (5-10 μM) and presented in Figures B5 and B6 in Appendix B. It is noted that the spectral characteristics of compounds A, B, and C are complex and could be related to both parent compounds (Figure 3.2 and Figures B5 and B6 in Appendix B). For example, absorption and photoluminescence behaviors of compound B show similarities to that of its parent compounds (Figure 3.3). However, it is noted that spectral characteristics of compound B are unique in terms of shape, relative peak intensities, and peak positioning. For example, although the absorption and photoluminescence spectra of compound B is positioned closely to the absorption and photoluminescence spectrum of the parent compound P_1, vibrational features of these spectra were significantly reduced in compound B than in P_1.

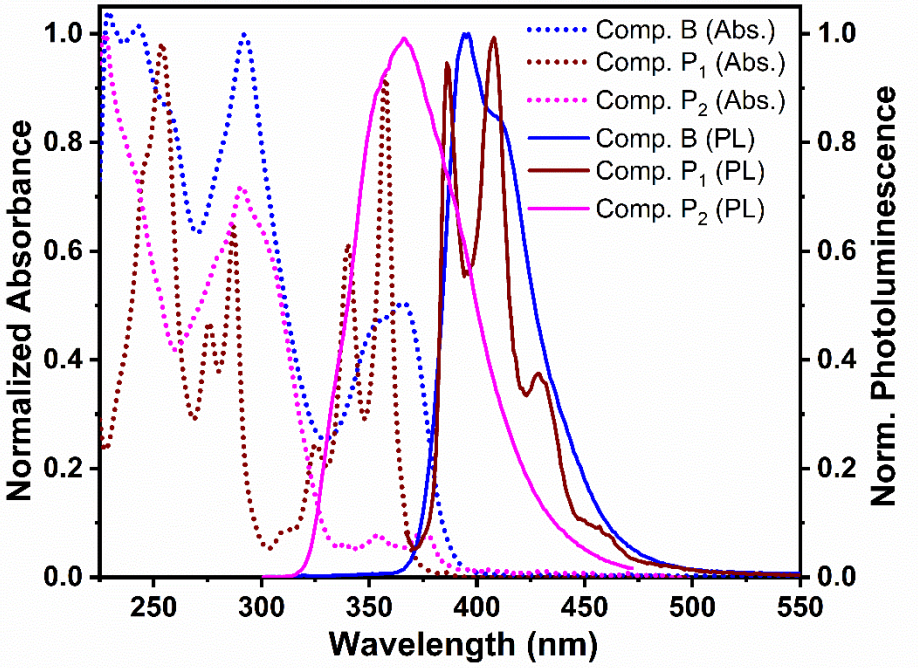

Figure 3.3. Normalized UV-vis absorption (Abs.) and photoluminescence (PL) spectra of compound B and its parent compounds: pyrene derivative (P_1) and benzimidazole derivative (P_2) in DCM.

Figure 3.4 displays the normalized absorption and photoluminescence spectra of pyrene-benzimidazole derivatives (compounds A, B, and C) in dilute DCM solutions (1 µM-10 µM), as well as in thin films on quartz. All three compounds showed multiple absorption peaks corresponding to multiple electronic transitions, with/without distinguishable vibronic features (i.e., shoulders, peak clusters). The absorption maxima (A_{max}) values for compounds A, B, and C are summarized in Table 3.2 for solution and solid states. Noteworthy, a systematic red-shift of A_{max} values was observed for compounds A, B, and C, in particular, for the lowest energy absorption bands. This could be due to the systematic increase of the extended conjugation in these compounds. In solid-state, these absorption spectra were widened as denoted by an increase in the FWHM values. For example, FWHM values of the lowest energy absorption bands were widened by 12-21 nm for compounds A, B, and C in the solid-state than in solution (Table 3.2). Also, these absorption spectra were red-shifted. For example, the lowest energy absorption bands were red-

shifted by 4-6 nm for compounds A, B, and C in the solid-state than in solution (Table 3.2). These spectral changes in the solid-state suggest that, despite the steric hindrance caused by phenyl/t-butyl moieties, compounds A, B, and C were able to aggregate in the solid-state to different extents.

Table 3.2. Absorption data summary for compounds A, B, and C.

Compound	A_{max} (nm)		FWHM (nm)	
	Sol[x]	Film	Sol[x]	Film
A	284	285	43	73
	326	329	12	18
	342	347	8	20
B	243, 259 [y]	N/A	42	N/A
	293	296	41	87
	366, 351[y]	372	47	61
C	242	N/A	58	N/A
	303, 293 [y]	309	44	55
	378, 396 [y]	400	53	74

[x] In DCM solution (10 µM), [y] Prominent shoulder peak maxima, N/A: Not available within the scanned wavelength range.

Photoluminescence spectra of compounds A, B, and C were also presented in Figure 3.4 for both solution and solid states, and a summary of photoluminescence characteristics was provided in the Table 3.3. Accordingly, photoluminescence spectra of all three compounds have a single broad peak, which contains recognizable shoulder(s) in the solution state but no such shoulders(s) recognizable in the solid-state, suggesting excimer formation of pyrene, particularly in the solid-state.[43] The emission maxima (λ_{max}) values recorded in DCM solution were found in the range of 395-424 nm, whereas in solid-state λ_{max} values were ranged from 452-456 nm. According to these λ_{max} values, it is noted that solid-state photoluminescence of compounds A, B, and C was significantly red-shifted than solution by 61, 58, and 30 nm, respectively. The λ_{max} values of all three compounds in solid-state were very close as a result of systematic reduction of the Stokes shifts, suggesting a gradual reduction of dye aggregation in the solid-state. Also, a systematic reduction of the peak broadening in solid-state, as indicated by gradual reduction of FWHM values

(81, 72, and 52 nm for compounds A, B, and C) was observed, further confirming a gradual reduction of dye aggregation for the reasons discussed in section 3.4.1.

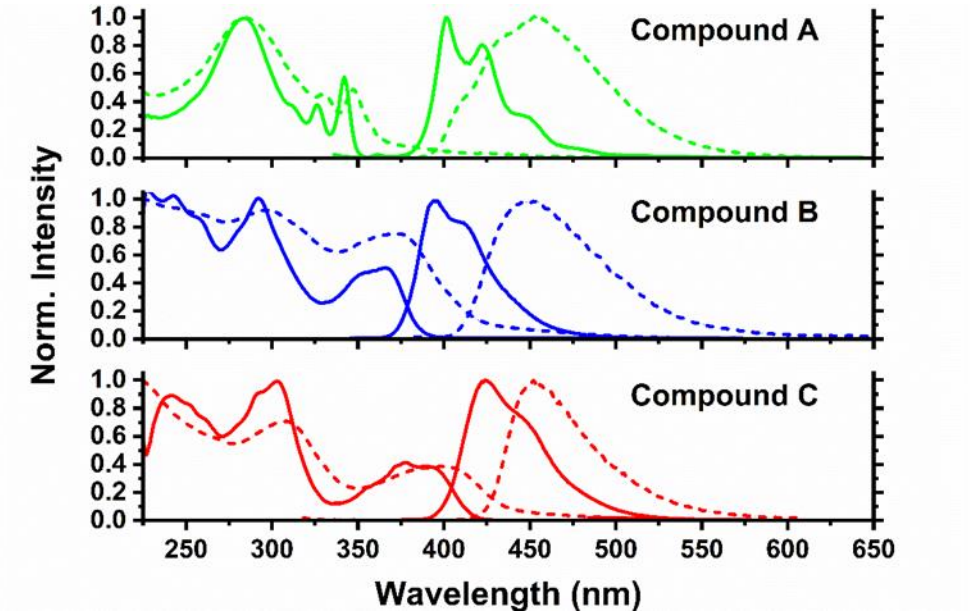

Figure 3.4. Normalized UV-vis absorption and fluorescence spectra of compound A, B, and C in DCM (1 μM, solid lines) and neat films (dashed lines).

The photoluminescence of these compounds is mostly confined to violet-blue region (in DCM solution) and blue region (in the solid-state) of the EMS. It is noted that solid-state emission of these compounds does not contain harmful near UV radiation. The color of these compounds has been assigned in accordance with the CIE coordinates and are listed in Table 3.3. In summary, compounds A, B, and C have an average CIE coordinates of (0.160 ±0.005, 0.029 ±0.009) in DCM solution and (0.152 ±0.007, 0.126 ±0.005) in solid-state. These CIE coordinates comply with the general criterion for blue emitters ($y < 0.15$, $(x + y) < 0.30$),[5] although these values are slightly off from NTSC and EBU standards, which require average CIE coordinates of (0.150 ±0.010, 0.07 ±0.010) for blue emitters in electronic displays.[4] However, many blue emitters with significant commercial interest (i.e., emitters that show high OLED device performance) often have CIE coordinates that are not fully compliant with NTSC/EBU standards.[44-46]

Table 3.3. Summary of emission properties of compound A, B, and C.

Compound	λ_{max} (nm)		FWHM (nm)		Stokes Shift (nm)		CIE Coordinates (x,y)	
	Sol[x]	Film	Sol[x]	Film	Sol[x]	Film	Sol[x]	Film
A	395	456	45	81	53	106	0.1620, 0.0197	0.1483, 0.1214
B	396	452	43	72	30	82	0.1635, 0.0306	0.1482, 0.1300
C	424	454	49	52	46	54	0.1548, 0.0373	0.1600, 0.1275

[x] In DCM solution (1μM)

3.4.4. PLQY

PLQY is the ratio of emitted photons to absorbed photons by a fluorophore and is influenced by factors such as optical characteristics, molecular rigidity, and inter/intra molecular interactions.[47] It is noted that a dye with a high PLQY does not necessarily exhibit high electroluminescence when applied to an OLED device and may not exhibit similar emission behavior (i.e., emission peak shape, intensity, position, efficiency etc.). This is because of the differences in emission and/or quenching mechanisms, influence of the other semiconductor layers in the device, device architecture, and physical/electrical properties of the emissive layer.[48,49] Also, compounds with low PLQY values often not show efficient electroluminescence. Therefore, it is important to estimate PLQY values of compounds A, B, and C, to further understand optical characteristics of these compounds. Accordingly, absolute PLQY values were measured using an integration sphere for solution and thin films deposited on quartz.[50] The resultant PLQY values of compounds A, B, and C are presented in Table 3.4. It is noted that all three compounds have substantial PLQY values in both solution and solid states. The PLQY values for both solution and solid-states increases in the following order, A < B < C. This trend is attributable to the systematic decrease in dye aggregation to reduce aggregation induced quenching. However, PLQY is reduced

in the solid-state than in solution, suggesting some dye aggregation related quenching of these compounds in the solid-state is inevitable.

Table 3.4. Quantum yields and lifetimes of compounds A, B, and C.

Compound	PLQY (%)	
	Solution	Film
Compound A	43 [x]	35
Compound B	64 [x]	51
Compound C	96 [y]	56

[x] In ACN solvent, [y] In DCM solvent

3.4.5. Electronic Properties

Equations 3.2 and 3.3 were employed to calculate HOMO and LUMO energies of compounds A, B, and C by employing cyclic voltammetry, which is the most common experimental method for estimating the HOMO and LUMO energies of organic semiconductors.[51] The cyclic voltammograms obtained for compounds A, B, and C were presented in Figure B7 in Appendix B. The calculated energies of frontier orbitals are listed in Table 3.5. Compounds A, B, and C showed quasi-reversible CVs with only oxidation peaks (Figure B7 in Appendix B). Furthermore, compounds A and B showed two distinguishable peaks (with prominent shoulders). These multiple oxidations can be attributed to the oxidations of two imidazole nitrogens. The solvent window for ACN (used for compounds A and B) was wider than DCM (used for compound C), therefore, only the first oxidation was recorded for compound C. However, the onset of oxidation/reduction is the most important piece of information obtained from the cyclic voltammograms to estimate the oxidation potential (E_{ox}).[51] For molecules with quasi reversible cyclic voltammograms with only oxidation peak(s), LUMO is theoretically calculated by the use of band gap (E_g) and HOMO values, which are obtained experimentally (Equations 3.2. and 3.3).

$$HOMO\ (eV) = -1e\ [E_{ox} + 4.71]\ V \quad (3.2)$$

$$LUMO\ (eV) = E_g\ - HOMO\ eV \quad (3.3)$$

The E_g values of compounds A, B, and C were estimated using UV-vis absorption spectra, hence termed the optical band gap. This simple E_g calculation method is widely used for organic semiconductor materials by employing Equation 3.4.[52] This method is based on the hypothesis that the onset at the higher wavelength side of the absorption spectrum corresponds to the minimum energy required to promote a ground state (HOMO) electron to the first excited state (LUMO), which is true for most small molecular organic semiconductors.

$$E_g\ (eV) = hf = h.\left(\frac{c}{\lambda_{onset}}\right) = \frac{1240}{\lambda_{onset}}\ eV, \qquad (3.4)$$

where h is the Planck's constant (6.626 x 10^{-34} Js), c is the speed of light in a vacuum (3.00 x 10^{-8} ms^{-1}), and λ_{onset} is the wavelength of the absorption onset (nm). Accordingly, the value of (h × c) is also a constant (1240 eV. nm). Accordingly, HOMO and LUMO values calculated in the aforementioned methods for compounds A, B, and C were found in the range of (-5.10 to -5.46) and (-2.23 to -2.56) eV. It is noted that E_g is gradually reduced with increasing the extended conjugation in these compounds. Computed HOMO and LUMO values of these compounds are in a range, in which, it is easy to find energetically matching supporting organic semiconductors (i.e., charge transporters/injectors/blockers) and to the work functions of most metal electrodes, making it easier to incorporate these compounds into existing OLED architectures.[53]

3.4.6. Characterization of OLED Prototype with Compound B as the EML

Compound B, which exhibited the best overall photo-physical characteristics among the three compounds investigated, was used to fabricate an OLED prototype for the preliminary OLED performance evaluations. Although doping may enhance the efficiency of OLED devices by controlling aggregation induced quenching and/or inducing favorable host-dopant energy transfers interactions, a non-doped OLED prototype was fabricated at this preliminary stage to reduce the device complexity and study the electroluminescence characteristics of the emitter itself.

Table 3.5. Summary of the electronic properties of compounds A, B, and C.

Compound	E_g (eV)	HOMO (eV)	LUMO (eV)
Compound A [y]	3.16	-5.39	-2.23
Compound B y	2.90	-5.46	-2.56
Compound C z	2.79	-5.10	-2.31
BCP	3.65[x]	-6.61[x]	-2.95[x]

[x] These values were obtained from reference 48. [y] In ACN solvent. [z] In DCM solvent.

An optimized OLED prototype was fabricated by vacuum thermal deposition with a configuration of ITO (140 nm)/ NDB (30 nm)/ Compound B (30 nm)/ TPBI (30 nm)/ Ca (10 nm) /Al (100 nm), as schematically shown in Figure 3.5 (A). Here, NDB and TPBI were used as charge transport layers, ITO and Ca are electrode materials, and compound B is the non-doped emissive layer. The performance of this OLED prototype was assessed by calculating CIE coordinates, current density, luminance, efficiency (in terms of power and current), and EQE in accordance with previously reported protocols.[3,54] This OLED device showed a blue electroluminescence with λ_{max} at 454 nm, while turning on at 3 V. EQE, which is the ratio of emitted photons into the viewing direction to injected charges, was recorded as 0.35 (± 0.04) % at 5.5 V. Power and current efficiencies, which provide insights into the energy consumption and light emitting ability of an OLED, were recorded as 1.2 (±0.6) lmW^{-1} and 0.17 (± 0.2) cdA^{-1}, respectively at 5.5 V. The OLED performance plots of this prototype are provided in Figure B8 in Appendix B. CIE coordinates of the electroluminescence spectrum is identical to that in solid-state (0.1482, 0.1300), implying blue emission with substantial spectral purity. Luminance (i.e., the amount of light emitted per unit surface area of OLED weighed by the visual response of the human eye) of the device reached 100 (± 6) cdm^{-2} at 5.5 V.

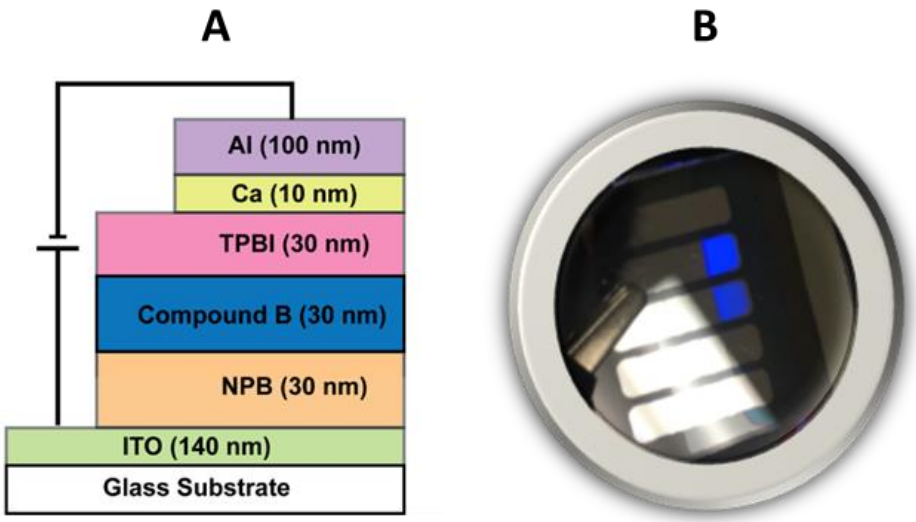

Figure 3.5. A simple schematic diagram of the OLED prototype (A) and a photograph of actual OLED showing blue emission at 3 V (B).

A comparison of photoluminescence (in DCM solution and in thin films) and electroluminescence (as EML in the OLED prototype) of compound B is presented in Figure 3.6. It is noted that the luminescence in solid state (both photo and electroluminescence) may affected by dye aggregation as denoted by band broadening and red-shifting than luminescence in the solution state. Noteworthy, photoluminescence and solid-state electroluminescence are nearly completely superimposable, suggesting both emission mechanisms are comparable.[5] Interestingly, solid-state luminescence of this OLED prototype does not contain near UV radiation, thus is safe to human eye when applied in electronic screens.

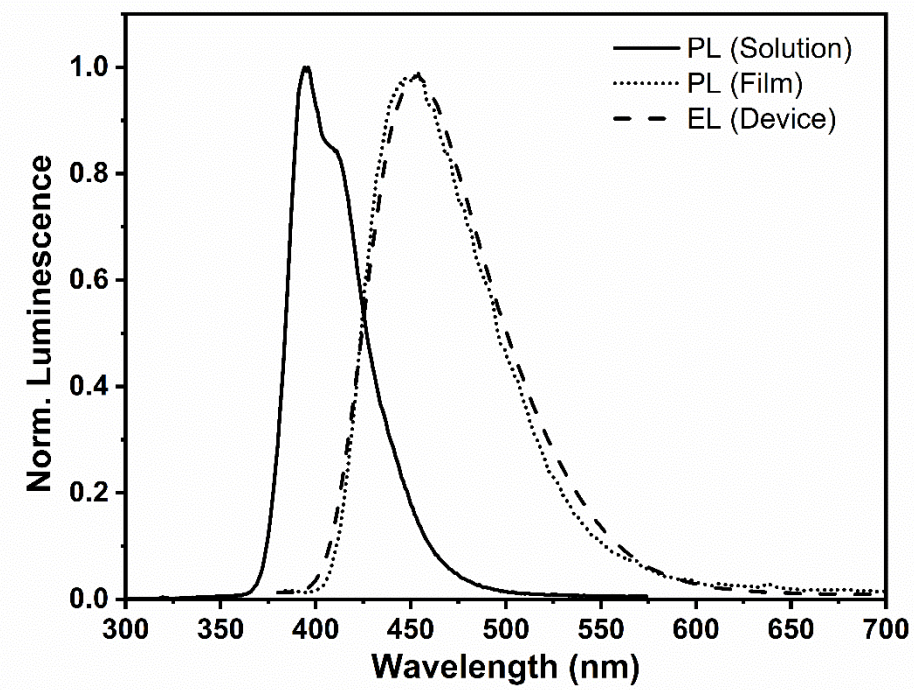

Figure 3.6. Normalized photoluminescence (PL) from solution and solid states, and electroluminescence from the OLED prototype recorded for compound B.

3.5. Conclusions

Three novel organic blue emitters, i.e., 2-(1,2-diphenyl)-1*H*-benzimidazole-7-*tert*-butylpyrene (compound A), 1,3-di(1,2-diphenyl)-1*H*-benzimidazole-7-*tert*-butylpyrene (compound B), and 1,3,6,8-tetra(1,2-diphenyl)-1*H*-benzimidazolepyrene (compound C) were synthesized via a Suzuki coupling reaction. These compounds displayed significantly pure blue emission with reasonably high spectral purity in the solid-state compared to many pyrene derivatives reported in the literature, which emit a bluish green or greenish blue light as a result of excimer formation and dye aggregation. Spectroscopic characteristics, such as absorption, photoluminescence, and quantum yield, as well as electronic properties based on cyclic voltammetry and UV-vis absorption of these novel compounds were found suitable for optoelectronic applications. Compound A, B, and C showed a systematic decrease in the degree of crystallinity, as elucidated by powder X-ray diffraction analysis. An OLED prototype fabricated using compound B as the non-doped emissive

layer, which displayed a blue electroluminescence with CIE coordinates of (0.1482, 0.1300), with an EQE of 0.35 (± 0.4) % at 5.5 V, at which approximately 100 (± 6) cdm^{-2} luminance was recorded.

3.6. References

1. Tang, C. W.; Van Slyke, S.A.: Organic electroluminescent diodes. *Applied Physics Letters* **1987**, *51*, 913-915.

2. Gupta, A. S.: *Organic Light Emitting Diodes (OLEDs): Technologies and Global Markets*; BCC Research, Massachusetts, USA, **2015**; pp. 7-14, 90-120.

3. Su, W. Printed organic light emission and display. In *Printed Electronics*; Editors Cui, Z.; John Wiley & Sons; New York, USA, **2016,** pp. 251-260.

4. Zhu, M.; Yang, C.: Blue fluorescent emitters: Design tactics and applications in organic light-emitting diodes. *Chemical Society Reviews* **2013**, *42*, 4963-4976.

5. Yang, X.; Xu, X.; Zhou, G.: Recent advances of the emitters for high performance deep-blue organic light-emitting diodes. *Journal of Material Chemistry C* **2015**, *3*, 913-944.

6. Kuma, H.; Hosokawa, C.: Blue fluorescent OLED materials and their application for high-performance devices. *Science and Technology Advanced Materials* **2014**, *15*, Article 034201.

7. Hu, J.-Y.; Yamato, T.: Synthesis and photophysical properties of pyrene-based multiply conjugated shaped light-emitting architectures: Toward efficient organic-light-emitting diodes. In *Organic Light Emitting Diode - Material, Process and Devices*; Editors Ko, S. H.; InTech: Rijeka, Croatia, **2011**; pp 22-54.

8. Tao, S.; Zhou, Y.; Lee, C.-S.; Lee, S.-T.; Huang, D.; Zhang, X.: Highly efficient nondoped blue organic light-emitting diodes based on anthracene-triphenylamine derivatives. *Journal of Physical Chemistry C* **2008,** *112*, 14603-14606.

9. Kim, S.-K.; Yang, B.; Park, Y.-I.; Ma, Y.; Lee, J.-Y.; Kim H.-J.; Park, J.: Synthesis and electroluminescent properties of highly efficient anthracene derivatives with bulky side groups. *Organic Electronics* **2009,** *10*, 822-833.

10. Moorthi, J. N.; Venkatakrishnan, P.; Natarajan, P.; Huang, D.-F.; Chow, T. J. De novo design for functional amorphous materials: synthesis and thermal and light-emitting properties of *Twisted* anthracene-functionalized bimesitylenes. *Journal of the American Chemical Society* **2008**, *130*, 17320-17333.

11. Tao, S.; Zhou, Y.; Lee, C.-S.; Zhang, X.; Lee, S.-T.: High-efficiency nondoped deep-blue-emitting organic electroluminescent device. *Chemistry of Materials* **2010,** *22*, 2138-2141.

12. Chou, H.-H.; Chen, Y.-H.; Hsu, H.-P.; Chang, W.-H.; Chen, Y.-H.; Cheng, C.-H.: Synthesis of diimidazolylstilbenes as n-type blue fluorophores: alternative dopant materials for highly efficient electroluminescent devices. *Advanced Materials* **2012,** *24*, 5867-5871.

13. Kuo, C.-J.; Li, T.-Y.; Lien, C.-C.; Liu, C.-H.; Wu, F.-I.; Huang, M.-J.: Bis(phenanthroimidazolyl)biphenyl derivatives as saturated blue emitters for electroluminescent devices. *Journal of Materials Chemistry* **2009,** *19*, 1865-1871.

14. Chien, C.-H.; Chen, C.-K.; Hsu, F.-M.; Shu, C.-F.; Chou, P.-T.; Lai, C.-H.: Multifunctional deep-blue emitter comprising an anthracene core and terminal triphenylphosphine oxide groups. *Advanced Functional Materials* **2009,** *19*, 560-566.

15. Zhu, M.; Wang, Q.; Gu, Y.; Cao, X.; Zhong, C.; Ma, D.; Qin, J.; Yang, C.: Efficient deep-blue emitters composed of an anthracene core and terminal bifunctional groups for nondoped electroluminescence. *Journal of Materials Chemistry* **2011,** *21*, 6409-6415.

16. Huang, J.; Su, J.-H.; Li, X.; Lam, M.-K.; Fung, K.-M.; Fan, H.-H., Cheah, K.-W.; Chen, C. H.; Tian, H.: Bipolar anthracene derivatives containing hole- and electron-transporting moieties for highly efficient blue electroluminescence devices. *Journal of Materials Chemistry* **2011,** *21*, 2957-2964.

17. Li, Z. H.; Wong, M. S.; Fukutani, H.; Tao, Y.: Synthesis and light-emitting properties of bipolar oligofluorenes containing triarylamine and 1,2,4-triazole moieties. *Organic Letters* **2006**, *8*, 4271-4274.

18. Figueira-Duarte, T.; Mullen, K.: Pyrene-based materials for organic electronics. Chemical Reviews **2011**, *111*, 7260-7314.

19. Zhao, Z.; Chen, S.; Lam, J. W. Y.; Wang, Z.; Lu, P.; Mahtab, F.; Sung, H. H. Y.; Williams, I. D.; Ma, Y.; Kwok, H. S.; Tang, B. Z.: Pyrene-substituted ethenes: aggregation-enhanced excimer emission and highly efficient electroluminescence. *Journal of Materials Chemistry* **2011**, *21*, 7210-7216.

20. Zhang, Y.; He, B.; Liu, J.; Hu, S.; Pan, L.; Zhao, Z.; Tang, B. Z.: Aggregation-induced emission and the working mechanism of 1-benzoyl and 1-benzyl pyrene derivatives. *Physical Chemistry Chemical Physics* **2018**, *20*, 9922-9929.

21. Lo, M. Y.; Zhen, C.; Lauters, M.; Jabbour. G. E.; Sellinger, A.: Organic-inorganic hybrids based on pyrene functionalized octavinylsilsesquioxane cores for application in OLEDs. *Journal of the American Chemical Society* **2017**, *129*, 5808-5809.

22. Chan, K. L.; Lim, J. P. F.; Yang, X.; Dodabalapur, A.; Jabbour, G. E.; Sellinger, A.: High efficiency pyrene-based blue light emitting diodes: aggregation suppression using a calixarene 3D-scaffold. *Chemical Communications* **2012**, *48*, 5106-5108.

23. Yuan, W.; Yuan, J.; Zhou, M.; Pan, C.: Synthesis, characterization, and fluorescence of pyrene-containing eight-arm star-shaped dendrimer-like copolymer with pentaerythritol core. *Journal of Polymer Science Part A: Polymer Chemistry* **2008**, *46*, 2788-2798.

24. Liu, F.; Lai, W.-Y.; Tang, C.; Wu, H.-B.; Chen, Q.-Q.; Peng, B.; Wei, W.; Huang, W.; Cao, Y.: Synthesis and characterization of pyrene-centered starburst oligofluorenes. *Macromolecular Rapid Communications* **2008**, *29*, 659-664.

25. Chercka, D.; Yoo, S.-J.; Baumgarten, M.; Kim, J.-J.; Mullen, K.: Pyrene based materials for exceptionally deep blue OLEDs. *Journal of Materials Chemistry C* **2014**, *2*, 9083-9086.

26. Hung, W.-Y.; Chi, L.-C.; Chen, W.-J.; Chen, Y.-M.; Chou, S.-H.; Wong, K.-T.: A new benzimidazole/carbazole hybrid bipolar material for highly efficient deep-blue electrofluorescence, yellow-green electrophosphorescence, and two-color-based white OLEDs. *Journal of Materials Chemistry* **2010,** *20*, 10113-10119.

27. Ge, Z.; Hayakawa, T.; Ando, S.; Ueda, M.; Akiike, T.; Miyamoto, H.; Kajita, T.: Kakimoto, M.: Solution-processable bipolar triphenylamine-benzimidazole derivatives for highly efficient single-layer organic light-emitting diodes. *Chemistry of Materials* **2008**, *7*, 2532-2537.

28. Spindler, J. P.; Hamer, J. W.; Kondakova, M. E. OLED manufacturing equipment and methods. In *Handbook of Advanced Lighting Technology*; Editors Karlicek, R.; Sun, C.-C.; Zissis, G.; Ma, R.: Springer, New York, USA, **2015**, pp 417-441.

29. Evans, O. R.; Lin, W.: Crystal engineering of NLO materials based on metal-organic coordination networks. *Accounts of Chemical Research* **2002**, *7*, 511-522.

30. Chemla, D. S.; Zyss, J. Quadratic non-linear optics and optimization of the second-order nonlinear optical response of molecular crystals. In *Nonlinear Optical Properties of Organic Molecules and Crystals*, Editors Chemla, D. S.; Zyss, J.; Academic Press, New York, USA, **1987**, pp 107-154.

31. Schmidbauer, S.; Hohenleutner, A.; Konig, B.: Chemical degradation in organic light-emitting devices: Mechanisms and implications for the design of new materials. *Advanced Materials* **2013**, *25*, 2114-2129.

32. Sivasubramaniam, V.; Brodkorb, F.; Hanning, S.; Loebl, H. P.; van Elsbergen, V.; Boerner, H.; Scherf, U.; Kreyenschmidt, M.: Fluorine cleavage of the light blue heteroleptic triplet emitter FIrpic. *Journal of Fluorine Chemistry* **2009**, *130*, 640-649.

33. Kondakov, D. Y.: Device degradation, In *OLED Fundamentals, Materials, Devices, and Processing of Organic Light-Emitting Diodes*, Editors Gaspar, D. J.; Polikarpov, E.; CRC Press, FL, USA, **2015**, pp 339-365.

34. Im, Y.; Kim, M.; Cho, Y. J.; Seo, J.-A.; Yook, K. S.; Lee, J. Y.: Molecular design strategy of organic thermally activated delayed fluorescence emitters. *Chemistry of Materials* **2017**, *29*, 1946-1963.

35. Savvate'ev, V. N.; Yakimov, A. V.; Davidov, D.: Degradation of nonencapsulated polymer-based light-emitting diodes: Noise and morphology. *Applied Physics Letters* **1997**, *71*, 3344.

36. Tyagi, P.; Srivastava, R.; Giri, L. I.; Tuli, S.; Lee, C.: Degradation of organic light emitting diode: Heat related issues and solutions. *Synthetic Metals* **2016**, *216*, 40-50.

37. Schmidbauer, S.; Hohenleutner, A.; König, B.: Studies on the photodegradation of red, green and blue phosphorescent OLED emitters. *Beilstein Journal of Organi Chemistry* **2013**, *9*, 2088-2096.

38. Wang, X. Z.; Gao, X. D.; Zhou, Y.C.; Xie, Z.T.; Song, Q.L.; Ding, X.M.; Hou, X.Y.: Photodegradation of organic light-emitting devices observed in nitrogen-filled environment. *Thin Solid Films* **2008**, *516*, 2171-2174.

39. De Silva, T. P. D.; Sahasrabudhe, G.; Yang, B.; Wang, C.-H.; Chhotaray, P. K.; Nesterov, E. E.; Warner, I. M.: Influence of anion variations on morphological, spectral, and physical properties of the propidium luminophore. *Journal of Physical Chemistry A* **2019**, *123*, 111-119.

40. Christ, T.; Kulzer, F.; Bordat, P.; Basche, T.: Watching the photo-oxidation of a single aromatic hydrocarbon molecule. *Angewandte Chemie International Edition* **2001**, *40*, 4192-4195.

41. Hoogenboom, J. P.; van Dijk, E. M.; Hernando, J.; van Hulst, N. F.; Garcia-Parajo, M. F.: Power-law-distributed dark states are the main pathway for photobleaching of single organic molecules. *Physics Review Letters* **2005**, *95*, 097401.

42. Eshetu, G. G.; Jeong, S.; Pandard, P.; Lecocq, A.; Marlair, G.; Passerini, S.: Comprehensive insights into the thermal stability, biodegradability, and combustion Chemistry of pyrrolidinium-based ionic liquids. *ChemSusChem* **2017**, *10*, 3146-3159.

43. Valeur, B.: *Molecular Fluorescence: Principles and Applications*; Wiley-VCH Verlag GmbH, Weinheim, Germany, **2001**; pp. 92-98.

44. Lee, J.; Sen, H.-F.; Batagoda, T.; Coburn; C.; Djurovich, P. I.; Thompson, M. E.; Forrest, S. R.: Deep blue phosphorescent organic-light emitting diodes with very high brightness and efficiency. *Nature Materials* **2016**, *15*, 92-98.

45. Zhang, Y.; Lee, J.; Forrest, S. R.: Tenfold increase in the lifetime of blue phosphorescent light-emitting diodes. *Nature Communications* **2014**, *5*, 5008.

46. Bui, T.-T.; Goubard, F.; Ibrahim-Ouali, M.; Gigmes, D.; Dumur, F.: Recent advances on thermally activated delayed fluorescence (TADF) emitters for organic light-emitting diodes. *Beilstein Journal of Organic Chemistry* **2018**, *14*, 282-308.

47. Lakowicz, J. R. *Principles of Fluorescence Spectroscopy*; Kluwer Academic/Plenum Publishers: New York, USA, **1999**, pp 10-12, 452.

48. Song, H.-Z.; Bao, X.-M.; Li, N.-S.; Zhang, J.-Y.: Relation between electroluminescence and photoluminescence of Si^+-implanted SiO_2. *Journal of Applied Physics* **1997**, *82*, 4028.

49. Anderson, M. R.; Yu, G.; Heeger, A. J.: Photoluminescence and electroluminescence of films from soluble PPV-polymers. *Synthetic Metals* **1997**, *85*, 1275-1276.

50. Zhou, Y.; He, Q.; Yang, Y.; Zhong, H.; He, C.; Sang, G.; Liu, W.; Yang, C.; Bai, F.; Li, Y.: Binaphthyl-containing green- and red-emitting molecules for solution-processable organic light-emitting diodes. *Advanced Functional Materials* **2008**, *18*, 3299-3306.

51. Costa, J. C. S.; Taveira, R. J. S.; Lima, C. F. R. A. C.; Mendes, A.; Santos, L. M. N. B. F.: Optical band gaps of organic semiconductor materials. *Optical Materials* **2016**, *58*, 51-60.

52. Bera, D.; Qian, L.; Tseng, T.-K.; Holloway, P. H.: Quantum dots and their multimodal applications: A review. Materials (Basel) 2010, *3*, 2260-2345.

53. Forrest, S. R.; Bradley, D. D. C.; Thompson, M. E.: Measuring the efficiency of organic light-emitting devices. *Advanced Materials* **2003**, *15*, 1043-1048.

CHAPTER IV. INFLUENCE OF ANION VARIATIONS ON PHOTO-PHYSICAL PROPERTIES OF THE PROPIDIUM LUMINOPHORE[1]

4.1. Introduction

Propidium iodide (3,8-diamino-5-[3-(diethylmethylammonio)propyl]-6-phenylphenanthridinium diiodide, [P][I]) is a well-known red fluorescent dye, often used for staining nucleic acids in human cells, animal cells, and micro-organisms.[1-7] Consequently, [P][I] is widely used in flow cytometry[1-3] and other related biological applications[4-7]. In this study, the typical iodide counteranion of [P][I] was replaced with three relatively hydrophobic and bulky organic anions containing systematically increasing chain length and number of fluorine atoms: trifluoromethanesulfonate/[TfO], bis(trifluoromethanesulfonyl)imide/[NTf_2], and bis(perfluoroethylsulfonyl)imide/[BETI]. The resultant solid phase organic salts were propidium trifluoromethanesulfonate/[P][TfO], propidium bis(trifluoromethanesulfonyl)imide /[P][NTf_2], and propidium bis(pentafluoroethylsulfonyl)imide/[P][BETI]. These novel propidium salts are collectively termed propidium GUMBOS (PGUMBOS), as the acronym GUMBOS (*g*roup of *u*niform *m*aterials *b*ased on *o*rganic *s*alts) has been coined for solid-state organic salts to distinguish them from liquid state organic salts, i.e., ionic liquids.[8] Many task-specific GUMBOS have been designed by our group, and have been derived from a wide variety of organic compounds for a range of applications such as rhodamine GUMBOS with selective cytotoxicity for chemotherapy,[9] aminopyrene GUMBOS with optimized hydrophobicity for matrix assisted laser desorption/ionization (MALDI) mass spectrometry,[10] porphyrin GUMBOS with enhanced vapor sensitivity for quartz crystal microbalance (QCM) sensors,[11] cyanine GUMBOS for dye-sensitized

[1] This Chapter previously appeared as De Silva, T. P. D.; Sahasrabudhe, G.; Yang, B.; Wang, C.-H.; Chhotaray, P. K.; Nesterov, E. E.; Warner, I. M. Influence of anion variations on morphological, spectral, and physical properties of the propidium luminophore. *Journal of Physical Chemistry A* **2019**, *123*, 111-119. It is reproduced by permission of the American Chemical Society.
https://pubs.acs.org/doi/10.1021/acs.jpca.8b06948

solar cells (DSSCs) applications,[12] and carbazole GUMBOS for OLED applications.[13] Herein, we report efforts toward tuning photothermal stability and solid-state morphology of the propidium luminophore simply by counteranion variation with the expectation of expanding the range of applications for the propidium luminophore in both solution and solid states.

Materials that are amorphous or have a low degree of crystallinity are preferred over highly crystalline compounds for use in optoelectronics and other related solid-state applications. This is because crystalline structures would often undesirably influence solid-state characteristics such as nonlinear optical activity, photothermal reactivity, and conductivity.[13,14] Optimization of solid-state molecular arrangements to reduce the degree of crystallinity is often achieved by inclusion of host materials, attachment of substituents, and use of polymorphism.[15-17] In addition, designing organic salts with appropriate combinations of cationic and anionic moieties to adjust solid-state molecular arrangements by optimizing electrostatic attractions as well as steric hindrance is also regarded as a simple, economical, and time-saving approach for ionic species.[18,19]

Variations in counteranions can generally produce modifications of physical and chemical properties of organic salts including solubility,[9] photothermal stability,[13,20] molecular motion,[21] magnetic behavior,[22] as well as spectral characteristics[23,24] such as absorption, photoluminescence, quantum yield, and lifetimes. In particular, [NTf_2] and [BETI] counteranions are known to enhance the photostability of luminophores.[13,20] According to single-molecule experiments, it is revealed that photobleaching usually takes place by light-induced oxidation of molecules, which affects the emission of the luminophore reversibly or irreversibly.[25] Although the mechanisms involved in photobleaching are not fully realized and specific for a given molecule, it is also reported that radical dark states might be involved in the photobleaching mechanisms.[26] These photobleaching mechanisms are likely perturbed by certain counterions as has been reported in previous

studies.[12,13,20] Thermal stability of organic salts depends on many factors including charge density, chain length, and functional groups of both anions and cations. In particular, the characteristics of the counterion such as nucleophilicity, shape, coordinating nature, and hydrophobicity. Therefore, counterions typically play an important role in determining the thermal stability of the organic salts.[13,27]

Anion variations are known to have variable influences on spectral and electrochemical characteristics of luminophores.[9-13,18,19] In the present study, we have found that [NTf_2] and [BETI] counteranions facilitate improved solubility of propidium luminophore in relatively less polar solvents such as ethyl acetate, THF, and DCM. According to fluorescence lifetime experiments, the excited state of the propidium luminophore is stabilized in relatively less polar solvents as indicated by longer fluorescence lifetimes. As a result, photoluminescence quantum yield was substantially higher in these relatively less polar solvents, possibly due to hindering nonradiative relaxation to the ground state by energy transfer, internal conversion, and intersystem crossing.[28,29] The propidium luminophore has a predominant red photoluminescence from S_1 emission as well as a weak photoluminescence in the deep blue region of the electromagnetic spectrum (EMS) resulting from S_2 emission in selected solvents (which was confirmed using a computational study). We note that S_2 emission is a rare phenomenon since Kasha's rule requires photon emission to occur from the lowest excited state of a given fluorophore.[30] This property of propidium fluorophores could be attributed to a higher than normal energy gap between the first two excited singlet states of the propidium moiety. Electronic properties of [P][I] and PGUMBOS show similar trends, with the highest occupied molecular orbital (HOMO) and lowest unoccupied molecular orbital (LUMO) energies in the range of -5.2 (±0.1) and -3.2 (±0.1) eV, as well as HOMO-LUMO energy gap at approximately 1.96 eV, confirming that these materials can act as organic

semiconductors. Therefore, PGUMBOS evaluated in this study can be potentially useful in organic light-emitting diodes (OLEDs), solar cells, smart materials, and sensors.

4.2. Experimental Section

4.2.1. Materials

The compound, [P][I], was purchased from Biotium Inc. (Fremont, CA) and [Li][NTf_2], [Na][TfO], $TBAPF_6$, and Fc were purchased from Sigma-Aldrich (St. Louis, MO). [Li][BETI] was purchased from IoLiTech Inc. (Tuscaloosa, AL). The solvents, EA, DMSO, DMF, MeOH, THF, DCM, and ACN were purchased from Macron (Center Valley, PA). Deionized water was obtained using an Elga PURELAB ultra water-filtration system (Neobits Inc., CA). All solvents were analytical grade with no stabilizers and all chemicals were used as received without further purification.

4.2.2. Instrumentation

A Panalytical Empyrean multipurpose diffractometer (Westborough, MA) with a copper anode was used for PXRD experiments. A Hi Res Modulated TGA 2950 thermogravimetric analyzer (TA Instruments, New Castle, DE) was used to obtain thermogravimetric profiles. Photoluminescence spectra were recorded using a HORIBA Spex Fluorolog-3-spectrofluorometer (model FL3-22TAU3, Jobin-Yvon, Edison, NJ) with a 0.4 cm path length quartz cuvette (Starna Cells) and connected to an integrating sphere (HORIBA Petite Integration Sphere, Jobin-Yvon, Edison, NJ) when absolute quantum yields were measured. The same fluorometer was used for photostability experiments with the entrance slit width maintained at 14 nm. All UV–vis absorbance spectra were obtained using a UV-3101PC scanning spectrophotometer (Shimadzu, Columbia, MD) with a 1 cm path length quartz cuvette (Starna Cells) against an identical cuvette filled with solvent as a blank. Fluorescence lifetime experiments were performed using a HORIBA

FluoroMax plus fluorometer with pulsed light source Delta Diodes (294 nm, pulse width 800 ps; 481 nm, pulse width 80 ps) and a PPD-850 detector with transit time spread ~180 ps (Horiba Scientific, NJ). All CV experiments were performed at room temperature using an Autolab PGSTAT 302 potentiostat (Metrohm, Riverside, FL) with a three-electrode system: a platinum disk working electrode, a $Ag/AgNO_3$ nonaqueous reference electrode, and a Pt wire counterelectrode (CH Instruments, Austin, TX). The reference electrode was checked against the ferrocene/ferrocenium (Fc/Fc^+) couple as the standard before and after each CV experiment and the potentials were quoted relative to the Fc/Fc^+ redox couple (scan rate of 0.1 V/s within the potential range of -1.5 to +1.3 V). [P][I] and PGUMBOS were dissolved in degassed $TBAPF_6$ solutions (0.1 M, supporting electrolyte) prepared in DCM or ACN to obtain a final concentration of 1 mM.

4.3. Synthesis and Characterization

All PGUMBOS were synthesized using a simple, one-step metathesis reactions between [P][I] and the respective Li/Na salts of [BETI], [NTf_2], and [TfO] as previously reported, as showed in Figure 4.1.[9-13] Synthesis of [P][BETI] is described here as a representative protocol for preparation of all PGUMBOS. First, the starting material, [P][I] (50 mg, 0.075 mmol), was completely dissolved into 75 mL of DI water in a 500 mL round bottom flask. Then, [Li][BETI] (58 mg, 0.15 mmol) was added to the aqueous [P][I] solution in the round-bottom flask and stirred for approximately 5 min until [Li][BETI] was completely dissolved. Then, DCM (300 mL) was gradually added to the aqueous [P][I] and [Li][BETI] solution. Once DCM was added, the resultant biphasic solution was stirred vigorously for approximately 6 h at room temperature. Then, this biphasic solution was transferred to a separatory funnel and the bottom organic layer was carefully siphoned into a separate container. The extracted organic layer was washed three times with DI

water (200 mL × 3) to remove traces of the byproduct, [Li][I], which is water soluble. Then, anhydrous magnesium sulfate was added to the DCM layer to remove trace amounts of water from the organic layer, followed by suction filtration to remove magnesium sulfate particles. The dried and filtered organic layer was vacuum evaporated to remove DCM. The resultant product, [P][BETI], was freeze -dried and obtained as a maroon color solid (81 ±5 mg, yield 92 ±6%). Syntheses of [P][NTf_2] and [P][TfO] were similarly performed and are detailed in Appendix C. PGUMBOS were characterized using ^{13}C NMR, ^{1}H NMR, (Bruker Avance 400), and ^{19}F NMR (Bruker Avance 500) as well as ESI-MS (Agilent 6210 ESI-TOF) with data presented in Appendix C.

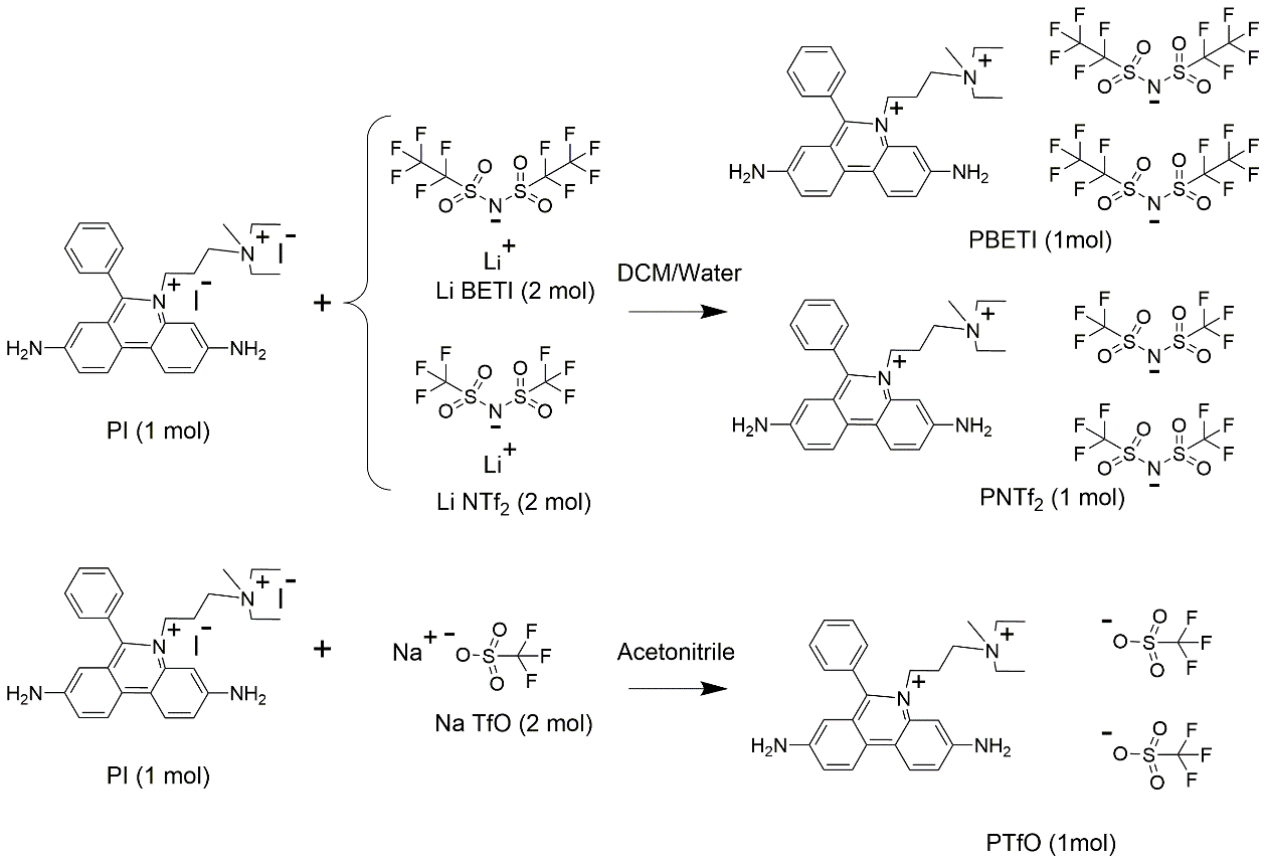

Figure 4.1. Synthesis scheme of PGUMBOS.

4.4. Results and Discussion

4.4.1. Morphology of PGUMBOS

Solid-state morphologies of [P][I] and PGUMBOS were elucidated using PXRD (Figure C1 in Appendix C), which confirmed the high crystallinity of [P][I] and [P][TfO] as denoted by clusters of sharp peaks. Since [I] and [TfO] are relatively small anions with less steric hindrance, [P][I] and [P][TfO] allowed effective packing in the solid-state, resulting in high crystallinity. In contrast, the significantly lower crystallinity exhibited by [P][BETI] and [P][NTf_2] as reflected from a few broad peaks in PXRD is attributed to reduced packing efficiency of [P][BETI] and [P][NTf_2] in the solid-state, as a result of steric hindrance caused by bulky [BETI] and [NTf_2] counteranions. These counterions, [BETI] and [NTf_2], were shown to produce similar effects on the solid-state morphology of a carbazole based cationic luminophore in the previous studies from our laboratory.[13] Counteranion dependent optimization of luminophore morphology is the simplest method for avoiding undesirable optical, electrical, and physical phenomena arising from crystallinity, which is extremely important for solid-state applications.[13,14]

4.4.2. Photothermal Stability

The effect of anion variation on photothermal stability was evaluated using TGA and time-dependent kinetic photoluminescence methods. TGA experiments were conducted within the temperature range of 25-600 °C at a rate of 10 °C/min using heating materials (< 5 mg) placed in aluminum pans under a nitrogen purge. The onset of weight loss (< 5%) due to thermal degradation was determined using a step-tangent method, denoted as T_{onset}, which is used to measure the thermal stability of the materials.[27] The resultant TGA profiles of [P][I] and PGUMBOS are displayed in Figure 4.2 and T_{onset} values are listed in Table 4.1. Also, TGA profiles of [Li][BETI], [Li][NTf_2], and [Na][TfO] were presented in Figure 2 in Appendix C. The thermal stability of an

ionic organic compound depends on the characteristics of the cation as well as the anion. These characteristics include size, shape, the extent of resonance stabilization, charge density, nucleophilicity/nucleophobicity, and functional groups. The influences of these factors on thermal stability of ionic liquids are well investigated and cited in the literature, and are relevant here. The outcomes of these studies are also applicable to solid-state ionic compounds such as PGUMBOS.[31,32] The thermal stability trend of [P][I] and PGUMBOS were determined to be in the following order: [P][BETI] ≥ [P][NTf_2] > [P][I] ≥ [P][TfO]. Halides are known to significantly reduce thermal stability of ionic compounds since halides possess relatively high nucleophilic and basic properties. As a result, iodide ions in [P][I] are more nucleophilic than [BETI], [NTf_2], and [TfO] anions and thus induce S_N1 or S_N2 nucleophilic decomposition of [P][I], resulting in the lowest thermal stability observed for the compounds investigated.[31-34]

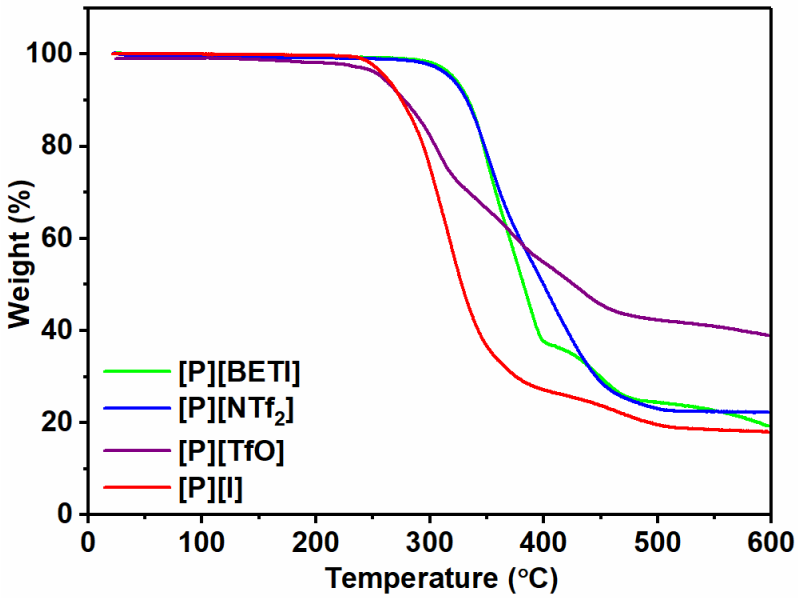

Figure 4.2. TGA profiles of [P][I] and PGUMBOS.

Among the variety of interactions that exist between the cationic and anionic species, electrostatic attractions are the strongest, which is determined by shape and charge delocalization of the associated ions. The thermal stability trend observed for Li/Na salts, [Li][BETI] > [Li][NTf_2]

> [Na][TfO], can be explained by use of electrostatic interactions (Figure C2 in Appendix C). In order to understand the thermal stability trends observed for PGUMBOS, it is important to remember that electrostatic interactions are much weaker in PGUMBOS than in Li/Na salts. The result is a significantly lower charge density on the bulky propidium cation. As a result, decomposition of PGUMBOS occurs at relatively lower temperatures as compared to Li/Na salt decomposition of the same set of anions. For example, T_{onset} of [Li][BETI] was 364 °C whereas T_{onset} of [P][BETI] was 327 °C. Thermal stabilities of PGUMBOS are influenced by numerous anion characteristics (since the cation is the same for all three compounds) including the extent of resonance stabilization, nucleophilicity, size, and shape of the anions. Noticeably, [TfO] has a negative charge on oxygens, whereas [BETI] and [NTf_2] have negative charges on N atoms. In addition, the negative charge of [TfO] is highly stabilized as compared to that of [BETI] and [NTf_2] (which is also reflected in the fact that [TfO] is one of the best leaving groups in organic chemistry).[35] Therefore, [P][TfO] exhibited the lowest thermal stability among PGUMBOS. The T_{onset} values of [P][BETI] and [P][NTf_2] are very close as a result of more or less similar characteristics of these two anions including size, shape, functional groups, nucleophilicity, and interactions with the cation. The TGA profiles of PGUMBOS showed few distinguishable decomposition steps during the thermal degradation process with multiple inflection points (Figure C3 in Appendix C). These multistep thermal decompositions are likely due to formation of intermediate degradation products formed during the thermal degradation process.

Table 4.1. Onset of decomposition (T_{onset}) and percentage photobleaching in DCM for [P][I] and PGUMBOS.

Compound	T_{onset} (°C)	Photobleaching (%)
[P][BETI]	327	1
[P][NTf_2]	323	1
[P][TfO]	271	2
[P][I]	273	6
[Ru (Phen)]	N/A	93

It should be noted that the performance of luminophores is often compromised by photo-induced changes.[36,37] Therefore, photostabilities of [P][I] and PGUMBOS were evaluated using a previously reported protocol with small modifications.[13,20,38] In a typical experiment, the PGUMBOS compound was dissolved in DMF at 50 °C to produce a concentrated solution (0.1 M) and this solution was used as the bulk solution to prepare [P][I] and PGUMBOS solutions in DCM (0.5 mM). These solutions were intensively irradiated with monochromatic light at the absorption maximum of the compound for 3000 consecutive seconds, while recording the photoluminescence intensity fluctuations at the wavelength of the emission maximum. The decrease in emission intensity observed with increasing irradiation time was deemed to be proportional to the extent of photobleaching. The experimental conditions for photostability experiments including solvent system, irradiation time, and concentration of the analyte were optimized by testing a readily photobleachable red fluorescent dye, dichlorotris(1,10-phenanthroline)ruthenium(II) hydrate [Ru(Phen)], using different experimental conditions, and choosing the conditions in which [Ru(Phen)] was near complete photobleached (93%) as shown in Figure 4.3. The extent of photobleaching of a compound was then calculated using Equation 4.1.

$$Photobleaching\ (\%) = \left(1 - \frac{I}{I_0}\right) \times\ 100\ \% \qquad , \qquad (4.1)$$

where I is the emission intensity after 3000 s and I_0 is the observed emission intensity prior to irradiation. Under these experimental conditions, [P][I] displayed approximately 6 % photobleaching, and PGUMBOS showed a substantially improved photostability as compared to that of [P][I]. [P][BETI] and [P][NTf_2] showed only 1% photobleaching, whereas [P][TfO] showed 2% photobleaching. Photobleaching data are summarized in Table 4.1. A similar counterion dependent improvement in photostability was also observed for cyanine GUMBOS with [NTf_2], as well as carbazole GUMBOS with [BETI] as counteranions in previous studies.[13,20]

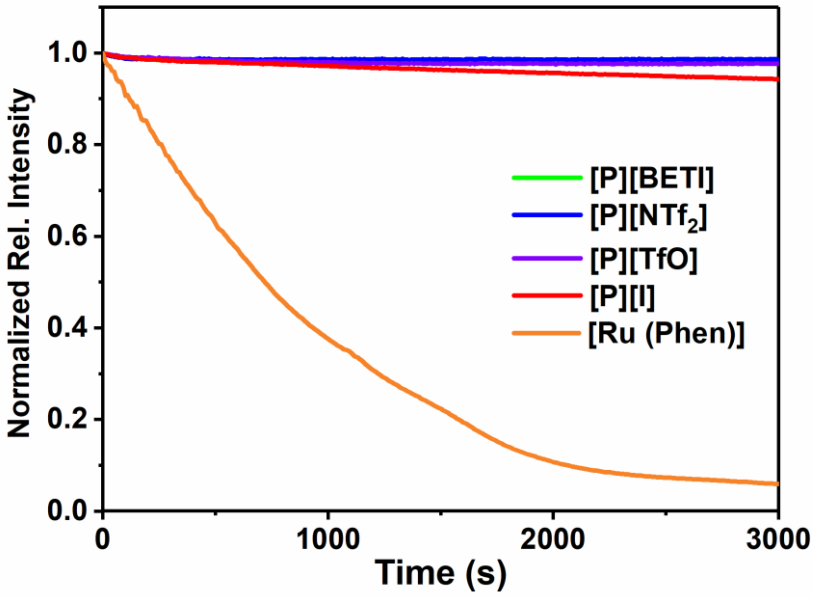

Figure 4.3. Time-dependent relative photoluminescence intensity of [P][I] and PGUMBOS over a time period of 3000 s.

4.4.3. Spectral Properties in Solution and Solid States

Figure 4.4 displays normalized UV-vis absorption spectra of [P][I] and PGUMBOS in methanol solution (10 µM) with a summary of absorption characteristics presented in Table 4.2. All compounds exhibited analogous absorption profiles with two sets of bands (A_1 and A_2) with absorption maxima (A_{max}) at 535 ±3 and 296 nm, respectively. Molar extinction coefficients (ε) of these compounds were found to be comparable (Table 4.2).

Table 4.2. Absorption maxima (A_{max}), FWHM, molar extinction coefficients (ε) in methanol for [P][I] and PGUMBOS.

Compound	A_{max} (nm)	FWHM (nm)	ε (10^3 $M^{-1}cm^{-1}$)
[P][BETI]	296,535	30,95	6.0
[P][NTf_2]	296,532	30,94	6.1
[P][TfO]	296,536	30.91	6.1
[P][I]	296,535	30,97	5.8

The A_1 peaks were observed to be much weaker and wider, with a FWHM value of 94 ±3 nm as compared to the A_2 peaks, which were much more intense and narrower (FWHM of 30 ±1 nm). Absorption spectra of [P][I] and PGUMBOS were recorded in several solvents with different

polarities and a significant blue shift was observed for [P][TfO] and [P][I] in water, suggesting the excited state to be relatively less polar than the ground state (Figure C4 in Appendix C).

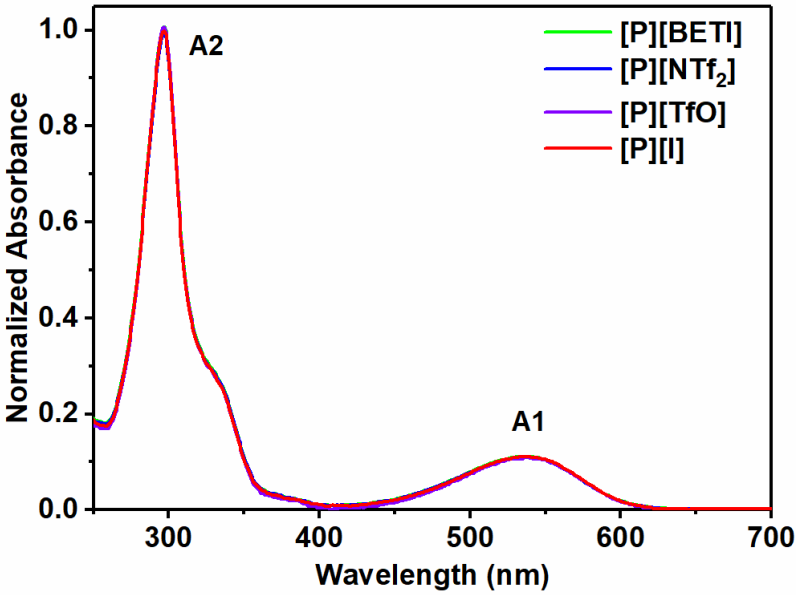

Figure 4.4. Normalized absorbance of [P][I] and PGUMBOS in methanol solution (10 µM).

The photoluminescence spectra of these compounds were also recorded in methanol solution (5 µM) using separate excitations at absorption maxima of both A_1 and A_2 peaks (A_{max1} and A_{max2}). The resultant photoluminescence spectra are shown in Figure 4.5.

Table 4.3. Emission maxima and full widths at half -maxima (FWHM) for [P][I] and PGUMBOS in methanol.

Compound	λ_{max1} (nm)	$FWHM_1$ (nm)	λ_{max2} (nm)	$FWHM_2$ (nm)
[P][BETI]	632	93	410	73
[P][NTf_2]	632	93	413	73
[P][TfO]	631	93	408	73
[P][I]	632	93	410	72

In addition, a summary of emission characteristics is provided in Table 4.3. When excited at A_{max1}, all compounds showed comparable S_1 emissions in the orange-red region of the EMS with the emission maxima (λ_{max1}) at approximately 630 ±2 nm (Figure 4.5A). When excited at A_{max2}, all compounds showed a weak S_2 emission in the violet-blue region of the EMS with the emission

maxima (λ_{max2}) at 410 ±3 nm, as well as a strong S_1 emission with the emission maxima at 630 ±4 nm (Figure 4.5B).

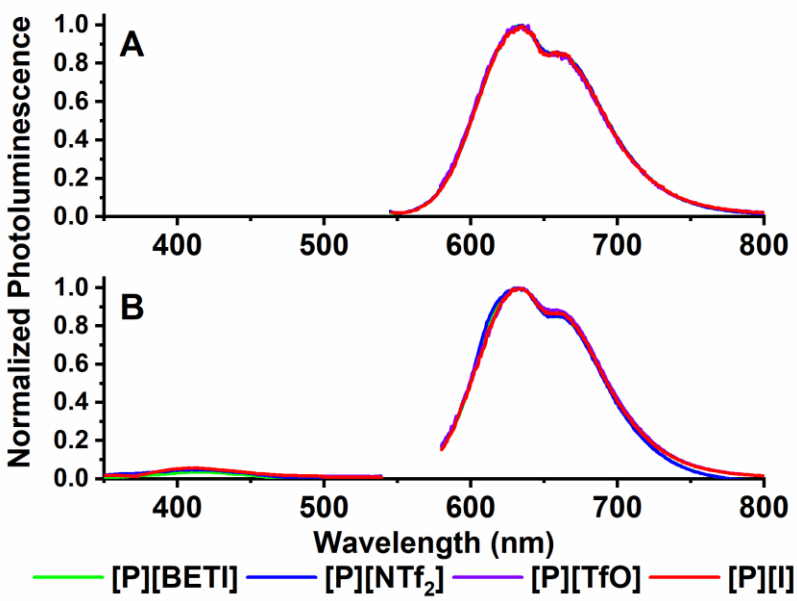

Figure 4.5. Normalized photoluminescence spectra of [P][I] and PGUMBOS in methanol solution (5 µM) when excited at A_{max1} (A) and A_{max2} (B) wavelengths.

Photoluminescence spectra of [P][I] and PGUMBOS were obtained in different solvents and are displayed in Figures C5 and C6 in Appendix C. Except for DCM, where [P][BETI] and [P][NTf_2] showed no detectable S_2 emission, [P][I] and PGUMBOS showed both S_1 and S_2 emissions when excited at A_{max2} in polar solvents such as ACN, THF, and water. Also, normalized absorption and excitation spectra of [P][BETI] in methanol solution are displayed in Figures C7 and C8 in Appendix C to further understand the spectral properties of PGUMBOS. Excitation spectra of [P][BETI] relevant to S_1 and S_2 emissions are presented in Figures C7 and C8 provided important insights into the electron distribution of the ground -state [P][BETI] molecule. Since excitation spectra found analogues to A_1 and A_2 bands of the absorption spectrum of [P][BETI], existence of both S_1 and S_2 emissions were experimentally confirmed and further supported by computational studies.

Solid films of [P][I] and PGUMBOS were prepared by electrodeposition of these compounds (from a 1 mM MeOH solution) on precleaned quartz slides followed by drying in ambient conditions overnight. Absorption and photoluminescence spectra of [P][BETI] thin films are presented in Figure 4.6. It is noted that the solid-state absorbance of [P][BETI] shows characteristics similar to those observed in the solution state, i.e., a strong peak with an absorption maximum ($A_{max2'}$) at 298 nm and a weaker peak with an absorption maximum ($A_{max1'}$) at 533 nm. The FWHM values of $A_{max1'}$ and $A_{max2'}$ were 95 and 179 nm, implying significant peak broadening as compared to the solution state values. The solid-state photoluminescence spectrum of [P][BETI] showed only an S_1 emission with a peak maximum at 636 nm and a slight red shift (5 nm) as compared to the solution state spectrum. The observed spectral broadening and red shifting of absorption peaks can be attributed to molecular aggregation in the solid-state.[39,40]

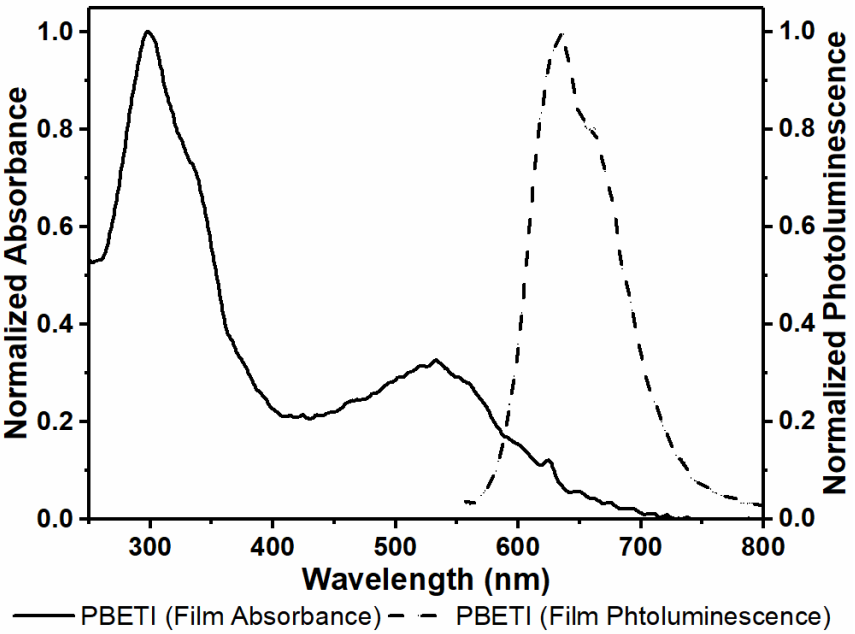

Figure 4.6. Normalized absorption and photoluminescence spectra of [P][BETI] solid film.

4.4.4. Lifetimes and PLQY

Measurement of the excited -state lifetime of a fluorophore provides both qualitative and quantitative information including quantum yields, polarization, and radiative energy transfer

processes.[28] For this reason, the fluorescence lifetimes of [P][I] and PGUMBOS were measured at 620 nm (near S_1 emission maxima of compounds) with excitation at 481 nm (near A_1 absorption maxima of compounds) in selected solvents with different polarities. Figure C8 in Appendix C displays fluorescence intensity decay curves and Table 4.4 lists the estimated lifetimes in each solvent. Lifetimes of [P][I] and PGUMBOS were found to be in the range from approximately 1 ns (water) to 8 ns (DCM). All curves were easily fit to monoexponential decays, indicating that emissions occurred from relatively pure compounds in the singlet excited state. Noticeably, lifetimes of [P][I] and PGUMBOS showed a strong solvent dependence as denoted by a systematic decrease of lifetimes with increasing polarity of solvents. This observation is likely a result of the excited state of propidium luminophore being relatively nonpolar as compared to the ground state of the propidium luminophore, which results in better stability in nonpolar solvents. As a result, nonradiative decay pathways such as energy transfer, internal conversion, and intersystem crossing were less favored in nonpolar media as indicated by substantial increases in photoluminescence quantum yields in nonpolar solvents (Table 4.4).[28,29]

Absolute quantum yields of [P][I] and PGUMBOS were determined using an integrating sphere for S_1 emission in the same set of solvents that were used for lifetime measurements.[41] The resulting quantum yield data are displayed in Table 4.4. [P][I] and [P][TfO] showed a systematic decrease in quantum yields with increasing solvent polarity. Maximum quantum yields for [P][I] and [P][TfO] (5 ±1%) were recorded in methanol. In the case of [P][BETI] and [P][NTf_2], the quantum yields were found to be essentially the same in DCM, THF, and EA with an average quantum yield of 21 ±2% and 18 ±1% for [P][NTf_2] (Table 4.4). The observed high quantum yields for PGUMBOS in relatively less polar solvents (such as DCM, THF, and EA, in which polarity indices are distributed in a narrow range of 3.1-4.4) as compared to those in the more polar solvents

(MeOH, DMSO, and water with polarity indices in the range of 5.1-9.0) used in this study are supported by the fluorescence lifetime data.[42] On the basis of these quantum yield and lifetime data, we contend that the bulky, hydrophobic [BETI] and [NTf_2] counteranions play a significant role in improving quantum yields of [P][BETI] and [P][NTf_2] through solubilization of the propidium fluorophore in less polar solvents. Furthermore, the bulky, hydrophobic [BETI] and [NTf_2] counteranions may contribute to stabilization of the excited state species by providing a hydrophobic environment analogous to that of previously reported significant quantum yield enhancements for [P][I] upon binding to nucleic acids with relatively hydrophobic cores.[43]

Table 4.4. Fluorescence lifetime and PLQY data for [P][I] and PGUMBOS in different solvents.

Compound		DCM	THF	EA	MeOH	DMSO	Water
[P][BETI]	Lifetime (ns)	7.72	4.86	5.78	3.07	-	-
	QY (%)	22.8 (±1.2)	21.3 (±1.8)	21.5 (±1.7)	5.6 (±0.6)	-	-
[P][NTf_2]	Lifetime (ns)	8.26	4.95	5.90	3.16	-	-
	QY (%)	18.8 (±2.0)	18.8 (±0.6)	17.8 (±1.5)	5.6 (±0.3)	-	-
[P][TfO]	Lifetime (ns)	-	-	-	3.00	2.82	0.96
	QY (%)	-	-	-	5.9 (±0.5)	5.5 (±0.4)	1.5 (±0.2)
[P][I]	Lifetime (ns)	-	-	-	3.04	2.79	0.96
	QY (%)	-	-	-	5.2 (±0.1)	5.6 (±0.5)	1.9 (±0.1)

4.4.5. Electrochemical Properties

CV and UV-vis absorption spectra were employed for estimating experimental HOMO, LUMO, and HOMO-LUMO energy gap (E_g) energies of [P][I] and PGUMBOS. The cyclic voltammograms obtained for [P][I] and PGUMBOS are shown in Figure C10 in Appendix C, and a summary of the electronic properties is provided in Table 4.5. From the CV data, the onset oxidation values ($E_{ox.}$) were estimated against the Fc/Fc^+ redox potential. Also, long-wavelength onset values of the absorption spectra (λ_{edge}) were used to estimate energy gaps of the compounds.

Equations 4.2 and 4.3 were employed to calculate energies of HOMO, LUMO, and E_g of compounds.[44]

$$HOMO = -1e\,[E_{ox.} + 4.71]eV \quad (4.2)$$

$$Eg = (E_{HOMO} - E_{LUMO}) = \left(\frac{hc}{\lambda_{edge}}\right) = \left(\frac{1240}{\lambda_{edge}}\right)eV \quad (4.3)$$

Calculated experimental HOMO and LUMO energies of the PGUMBOS were in the range of - (5.1 ±0.1) eV to - (3.1 ±0.3) eV. In the case of [P][I], additional oxidation peaks were observed and were attributed to the oxidation of [I].[45] Optical energy gaps were calculated using absorption spectra of [P][I] and [P][BETI] and found to be 1.96 eV, which is within the typical energy gap range (0-4 eV) of organic semiconducting materials.[46]

Table 4.5. Experimental HOHO-LUMO energies and energy gaps of [P][I] and PGUMBOS.

Compound	Energy Gap (eV)	HOMO (eV)	LUMO (eV)
[P][BETI]	1.96	-5.10	-3.14
[P][NTf_2]	1.96	-5.12	-3.16
[P][TfO]	1.96	-5.12	-3.16
[P][I]	1.96	-5.27	-3.31

4.4.6. Computational Studies

In order to confirm structural and electronic assignments obtained in spectroscopic and electrochemical studies, computational analysis was performed using the time-dependent density functional theory (DFT) approach at the B3LYP/6-31+G(d,p) level of theory. The DFT approach is widely used to accurately model small to medium size organic compounds and has been previously used by our group to characterize heteroaromatic carbazole derivatives.[13] To better adjust for the polar medium of the ionic solids, computations on the propidium cation was performed using a polarizable conductor calculation model (CPCM) for the highly polar solvent DMSO. The CPCM model applies a solvent field to account for potential dispersion effects and polarization, which also provide some cation stabilization in the solid-state.[47,48] This computational

study produced an energy gap value of 2.39 eV, which is in reasonable agreement with the experimental values estimated from UV-vis absorption spectra (Table 4.5). Furthermore, the computed long-wavelength absorption band maximum (519 nm) agreed well with the experimental value for the band A_1 (535 nm, Figure 4.5). These computations indicated that this absorption band was primarily due to the HOMO→LUMO electronic transition, with both frontier molecular orbitals spatially distributed over the three-ring benzoquinolinium aromatic fragment (Figure 4.7). The colocalization of the frontier molecular orbitals over the benzoquinolinium fragment might be at least partially responsible for the invariance of the optical properties with respect to the counteranions. In contrast, the higher energy absorption band A_2 originated from two primary configurations, HOMO-1→LUMO, and HOMO-2→LUMO, one of which (HOMO-2) was spatially delocalized over both benzoquinolinium and phenyl rings (Figure 4.7), which could make it sensitive to torsional twisting of the phenyl ring, and therefore to molecular packing in the solid-state.

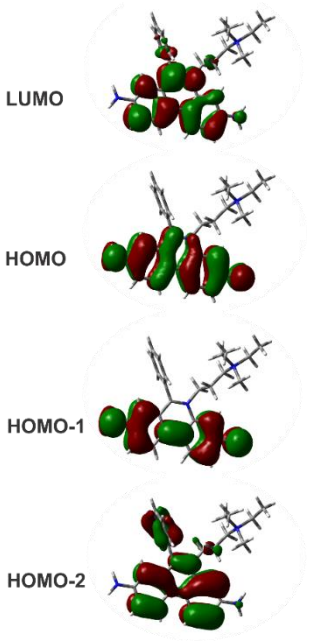

Figure 4.7. Calculated distributions of molecular orbitals near the energy gap for the propidium luminophore.

4.5. Conclusions

A series of novel solid-state organic salts derived from PGUMBOS were successfully synthesized, and physical characteristics such as solubility, crystallinity, photothermal stability, electrochemistry, and spectroscopy including absorption, photoluminescence, quantum yields, and lifetimes of these compounds were systematically investigated. The parent compound, [P][I], and the novel synthesized compound, [P][TfO], showed similar characteristics such as a high degree of crystallinity, solubility in relatively polar solvents including water, and similar thermal stabilities. In contrast, [P][BETI] and [P][NTf_2] with the bulkier and more hydrophobic counteranions exhibited substantially lower crystallinity, better solubility in less polar solvents, and high thermal stability relative to [P][I]. All PGUMBOS materials showed high stability with regard to photothermal degradation. Interestingly, PGUMBOS showed two absorption peaks and a single broad photoluminescence peak in the red region of the EMS. In some solvents, a weak S_2 emission in the deep blue region was also observed for PGUMBOS. Quantum yields and lifetime measurements of [P][I] and PGUMBOS showed a strong dependence on solvent polarity. The counteranions, [BETI] and [NTf_2], played an important role in increasing the lifetime and quantum yield by allowing solubilization of propidium luminophore in less polar solvents and thus providing a more hydrophobic environment. These novel PGUMBOS materials were organic semiconductors with electronic properties suitable for a variety of optoelectronic applications. Future studies of these compounds will include preparation and evaluation of electroluminescent devices with these materials as emissive layers.

4.6. References

1. Riccardi, C.; Nicoletti, I. Analysis of apoptosis by propidium iodide staining and flow cytometry. *Nature Protocols* **2006**, *1*, 1458-1461.

2. Pietkiewicz, S.; Schmidt, J. H.; Lavrik, I. N. Quantification of apoptosis and necroptosis at the single cell level by a combination of imaging flow cytometry with classical annexin V/propidium iodide staining. *Journal of Immunological. Methods* **2015**, *423*, 99-103.

3. Nicoletti, I.; Migliorati, G.; Pagliacci, M. C.; Grignani, F.; Riccardi, C. A rapid and simple method for measuring thymocyte apoptosis by propidium iodide staining and flow cytometry. *Journal of Immunological Methods* **1991**, *139*, 271-279.

4. Belloc, F.; Dumain, P.; Boisseau, M. R.; Jalloustre, C.; Reiffers, J.; Bernard, P.; Lacombe, F. A flow cytometric method using hoechst 33342 and propidium iodide for simultaneous cell cycle analysis and apoptosis determination in unfixed cells. *Cytometry* **1994**, *17*, 59-65.

5. Hezel, M.; Ebrahimi, F.; Koch, M.; Dehghani, F. Propidium iodide staining: A new application in fluorescence microscopy for analysis of cytoarchitecture in adult and developing rodent brain. *Micron* **2012**, *43*, 1031-1038.

6. Happ, D. F.; Tasker, R. A. A method for objectively quantifying propidium iodide exclusion in organotypic hippocampal slice cultures. *Journal of Neuroscience Methods* **2016**, *269*, 1-5.

7. Eilam, T.; Bushnell, W. R.; Anikster, Y.; McLaughlin, D. J. Nuclear DNA content of basidiosphores of selected rust fungi as estimated from fluorescence of propidium iodide-stained nuclei. *Phytopathology* **1992**, *82*, 705-712.

8. Warner, I. M.; El-Zahab, B.; Siraj, N. Perspectives on moving ionic liquid chemistry into the solid phase. *Analytical Chemistry* **2014,** *86*, 7184-7191.

9. Magut, P. K. S.; Das, S.; Fernand, V. E.; Losso, J. ; McDonough, K.; Naylor, B. M.; Aggarwal, S.; Warner, I. M. Tunable cytotoxicity of rhodamine 6G via anion variations. *Journal of the American Chemical Society* **2013**, *135*, 15873-15879.

10. Al Ghafly, H.; Siraj, N.; Das, S.; Regmi, B. P.; Magut, P. K. S.; Galpothdeniya, W. I. S.; Murray, K. K.; Warner, I. M. GUMBOS matrices of variable hydrophobicity for matrix-assisted laser desorption/ionization mass spectrometry. *Rapid Communications in Mass Spectrometry* **2014**, *28*, 2307-2314.

11. Regmi, B. P.; Galpothdeniya, W. I. S.; Siraj, N.; Webb, M. H.; Speller, N. C.; Warner, I. M. Phthalocyanine- and porphyrin-based GUMBOS for rapid and sensitive detection of organic vapors. *Sensors and Actuators B: Chemical* **2015,** *209*, 172-179.

12. Jordan, A. N.; Das, S.; Siraj, N.; de Rooy, S. L.; Li, M.: El-Zahab, B.; Chandler, L.; Baker, G. A.; Warner, I. M. Anion-controlled morphologies and spectral features of cyanine-based nanoGUMBOS- an improved photosensitizer. *Nanoscale* **2012**, *4*, 5031-5038.

13. Siraj, N.; Hassan, F.; Das, S.; Kiruri, L.; Steege Gall, K. E.; Baker, G. A.; Warner, I. M. Carbazole-derived group of uniform materials based on organic salts: solid state fluorescent analogues of ionic liquids for potential applications in organic-based blue light-emitting diodes. *Journal of Physical Chemistry C* **2014**, *118*, 2312-2320.

14. Moorthi, J. N.; Venkatakrishnan, P.; Natarajan, P.; Huang, D.-F.; Chow, T. J. De novo design for functional amorphous materials: synthesis and thermal and light-emitting properties of twisted anthracene-functionalized bimesitylenes. *Journal of the American Chemical Society* **2008**, *130*, 17320-17333.

15. Ooyama, Y.; Yoshida, K. Heterocyclic quinol-type fluorophores. Dramatic solid-state fluorescence enhancement behavior of imidazoanthraquinol-type clathrate hosts upon inclusion of various kinds of organic solvent molecules. *New Journal of Chemistry* **2005**, *29*, 1204-1212.

16. Ooyama, Y.; Harima, Y. Dramatic effects of the substituents on the solid-state fluorescence properties of structural isomers of novel benzofuro[2,3-c]oxazolocarbazole-type fluorophores. *Chemistry Letters* **2006**, *35*, 902-903.

17. Mutai, T.; Satou, H.; Araki, K. Reproducible on-off switching of solid-state luminescence by controlling molecular packing through heat-mode interconversion. *Nature Materials* **2005**, *4*, 685-687.

18. Zhang, G.; Zhang, H.; Kong, L.; Wang, S.; Tian, Y.; Tao, X.; Yang, J. Anion-controlled dimer distance induced unique solid-state fluorescence of cyano substituted styrene pyridinium. *Scientific Reports* **2016**, *6*, 37609.

19. Hinoue, T.; Shigenoi, Y.; Sugino, M.; Mizobe, Y.; Hisaki, I.; Miyata, M.; Tohnai, N. Regulation of π-stacked anthracene arrangement for fluorescence modulation of organic solid from monomer to excited oligomer emission. *Chemistry: A European Journal* **2012**, *18*, 4634-4643.

20. Lu, C.; Das, S.; Magut, P. K. S.; Li, M.; El-Zahab, B.; Warner, I. M. Irradiation induced fluorescence enhancement in PEGylated cyanine-based NIR nano- and mesoscale GUMBOS. *Langmuir* **2012**, *28*, 14415-14423.

21. Leontiev, A. V.; Serpell, C. J.; White, N. G.; Beer, P. D. Cation-induced molecular motion of spring-like [2]catenanes. *Chemical Science* **2011**, *2*, 922-927.

22. Del Sesto, R. E.; McCleskey, T. M.; Burrell, A. K.; Baker, G. A.; Thompson, J. D.; Scott, B. L.; Wilkes, J. S., Williams, P. Structure and magnetic behavior of transition metal based ionic liquids. *Chemical Communications* **2008**, *0*, 447-449.

23. Das, S.; Bwambok, D.; El-Zahab, B; Monk, J.; de Rooy, S. L.; Challa, S.; Li, M.; Hung, F. R.; Baker, G. A.; Warner, I. M. Nontemplated approach to tuning the spectral properties of cyanine-based fluorescent nanoGUMBOS. *Langmuir* **2010**, *26*, 12867-12876.

24. Jordan, A. N.; Siraj, N.; Das, S.; Warner, I. M. Tunable near-infrared emission of binary nano- and mesoscale GUMBOS. *RSC Advances* **2014**, *4*, 28471-28480.

25. Christ, T.; Kulzer, F.; Bordat, P.; Basche, T. Watching the photo-oxidation of a single aromatic hydrocarbon molecule. *Angewandte Chemie International Edition* **2001**, *40*, 4192-4195.

26. Hoogenboom, J. P.; van Dijk, E. M.; Hernando, J.; van Hulst, N. F.; Garcia-Parajo, M. F. Power-law-distributed dark states are the main pathway for photobleaching of single organic molecules. *Physical Review Letters* **2005**, *95*, 097401.

27. Eshetu, G. G.; Jeong, S.; Pandard, P.; Lecocq, A.; Marlair, G.; Passerini, S. Comprehensive insights into the thermal stability, biodegradability, and combustion chemistry of pyrrolidinium-based ionic liquids. *ChemSusChem* **2017**, *10*, 3146-3159.

28. Lakowicz, J. R. *Principles of Fluorescence Spectroscopy*; Kluwer Academic/Plenum Publishers: New York, USA, 1999.

29. Berezin, M. Y.; Achilefu, S. Fluorescence lifetime measurements and biological imaging. *Chemical Reviews* **2010**, *110*, 2641-2684.

30. Kasha, M. Characterization of electronic transitions in complex molecules. *Discussions of the Faraday Society* **1950**, *9*, 14-19.

31. Cao, Y.; Mu, T. Comprehensive investigation on the thermal stability of 66 ionic liquids by thermogravimetric analysis. *Industrial and Engineering Chemistry Research* **2014**, *53*, 8651-8664.

32. Maton, C.; De Vos, N.; Stevens, C. V. Ionic liquid thermal stabilities: decomposition mechanisms and analysis tools. *Chemical Society Reviews* **2013**, *42*, 5963-5977.

33. Fox, D. M.; Awad, W. H.; Gilman, J. W.; Maupin, P. H.; De Long, H. C. Trulove, P. C. Flammability, thermal stability, and phase change characteristics of several trialkylimidazolium salts. *Green Chemistry* **2003**, *5*, 724-727.

34. Tokuda, H.; Hayamizu, K.; Ishii, K.; Susan, M. A. B. H.; Watanabe, M. Physicochemical properties and structures of room temperature ionic liquids. 2. variation of alkyl chain length in imidazolium cation. *Journal of Physical Chemistry B* **2005**, *109*, 6103-6110.

35. Dixon, N. E.; Lawrance, G. A.; Lay, P. A.; Sargeson, A. M.; Taube, H. In *Trifluoromethanesulfonate and Trifluoromethanesulfonato-O Complexes*; Angelici, R. J., Eds.; John Wiley and Sons: New York, 1990; Vol. 28, pp 71-76.

36. Vogelsang, J.; Kasper, R.; Steinhauer, C.; Person, B.; Heilemann, M.; Sauer, M.; Tinnefeld, P. A reducing and oxidizing system minimizes photobleaching and blinking of fluorescent dyes. *Angewandte. Chemie International Edition* **2008**, *47*, 5465-5469.

37. Altman, R. B.; Terry, D. S.; Zhou, Z.; Zheng, Q.; Geggier, P.; Kolster, R. A.; Zhao, Y.; Javitch, J. A.; Warren, J. D.; Blanchard, S. C. Cyanine fluorophore derivatives with enhanced photostability. *Nature Methods* **2012**, *9*, 68-71.

38. Kolic, P. E.; Siraj, N.; Hamdan, S.; Regmi, B. P.; Warner, I. M. Synthesis and characterization of porphyrin-based GUMBOS and nanoGUMBOS as improved photosensitizers. *Journal of Physical Chemistry C* **2016**, *120*, 5155-5163.

39. Chan, K. L.; Lim, J. P. F.; Yang, X.; Dodabalapur, A.; Jabbour, G. E.; Sellinger, A. High-efficiency pyrene-based blue light emitting diodes: aggregation suppression using a calixarene 3D-scaffold. *Chemical Communications* **2012**, *48*, 5106-5108.

40. Ooyama, Y.; Kagawa, Y.; Harima, Y. Synthesis and solid-state fluorescence properties of structural isomers of novel benzofuro[2,3-c]oxazolocarbazole-type fluorescent dyes. *European Journal of Organic Chemistry* **2007**, *22*, 3613-3621.

41. Wurth, C.; Grabolle, M.; Pauli, J.; Spieles, M.; Resch-Genger, U. Relative and absolute determination of fluorescence quantum yields of transparent samples. *Nature Protocols* **2013**, *8*, 1535-1550.

42. Sadek, P. C. *The HPLC Solvent Guide*; Wiley-Interscience: New York, USA, 2002.

43. Cosa, G.; Focsaneanu, K.-S.; McLean, J. R. N.; McNamee, J. P.; Scaiano, J. C. Photophysical properties of fluorescent DNA-dyes bound to single- and double-stranded DNA in aqueous buffered solution. *Photochemistry and Photobiology* **2001**, *73*, 585-599.

44. Zhou, Y.; He, Q.; Yang, Y.; Zhong, H.; He, C.; Sang, G.; Liu, W.; Yang, C.; Bai, F.; Li, Y. Binaphthyl-containing green- and red-emitting molecules for solution-processable organic light-emitting diodes. *Advanced Functional Materials* **2008**, *18*, 3299-3306.

45. Shukla, S.; Loc, N. H.; Boix, P. P.; Koh, T. M.; Prabhakar, R. R.; Mulmudi, H. K.; Zhang, J.; Chen, S.; Ng, C. F.; Huan, C. H. A. et al. Iron pyrite thin film counter electrodes for dye-sensitized solar cells: high efficiency for iodine and cobalt redox electrolyte cells. *ACS Nano* **2014**, *8*, 10597-10605.

46. Strehlow, W. H.; Cook, E. L. Compilation of energy band gaps in elemental and binary compound semiconductors and insulators. *Journal of Physical and Chemical Reference Data* **1973**, *2*, 163-199.

47. Barone, V.; Cossi, M. Quantum calculation of molecular energies and energy gradients in solution by a conductor solvent model. *Journal of Physical Chemistry A* **1998**, *102*, 1995-2001.

48. Cossi, M.; Rega, N.; Scalmani, G.; Barone, V. Energies, structures, and electronic properties of molecules in solution with the C-PCM solvation model. *Journal of Computational Chemistry* **2003**, *24*, 669-681.

CHAPTER V. CONCLUSIONS AND FUTURE WORK

This dissertation work involved synthesis and the characterization of dyes (with an emphasis on blue emitters) derived from small organic compounds and GUMBOS, for potential application as OLED emitters. Accordingly, in the first chapter, an overview of OLEDs, with a focus on history, market forecast, working principles, classification methods, current status, challenges, and suggestions for further improvements, as well as analytical techniques used in this research, was discussed.

The first project described in Chapter two contains the synthesis and characterization of four structurally related pyrenylpyridine compounds, and an evaluation of the spectral, optical, physical, and electronic properties of these compounds in both solutions and in solid-state (as thin films on quartz substrates and inside OLED prototypes). Interestingly, the photo-physical properties of these compounds were found to be quite diverse, stemming from factors such as molecular symmetry and the extent of inter/intramolecular interactions, which are attributable to variations in the conformations. These compounds exhibited high photothermal stability and favorable optoelectronic properties. Interestingly, the OLED prototype fabricated with 2,4,6-TPP as the non-doped emissive layer showed bright sky-blue electroluminescence with promising device performance. An evaluation of the structure-property relationships of the pyrenylpyridines as model compounds related to pyrene aided in understanding the important role of morphology induced inter- and intramolecular interactions that tremendously influence the spectral and physical characteristics of these structurally related molecules. Future directions for this research would involve fabrication and characterization of OLED prototypes for the other three DPPs to understand electroluminescence and OLED characteristic variation with the structure of these compounds. Also, fabrication of OLED prototypes with a doped emissive layer created by

embedding pyrenylpyridines in a suitable host matrix is important, since this approach may further improve device performance.

The second project discussed in Chapter three involved the synthesis and characterization of three novel organic blue emitters derived from pyrene-benzimidazole hybrids (compounds A, B, and C). Learning from the first project, these compounds were designed to avoid solid-state dye aggregation to obtain significantly pure blue electroluminescence. Spectroscopic characteristics of these materials, such as solid-state morphology, absorption, photoluminescence, and quantum yield, as well as electronic properties based on cyclic voltammetry and UV-vis absorption, were investigated and found suitable for optoelectronic applications. An OLED prototype fabricated using compound B as the non-doped emissive layer displayed a significantly pure blue electroluminescence as expected. Future directions for this research include fabrication and characterization of OLED prototypes for the other two compounds and fabrication of OLED prototypes with a doped emissive layer by embedding these dyes in a suitable host matrix to further improve device performance.

In the third project discussed in Chapter 4, a series of novel solid-state organic salts derived from propidium luminophore (PGUMBOS) were synthesized, and photo-physical characteristics such as solubility, crystallinity, photothermal stability, electrochemistry, and spectroscopy, including absorption, photoluminescence, quantum yields, and lifetimes, were systematically investigated. Noteworthy, PGUMBOS exhibited a substantially lower crystallinity, better solubility and quantum efficiency in less polar solvents, and a high thermal stability relative to the parent compound, [P][I]. Also, these PGUMBOS materials showed improved resistance to photodegradation. These novel PGUMBOS materials were organic semiconductors with electronic properties suitable for a variety of optoelectronic applications. Therefore, GUMBOS were

recognized as one of the promising molecular designs for optoelectronic applications. For future work related to this research, it is important to prepare and evaluate electroluminescent devices with these GUMBOS materials as emissive layers and compare the performance with OLEDs fabricated using non-GUMBOS analogues to further understand the influence of counterion variations on ionic luminophores.

APPENDIX A. SUPPORTING INFORMATION FOR CHAPTER 2

Characterization of pyrenylpyridines

2,4-DPP: HRMS-ESI ($CHCl_3$): m/z 480.1800 ($M+H^+$ for $C_{37}H_{21}N$, calculated mass 480.1674); ^1H NMR ($CDCl_3$, 400 MHz, ppm): δ 9.09 (d, J = 4.00Hz, 1H), 8.65(d, J = 8.00Hz, 1H), 8.37-8.31 (m, 4H), 8.28-8.19 (m, 4H), 8.14-8.03 (m, 10H), 7.73 (d, J = 4.00Hz, 1H); ^{13}C Proton Decoupled NMR ($CDCl_3$, 400 MHz, ppm): δ 159.72, 149.79, 135.58, 134.56, 131.56, 131.52, 131.42, 130.93, 130.87, 128.74, 128.41, 128.29,), 128.20, 128.17, 128.00, 127.80, 127.47, 127.43, 127.33, 127.18, 126.32, 126.07, 125.67, 125.42, 125.35, 125.01, 124.87, 124.79, 124.43, 123.83.

2,6-DPP: HRMS-ESI ($CHCl_3$): m/z 480.1767 ($M+H^+$ for $C_{37}H_{21}N$, calculated mass 480.1674); ^1H NMR ($CDCl_3$, 400 MHz, ppm): δ 8.65 (d, J = 12.00Hz, 2H), 8.39 (d, J = 8.00Hz, 2H), 8.33 (d, 8.00Hz, 2H), 8.25 -8.22 (m, 4H), 8.18-8.11 (m, 7H), 8.07-8.04 (t, J = 8.00Hz, 2H), 7.88-7.87 (d, J = 4.00Hz, 2H); ^{13}C Proton Decoupled NMR ($CDCl_3$, 400 MHz, ppm): δ 159.53, 136.58, 131.43, 130.94, 129.60, 128.75, 127.99, 127.92, 127.88, 127.46, 126.01, 125.35, 125.13, 125.07, 124.88, 124.02.

3,5-DPP: HRMS-ESI ($CHCl_3$): m/z 480.1761 ($M+H^+$ for $C_{37}H_{21}N$, calculated mass 480.1674); ^1H NMR ($CDCl_3$, 400 MHz, ppm): δ 9.07 (d, J = 4Hz, 2H), 8.34-8.32 (m, 4H), 8.30-8.23 (m, 5H), 8.17-8.13 (m, 8H), 8.09-8.06 (m, 2H); ^{13}C Proton Decoupled NMR ($CDCl_3$, 400 MHz, ppm): δ 149.48, 139.71, 136.75, 133.17, 131.46, 131.36, 130.90, 128.82, 128.37, 128.06, 127.77, 127.35, 126.29, 125.60, 125.27, 125.06, 124.90, 124.81, 124.34.

2,4,6-TPP: HRMS-ESI ($CHCl_3$): m/z 680.2342 ($M+H^+$ for $C_{53}H_{29}N$, calculated mass 480.2300); ^1H NMR ($CDCl_3$, 400 MHz, ppm): δ 8.88-8.86 (d, J = 8Hz, 2H), 8.56 (t, J = 8Hz, 3H), 8.35 (t, J = 8Hz, 3H), 8.27-8.22 (m, 9H), 8.20-8.15 (m, 9H), 8.09-8.03 (m, 4H); ^{13}C Proton Decoupled NMR ($CDCl_3$, 400 MHz, ppm): δ 159.70, 149.92, 135.87, 134.67, 131.60, 131.44, 130.96, 130.89, 128.90, 128.50, 128.43, 128.19, 128.15, 128.11, 127.95, 127.46, 127.34, 126.31, 126.03, 125.80, 125.69, 125.40, 125.21, 125.12, 125.09, 124.95, 124.84, 124.41.

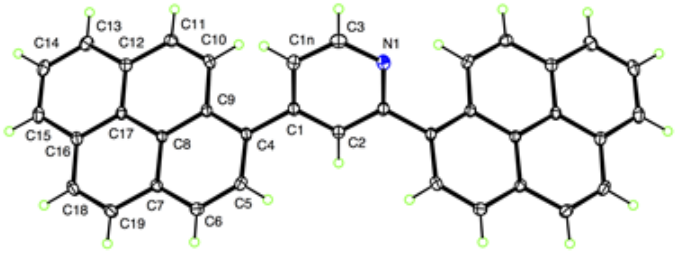

2,4-DPP

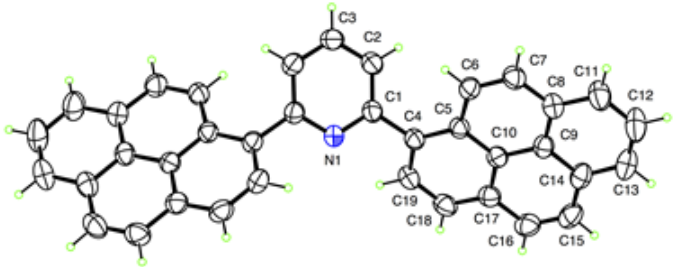

2,6-DPP

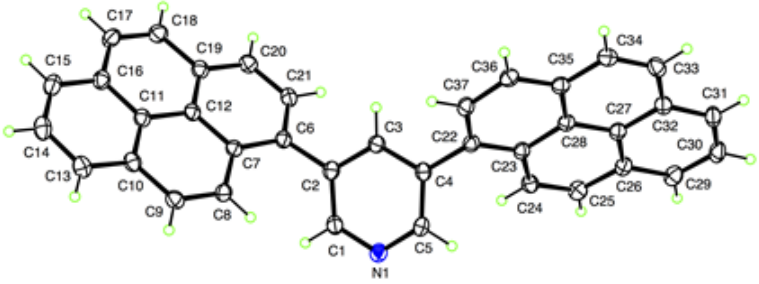

3,5-DPP

Figure A1. Single-crystal XRD derived ORTEP diagrams of dipyrenylpyridines.

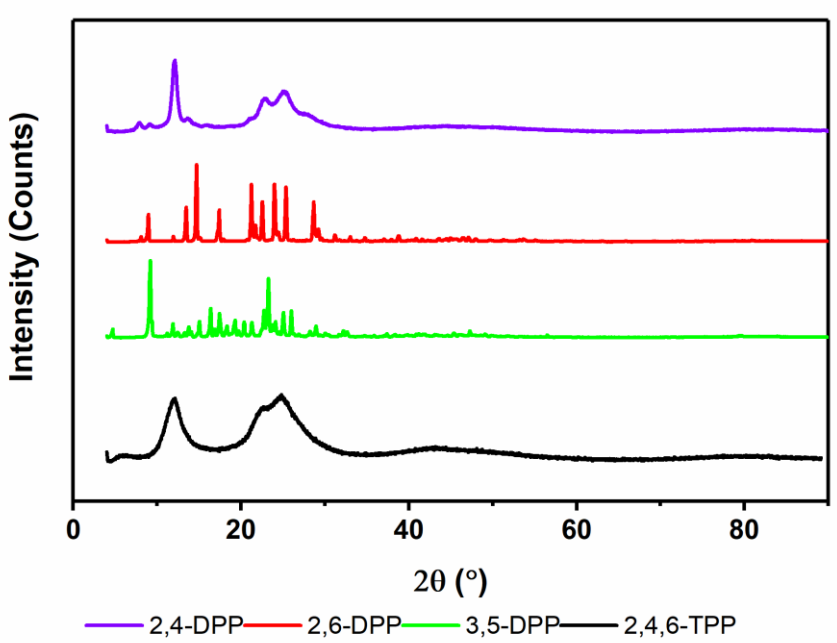

Figure A2. PXRDs of pyrenylpyridines.

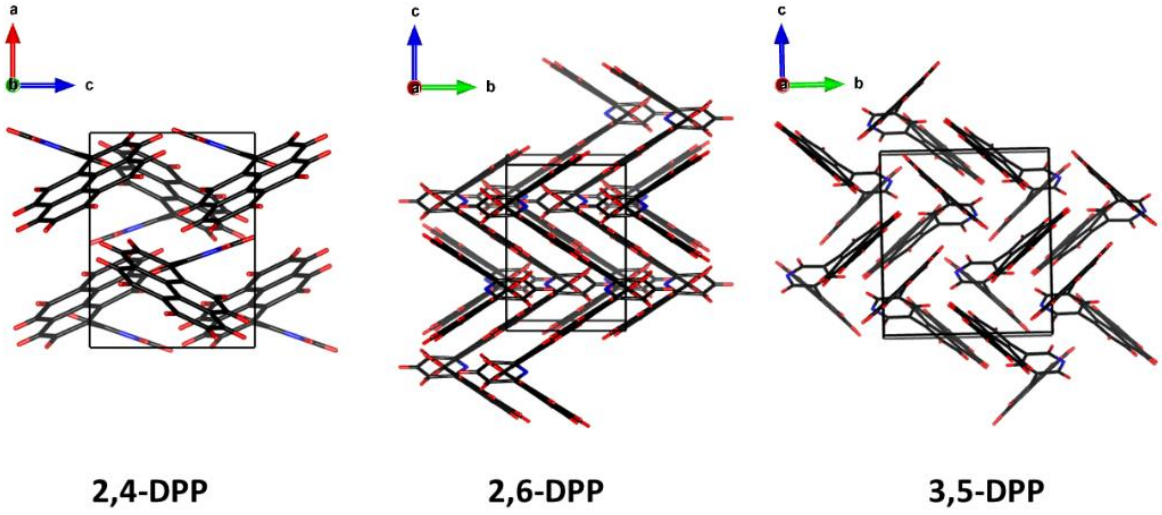

Figure A3. Molecular packing of dipyrenylpyridines in the unit cells derived from single-crystal XRD.

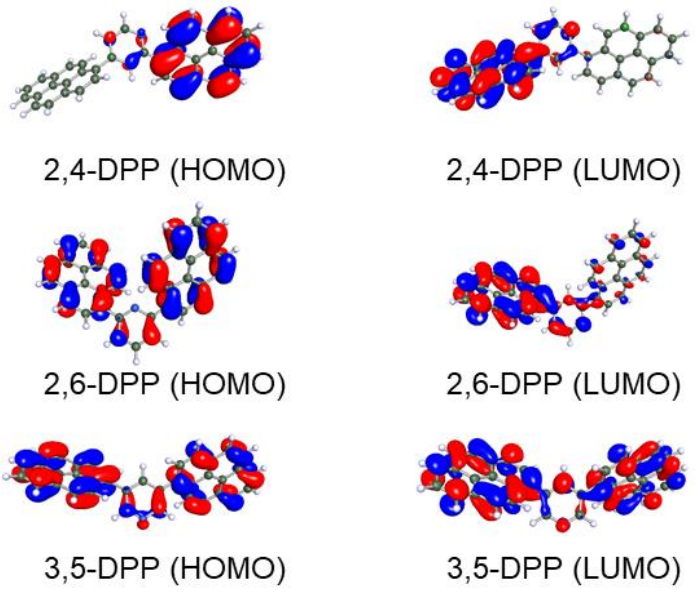

Figure A4. HOMO (left) and LUMO (right) of DPPs.

Table A1. Energy gaps of pyrenylpyridines obtained from computational studies.

Compound	2,4-DPP	2,6-DPP	3,5-DPP	2,4,6-TPP
Computed energy gap (eV)	3.44	3.27	3.64	3.42
Experimental energy gap (eV)	3.16	3.16	3.28	3.12

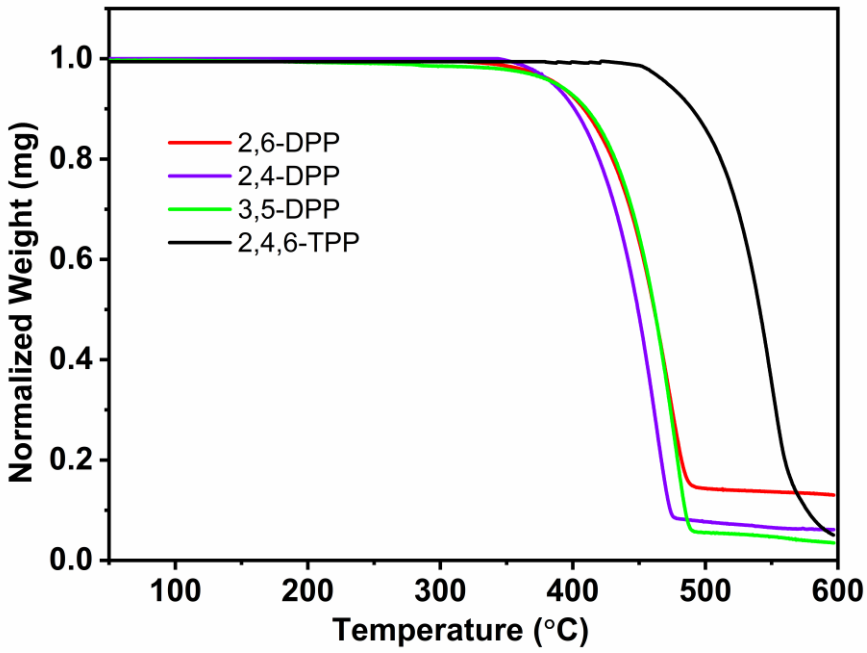

Figure A5. Thermogravimetric profiles of pyrenylpyridines.

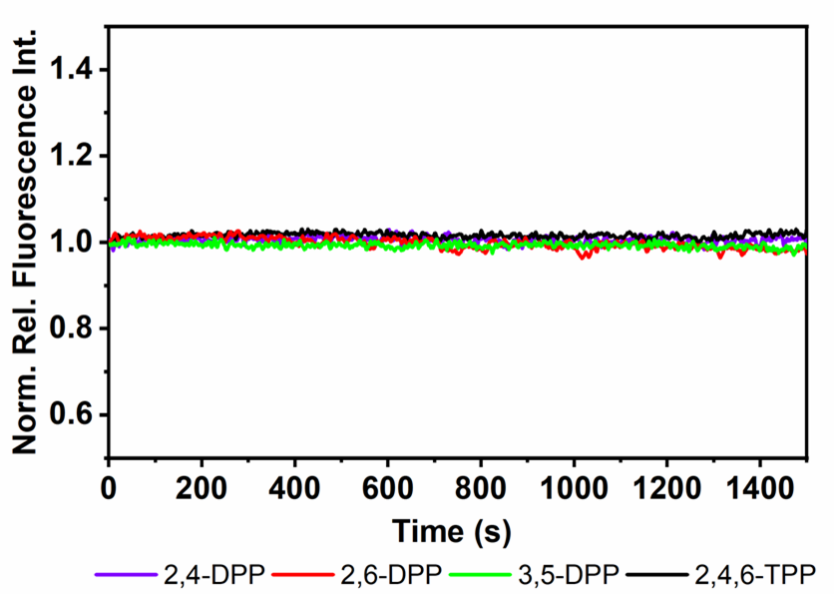

Figure A6. Time-dependent relative photoluminescence intensity spectra of pyrenylpyridines in chloroform solvent over a period of 1500 s.

Table A2. Emission maxima (nm) of pyrenylpyridines in different solvents.

Solvent	2,4-DPP	2,6-DPP	3,5-DPP	2,4,6-TPP
Hexane	392	394	393	396
Methanol	407	405	406	410
DMSO	428	429	429	444

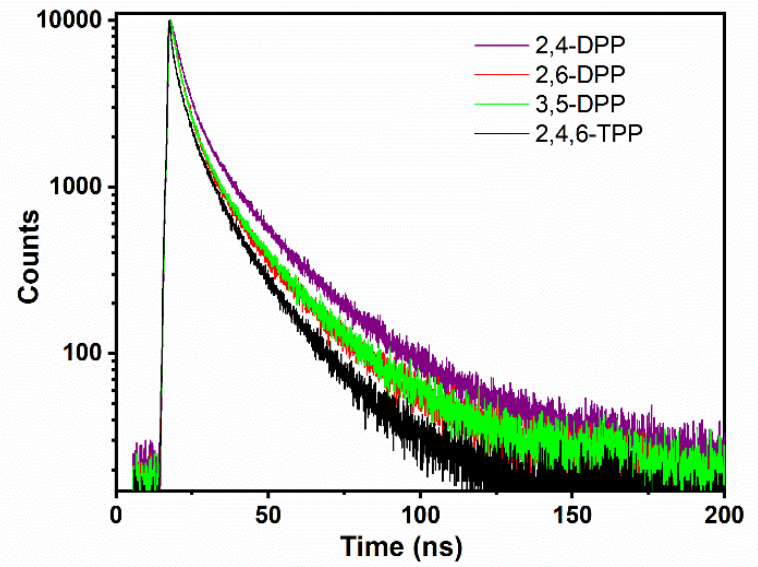

Figure A7. Fluorescence decay curves of pyrenylpyridines solid films monitored at emission maxima with a 1.5 nm band pass and excitation at 375 nm.

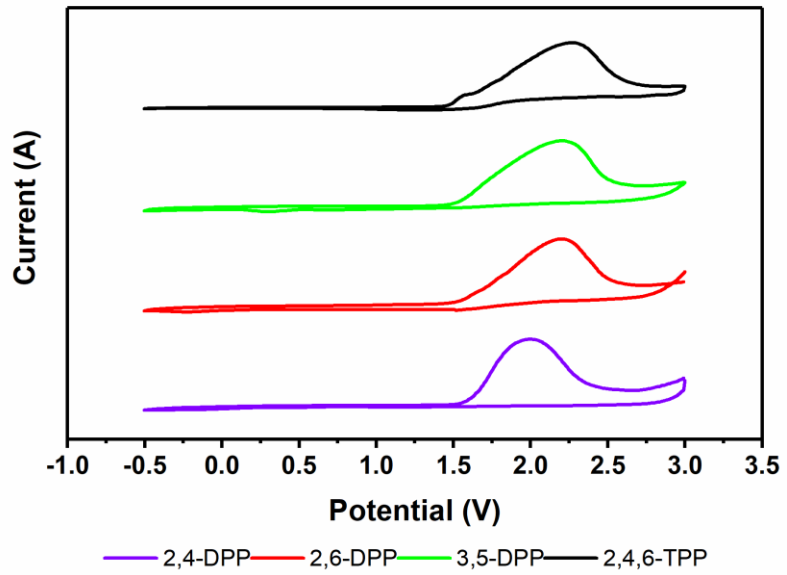

Figure A8. Cyclic voltammograms of pyrenylpyridines.

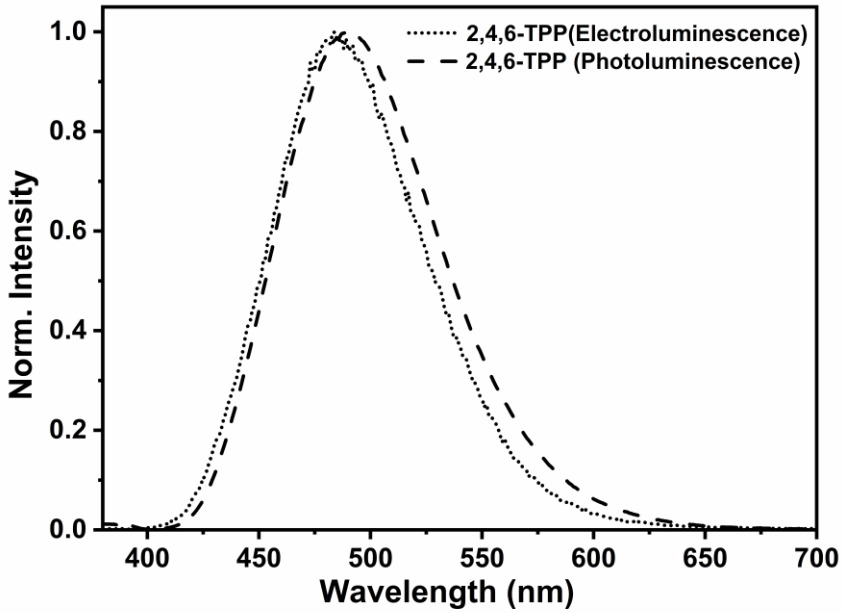

Figure A9. Photoluminescence and electroluminescence (in OLED device) of 2,4,6-TPP in solid state.

APPENDIX B. SUPPORTING INFORMATION FOR CHAPTER 3

Characterization of compound A, B and C - ^{1}H, ^{13}C NMR, ESI-MS/MALDI-MS data

Compound A: HRMS-ESI ($CHCl_3$); m/z 527.2417 ($M+H^+$ for $C_{39}H_{30}N_2$, calculated mass 527.2409); ^{1}H NMR (CD_2Cl_2, 400 MHz, ppm): δ 8.31 (s, 2H), 8.13 -8.15 (m, 4H), 8.10-8.08 (m, 2H), 8.048-8.03 (m, 1H), 7.95-7.91 (m, 2H), 7.84-7.82 (d, 1H), 7.72-7.70 (m, 3H), 7.61-7.57 (t, 1H), 7.50-7.52 (m, 2H), 7.38-7.42 (m), 7.35-7.36 (m, 2H), 1.64 (s, 9H); ^{13}C Proton Decoupled NMR (CD_2Cl_2, 400 MHz, ppm): δ 152.13, 149.44, 143.26, 141.25, 137.56, 137.50, 131.36, 130.96, 130.76, 130.13, 129.05, 128.74, 128.66, 128.39, 128.01, 127.83, 127.22, 123.80, 123.30, 123.19, 122.83, 122.54, 119.69, 110.46, 35.16, 31.63.

Compound B: HRMS-ESI ($CHCl_3$); m/z 795. 3592 ($M+H^+$ for $C_{58}H_{42}N_4$, calculated mass 795.3409); ^{1}H NMR ($CDCl_3$, 400 MHz, ppm): δ 8.24 (s, 2H), 7.99 -7.93 (q, 6H), 7.90-7.87 (m, 2H), 7.76 (m, 2H), 7.66-7.58 (m, 4H), 7.55-7.51 (m, 3H), 7.43-7.35 (m, 11H), 7.30-7.29 (d, 3H), 1.63 (s, 9H); ^{13}C Proton Decoupled NMR (CD_2Cl_2, 400 MHz, ppm): δ 152.26, 149.55, 143.22, 140.89, 137.46, 137.10, 136.13, 133.38, 132.35, 131.98, 131.89, 131.69, 131.56, 131.01, 130.49, 130.00, 129.09, 128.73, 128.56, 128.52, 128.44, 128.42, 128.05, 127.68, 127.56, 124.98, 124.53, 123.29, 123.08, 122.83, 122.54, 119.68, 110.49, 35.13, 31.61.

Compound C: MALDI-MS ($CHCl_3$); m/z 1274.661 (M^+ for $C_{92}H_{58}N_8$, calculated mass 1274.4784); ^{1}H NMR ($CDCl_3$, 400 MHz, ppm): δ 7.94-7.92 (d, 3H), 7.88-7.85 (m, 3H), 7.81 (s, 3H), 7.78 (s, 3H), 7.72-7.67 (m, 2H), 7.62 (m, 5H), 7.60-7.56 (m, 2H), 7.53-7.48 (m, 10H), 7.43-7.41 (m, 6H), 7.40-7.33 (m, 10H), 7.31-7.30 (m, 7H), 7.27-7.21 (m, 4H); ^{13}C Proton Decoupled NMR ($CDCl_3$, 400 MHz, ppm): δ 152.26, 143.10, 140.90, 137.28, 137.01, 136.31, 134.06, 132.16,

132.07, 131.94, 131.91, 131.84, 131.66, 130.49, 130.00, 130.39, 130.04, 129.59, 128.78, 128.62, 128.56, 128.44, 127.93, 127.51, 125.48, 125.17, 123.50, 123.10, 119.96, 110.55.

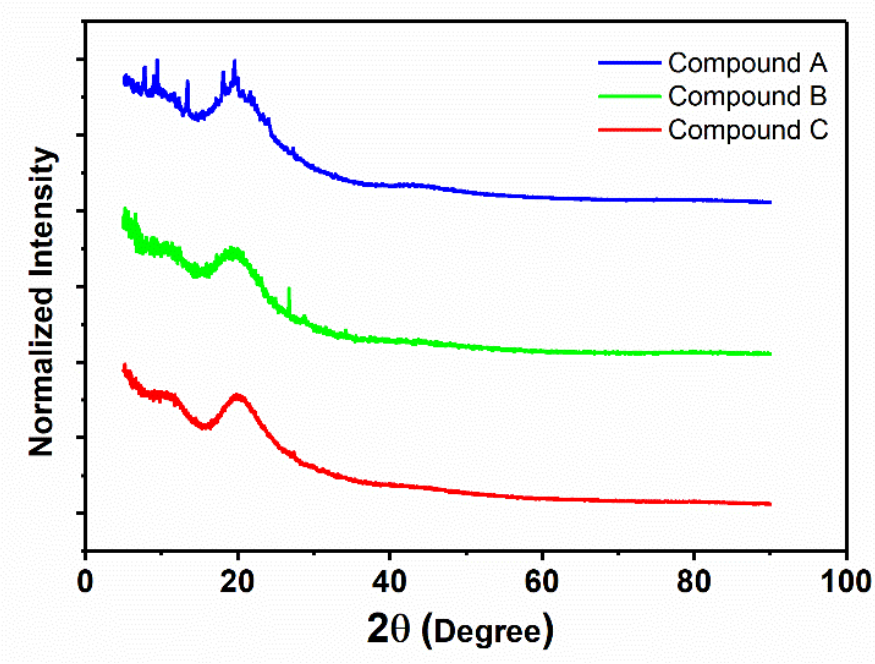

Figure B1. PXRDs of pyrenylpyridines.

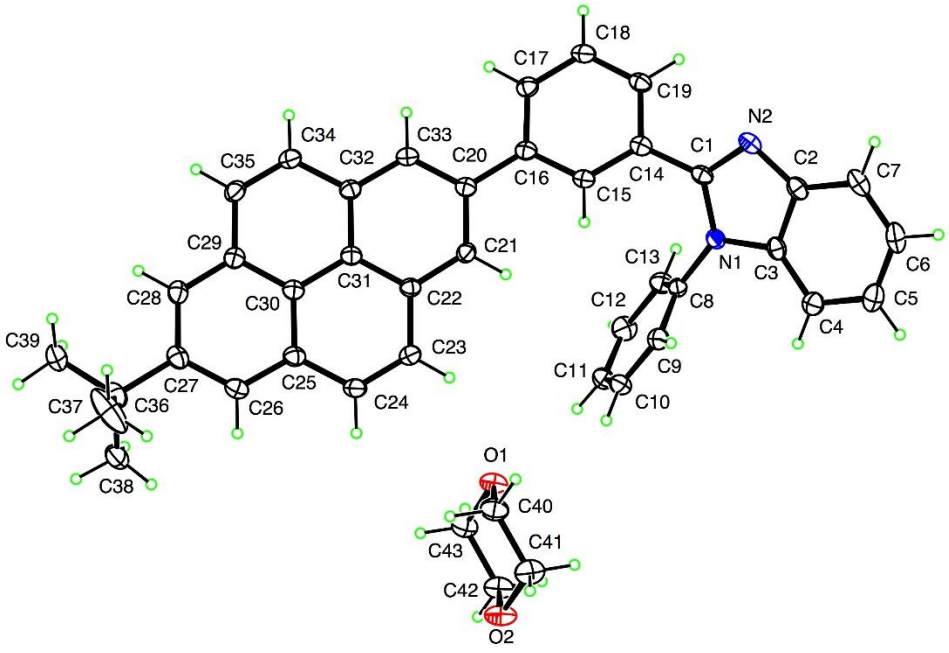

Figure B2. Single-crystal XRD derived ORTEP diagram of compound A.

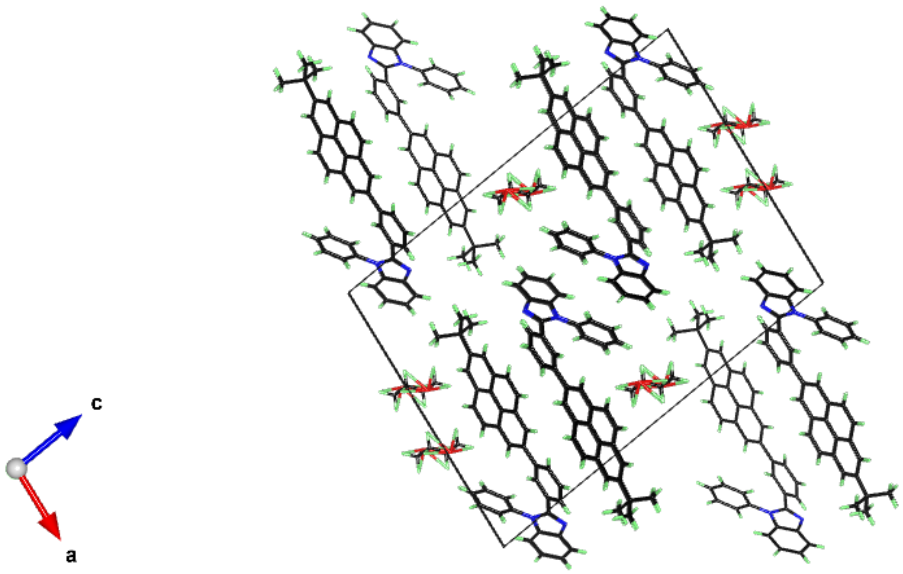

Figure B3. Molecular packing of compound A in the unit cells derived from single-crystal XRD.

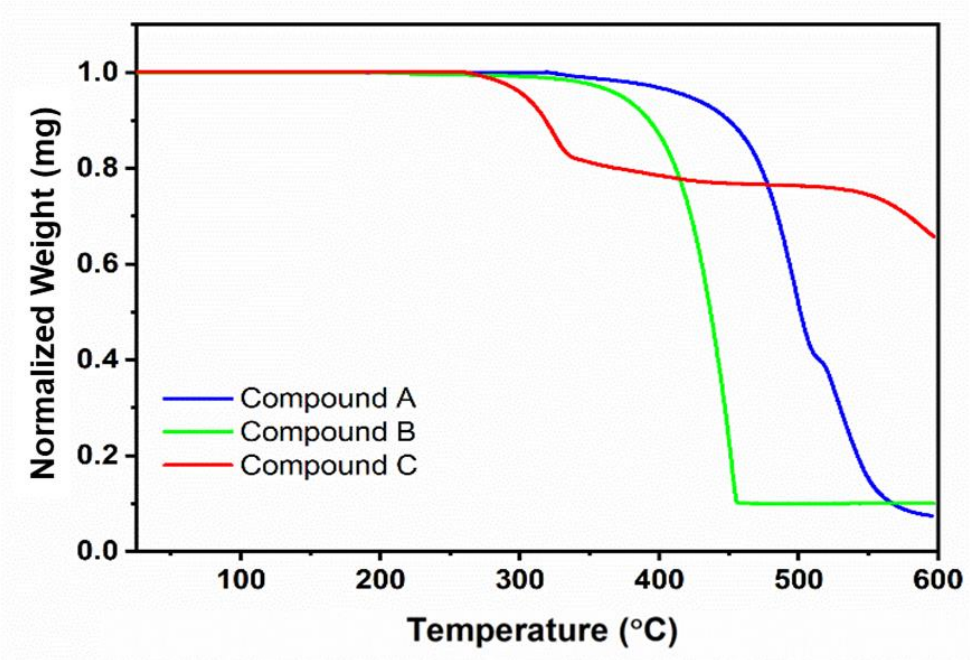

Figure B4. TGA profiles of compounds A, B, and C.

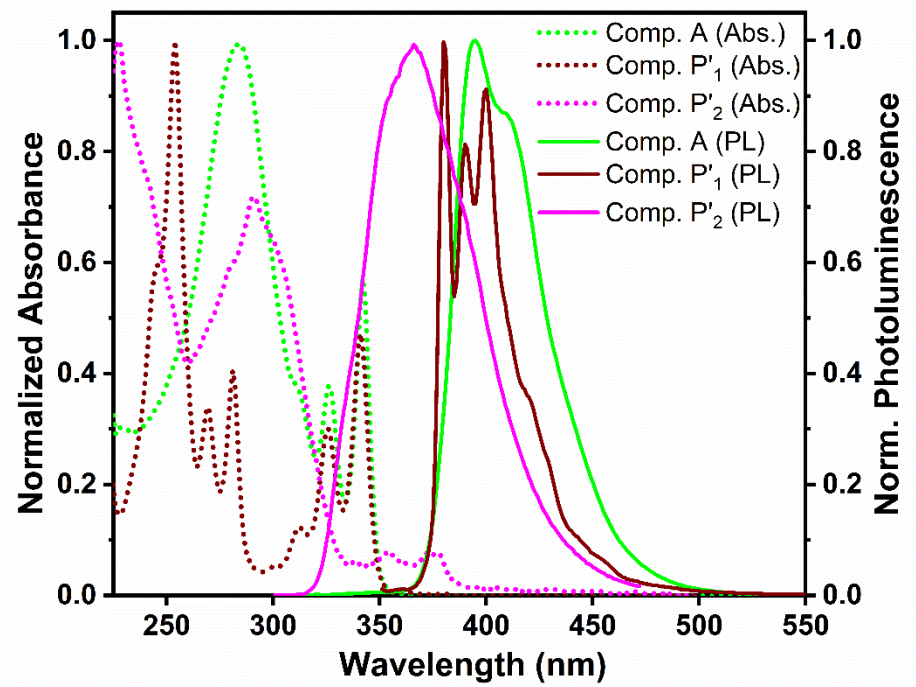

Figure B5. Normalized UV-vis absorption (Abs.) and photoluminescence (PL) spectra of compound A, and its parent compounds: pyrene derivative (P'$_1$) and benzimidazole derivative (P'$_2$) in DCM.

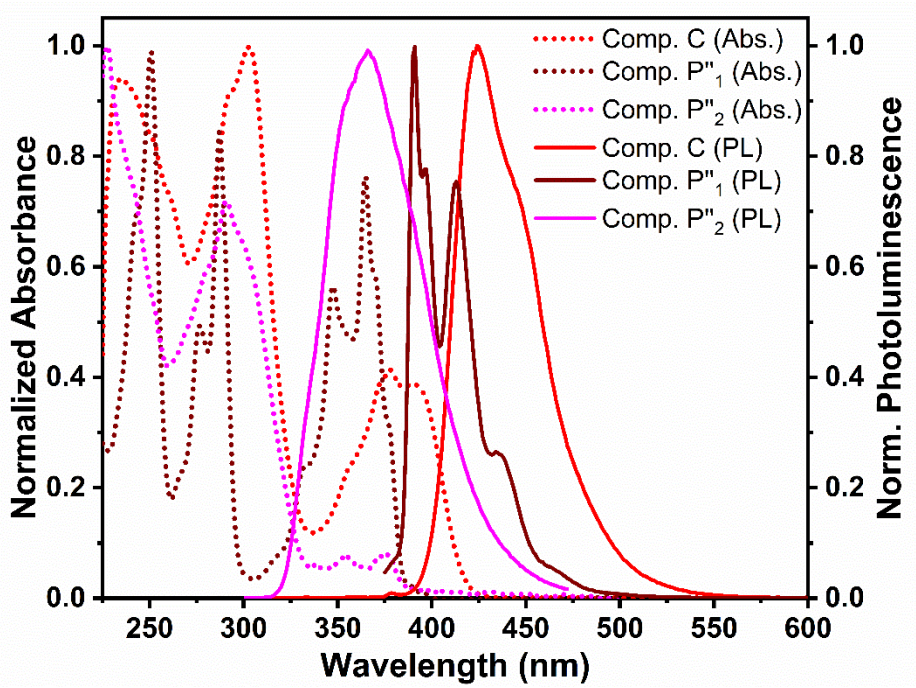

Figure B6. Normalized UV-vis absorption (Abs.) and photoluminescence (PL) spectra of compound C, and its parent compounds: pyrene derivative (P"$_1$) and benzimidazole derivative (P"$_2$) in DCM.

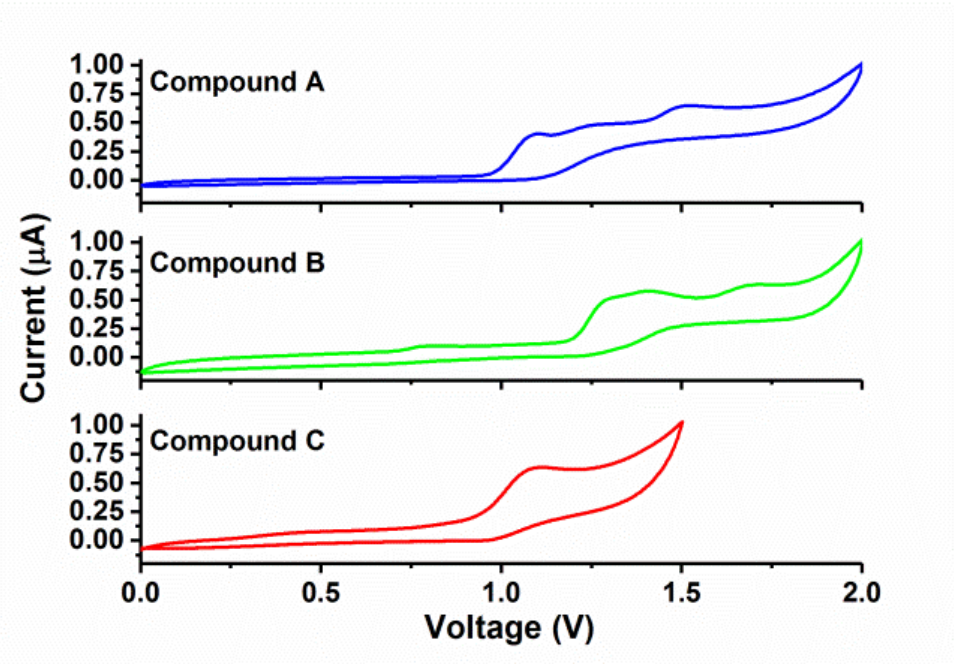

Figure B7. Cyclic voltammograms of compounds A, B, and C.

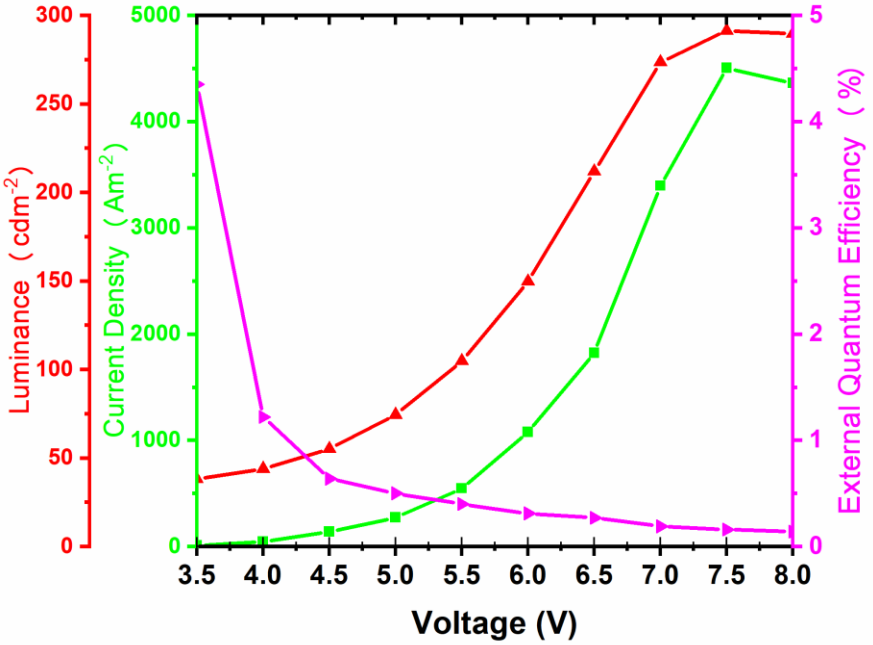

Figure B8. Performance plots for the OLED prototype with compound B as the emissive layer.

APPENDIX C. SUPPORTING INFORMATION FOR CHAPTER 4

Synthesis protocols of [P][NTf_2] and [P][TfO]

Synthesis of [P][NTf_2]: The starting material [P][I] (50 mg, 0.075 mmol) was dissolved in 60 mL of DI water in a 500 mL round bottom flask. Then, [Li][NTf_2] (43 mg, 0.15 mmol) was added to the aqueous [P][I] solution and stirred for approximately 5 minutes until [Li][NTf_2] is completely dissolved. Then, DCM (300 mL) was gradually added to the same round bottom flask containing the aqueous [P][I] and [Li][NTf_2] solution. Once DCM was added, the resultant biphasic solution was stirred vigorously for 6 hours at room temperature. Then, this biphasic solution was transferred to a separatory funnel and the bottom organic layer was carefully siphoned into a container. The extracted organic layer was washed three times with DI water (200 mL x 3) to remove traces of the byproduct, [Li][I], which is water soluble. Then, anhydrous magnesium sulfate was added to the DCM layer to remove trace amounts of water from the organic layer, followed by suction filtration to remove magnesium sulfate particles. The dried and filtered organic layer was vacuum evaporated to remove DCM. The resultant product, [P][NTf_2], was freeze dried, and obtained as a maroon color solid (68 ±4 mg, yield: 93 ±5%).

Synthesis of [P][TfO]: The starting material [P][I] (50 mg, 0.075 mmol) was dissolved in 300 mL of ACN in a 500 mL round bottom flask. Then, [Na][TfO] (26 mg, 0.15 mmol) was added to the same flask and stirred for 48 hours at room temperature. Then, this solution was concentrated by use of solvent evaporation. Next, the concentrated solution was sent through a short silica gel column, first with 100% methanol as the solvent to elute NaI byproduct. The remaining red color band of [P][TfO] at the bottom was eluted using 100% acetone and combined fractions were filtered to remove any silica particles. The solvent was evaporated using a rotatory evaporator. The

resultant product, [P][TfO], was freeze dried, and obtained as a maroon color solid (45 ±5 mg, yield: 84 ±10%).

Summary of ESI-MS and ^{1}H, ^{13}C, and ^{19}F NMR data for [P][I] and PGUMBOS

[P][I]: MS, ESI^{+}- m/z 207.1397 (P^{2+}); MS, ESI^{-}- m/z 126.9049 (I^{-}); ^{1}H NMR (d-DMSO, 400 MHz, ppm): δ 8.69-8.72 (d, 1H), 8.64 -8.66 (d, 1H), 7.76-7.81 (m, 5H), 7.55-7.57 (m, 2H), 7.36-7.38 (d, 1H), 6.39 (s, 2H), 6.27-6.28 (d, 1H), 5.99 (s, 2H), 4.45 (s, 2H), 3.21-3.26 (m,6H), 2.89 (s, 3H), 2.23 (m, 2H), 1.13-1.17 (t,6H); ^{13}C Proton Decoupled NMR (d-DMSO, 400 MHz, ppm): δ 159.24, 151.71, 148.59, 134.69, 132.36, 131.47, 130.00, 128.86, 128.70, 128.07, 125.47, 125.27, 123.21, 120.53, 117.95, 108.27, 98.64, 56.55, 56.01, 50.67, 47.21, 21.68, 8.04

[P][BETI]: MS, ESI^{+}- m/z 207.1392 (P^{2+}); MS, ESI^{-}- m/z 379.9116 ($BETI^{-}$); ^{1}H NMR (CD_2Cl_2, 400 MHz, ppm): δ 8.55-8.57 (d, 1H), 8.49-8.51 (d, 1H), 7.82-7.84 (m, 3H), 7.63-7.65 (m, 2H), 7.56-7.59 (d, 1H), 7.44 (d, 1H), 7.36-7.39 (d, 1H), 6.47-6.48 (d, 1H), 4.64-4.68 (t, 2H), 3.26-3.34 (m, 6H), 2.94 (s, 3H), 2.37 (m, 2H), 1.26-1.29 (m,6H); ^{13}C Proton Decoupled NMR (CD_2Cl_2, 400 MHz, ppm): δ 159.11, 151.19, 146.51, 134.93, 131.71, 131.32, 130.07, 129.90, 128.91, 128.20, 125.28, 125.04, 122.73, *122.17*, 120.68, *119.64*, *119.31*, *118.98*, 118.72, *116.45*, *114.34*, *111.80*, *111.42*, 110.07, *108.88*, 98.02, 56.96, 56.85, 49.62, 47.30, 21.68, 7.50 (Signals coming from C atoms in the anion are split due to the attached F atoms and are presented in italics) ; ^{19}F NMR (CD_2Cl_2, 500 MHz, ppm): δ -78.90, -117.54

[P][NTf_2]: MS, ESI^{+}- m/z 207.1389 (P^{2+}); MS, ESI^{-}- m/z 279.9177 (NTf_2^{-}) ^{1}H NMR (CD_2Cl_2, 400 MHz, ppm): δ 8.56-8.58 (d, 1H), 8.49-8.52 (d, 1H), 7.83-7.85 (m, 3H), 7.64-7.65 (m, 2H), 7.57-7.60 (d, 1H), 7.47 (d, 1H), 7.37-7.39 (d, 1H), 6.48-6.49 (d, 1H), 4.66-4.70 (t, 2H), 3.26-3.34 (m,

6H), 2.95 (s, 3H), 2.38 (m, 2H), 1.27-1.31 (m, 6H); ^{13}C Proton Decoupled NMR (CD_2Cl_2, 400 MHz, ppm): δ 159.19, 151.12, 146.52, 134.93, 131.71, 131.31, 130.09, 129.85, 128.90, 128.21, 125.29, 125.06, *124.46*, 122.76, *121.26*, 120.67, *118.74*, 118.07, *114.88*, 110.15, 98.17, 56.91, 56.90, 49.71, 47.39, 21.71, 7.56 (Signals coming from C atoms in the anion are split due to the attached F atoms and are presented in italics) ; ^{19}F NMR (CD_2Cl_2, 500 MHz, ppm): δ -78.73

[P][TfO]: MS, ESI$^+$- m/z 207.1382 (P^{2+}); MS, ESI$^-$- m/z 148.9529 (TfO^-) ^{1}H NMR (d-DMSO, 400 MHz, ppm): δ 8.69-8.71 (d, 1H), 8.63-8.65 (d, 1H), 7.80 (m, 3H), 7.74-7.76 (m, 2H), 7.54-7.57 (d, 1H), 7.36-7.39 (m, 2H), 6.33 (s, 2H), 6.27-6.28 (d, 1H), 6.0 (s, 2H), 4.44 (t, 2H), 3.19-3.24 (m, 6H), 2.86 (s, 3H), 2.21 (m, 2H), 1.13-1.16 (m, 6H); ^{13}C Proton Decoupled NMR (d-DMSO, 500 MHz, ppm): δ 159.25, 151.68, 148.62, 134.72, 132.38, 131.47, 130.00, 128.84, 128.71, 128.07, *125.95*, 125.49, 125.28, 123.20, *122.74*, 120.51, *119.54*, 117.98, *116.34*, 108.27, 98.60, 56.52, 55.97, 50.63, 47.17, 21.64, 7.95 (Signals coming from C atoms in the anion are split due to the attached F atoms and are presented in italics) ; ^{19}F NMR (d-DMSO, 500 MHz, ppm): δ -77.75

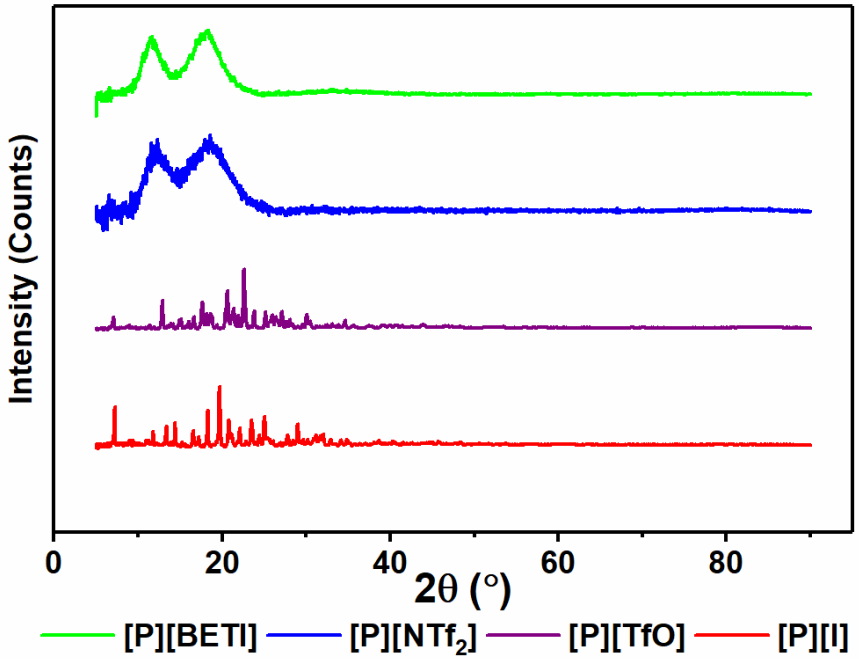

Figure C1. PXRD profiles of [P][I] and PGUMBOS.

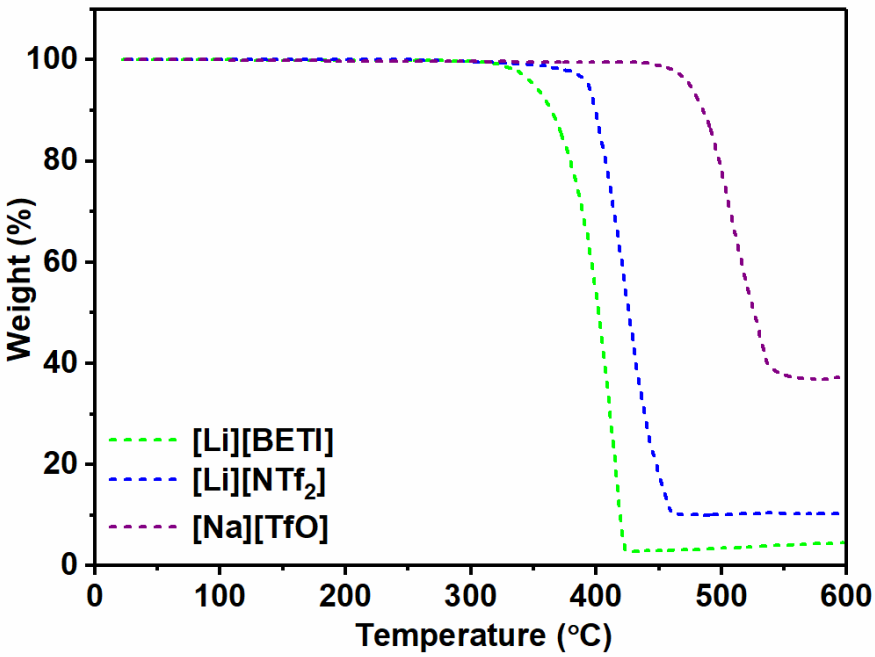

Figure C2. TGA profiles of [Li][BETI], [Li][NTf_2], and [Na][TfO].

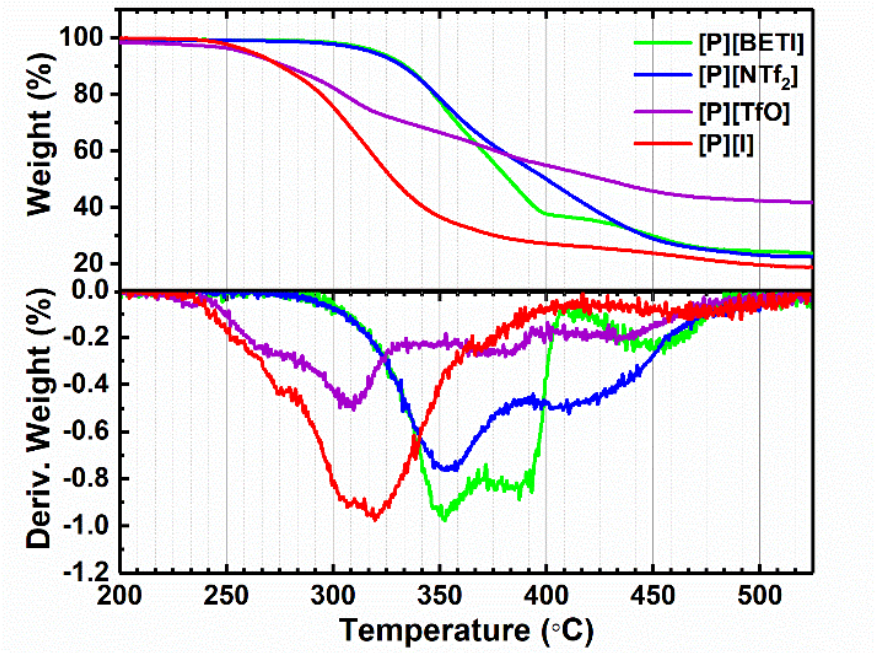

Figure C3. TGA profiles with first derivative curves for [P][I] and PGUMBOS showing multiple inflection points.

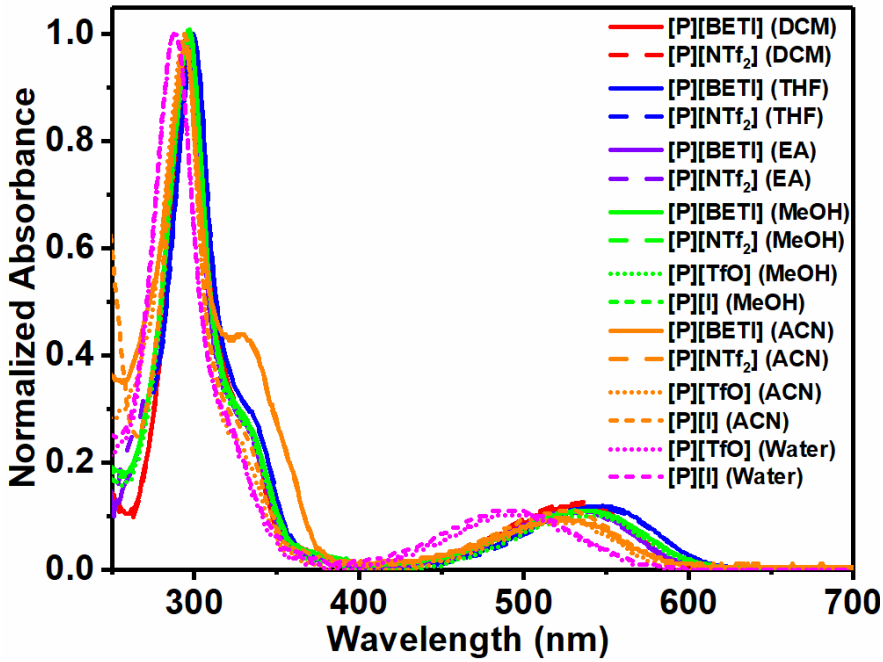

Figure C4. Absorption spectra of [P][I] and PGUMBOS in different solvents.

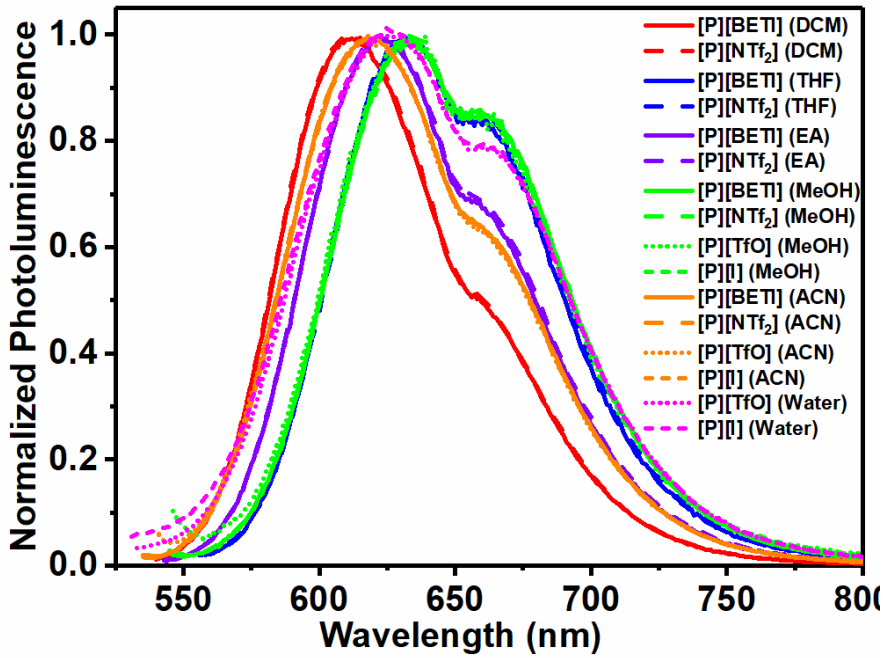

Figure C5. Emission spectra of [P][I] and PGUMBOS in different solvents when excited at A_{max1} wavelength.

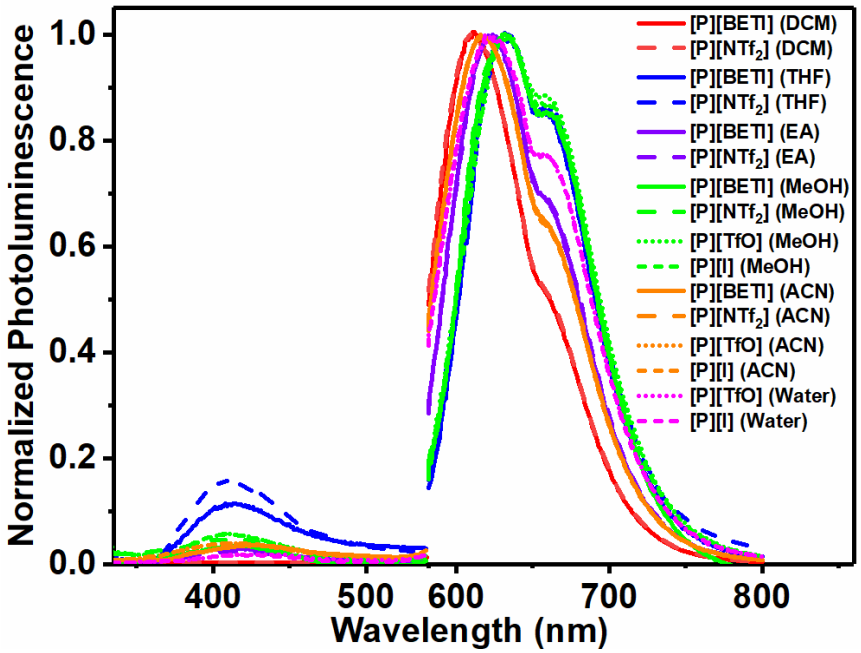

Figure C6. Emission spectra of [P][I] and PGUMBOS in different solvents when excited at A_2 wavelength.

Table C1. Absorption maxima of [P][I] and PGUMBOS in different solvents.

Solvent / Compound	DCM	THF	EA	MeOH	ACN	Water
[P][BETI]	297, 530	299,548	296, 533	296,535	295,525	N/A
[P][NTf_2]	297, 533	299, 546	296,534	296,532	295,526	N/A
[P][TfO]	N/A	N/A	N/A	296, 536	294, 531	288, 493
[P][I]	N/A	N/A	N/A	296, 536	294, 525	288, 491

N/A: Not available due to the limited solubility

Table C2. Emission maxima of [P][I] and PGUMBOS in different solvents when excited at A_1 wavelengths.

Solvent / Compound	DCM	THF	EA	MeOH	ACN	Water
[P][BETI]	614	633	623	632	617	N/A
[P][NTf_2]	612	630	624	635	619	N/A
[P][TfO]	N/A	N/A	N/A	635	620	624
[P][I]	N/A	N/A	N/A	633	618	625

N/A: Not available due to the limited solubility

Table C3. Emission maxima of [P][I] and PGUMBOS in different solvents when excited at A_2 wavelengths.

Solvent / Compound	DCM	THF	EA	MeOH	ACN	Water
[P][BETI]	611[a]	631[a],411[b]	624[a],412[b]	632[a],410[b]	617a,426[b]	N/A
[P][NTf_2]	612[a]	632[a],411[b]	623[a],409[b]	632[a],413[b]	617a,421[b]	N/A
[P][TfO]	N/A	N/A	N/A	631[a],408[b]	616[a],414[b]	623[a],425[b]
[P][I]	N/A	N/A	N/A	632[a],410[b]	616[a],415[b]	622[a],424[b]

[a] S_1 emission, [b] S_2 emission, N/A: Not available due to the limited solubility

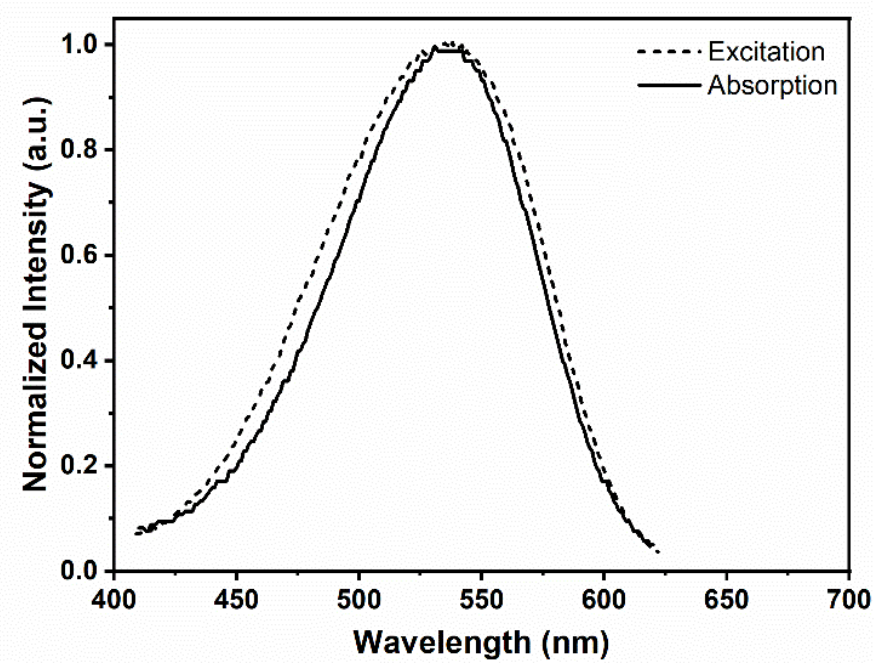

Figure C7. Normalized absorption and excitation spectra of [P][BETI] related to S_1 emission in methanol solution.

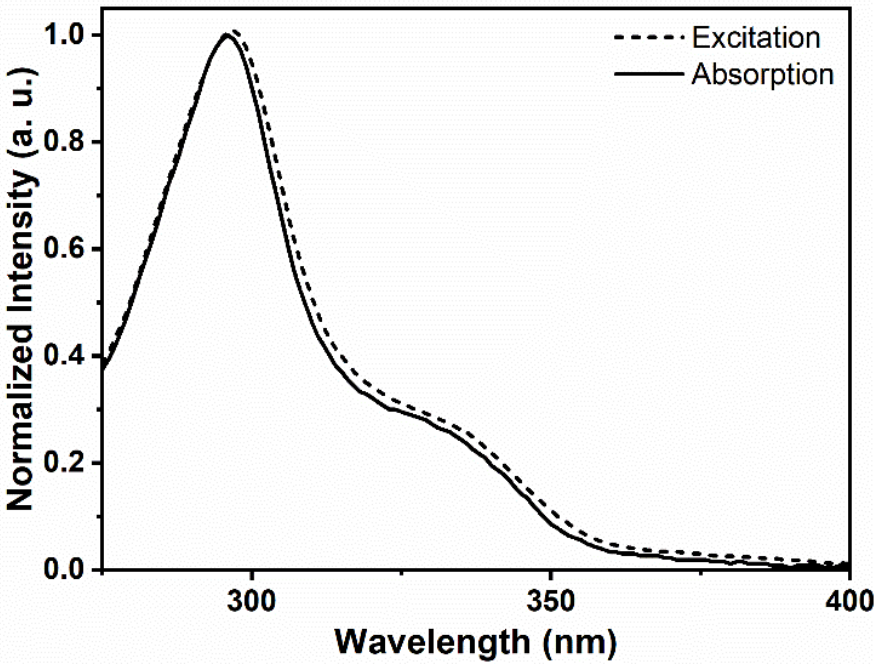

Figure C8. Normalized absorption and excitation spectra of [P][BETI] related to S_2 emission in methanol solution.

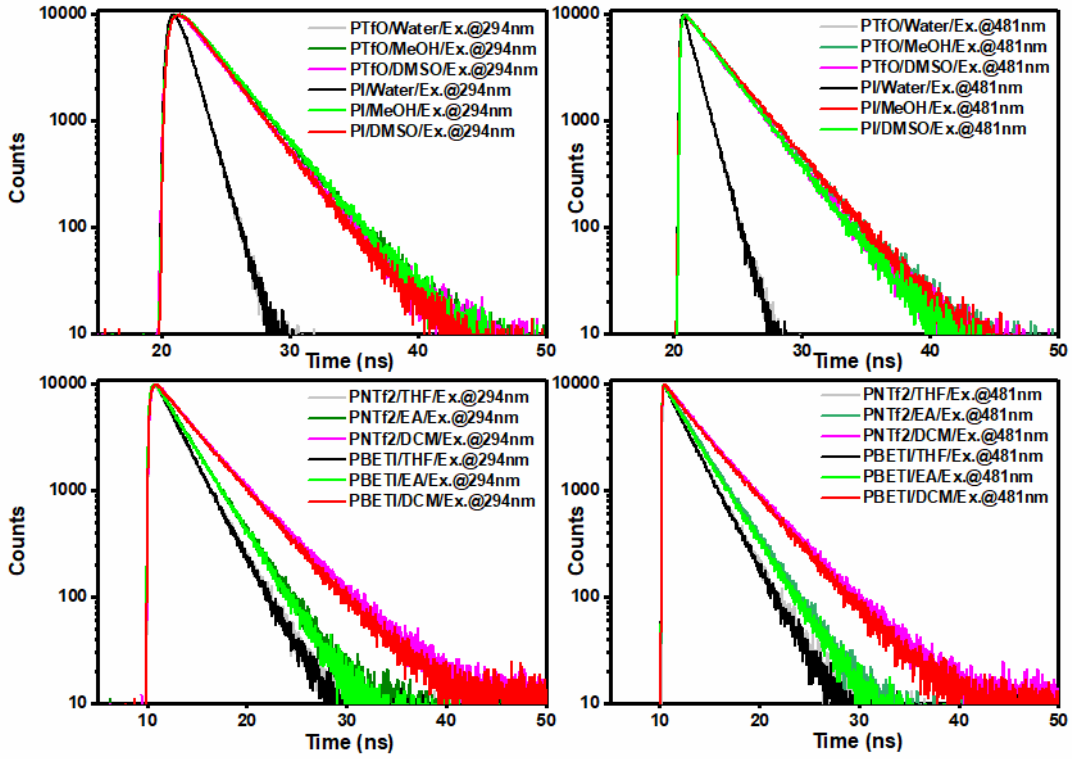

Figure C9. Fluorescence lifetime decay curves for [P][I] and PGUMBOS in different solvents.

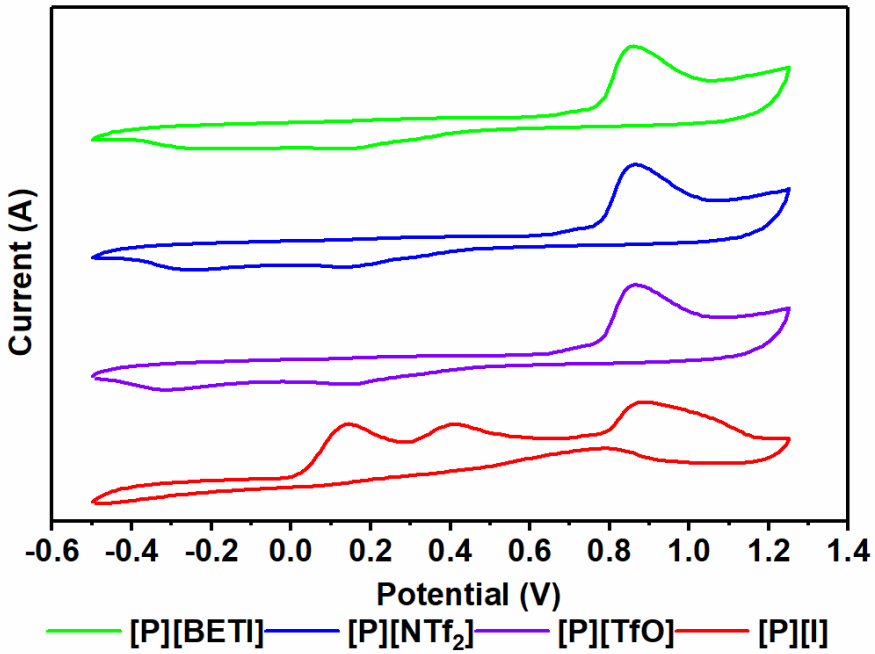

Figure C10. Cyclic voltammograms of [P][I] and PGUMBOS.

APPENDIX D. LETTERS OF PERMISSION

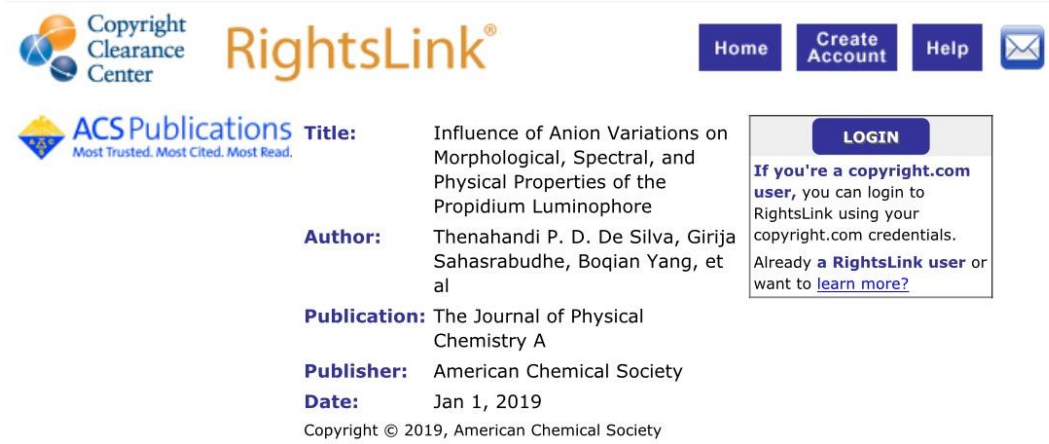

Copyright Clearance Center RightsLink®

Home | Create Account | Help

ACS Publications
Most Trusted. Most Cited. Most Read.

Title: Influence of Anion Variations on Morphological, Spectral, and Physical Properties of the Propidium Luminophore

Author: Thenahandi P. D. De Silva, Girija Sahasrabudhe, Boqian Yang, et al

Publication: The Journal of Physical Chemistry A

Publisher: American Chemical Society

Date: Jan 1, 2019

Copyright © 2019, American Chemical Society

LOGIN

If you're a copyright.com user, you can login to RightsLink using your copyright.com credentials.

Already **a RightsLink user** or want to learn more?

PERMISSION/LICENSE IS GRANTED FOR YOUR ORDER AT NO CHARGE

This type of permission/license, instead of the standard Terms & Conditions, is sent to you because no fee is being charged for your order. Please note the following:

- Permission is granted for your request in both print and electronic formats, and translations.
- If figures and/or tables were requested, they may be adapted or used in part.
- Please print this page for your records and send a copy of it to your publisher/graduate school.
- Appropriate credit for the requested material should be given as follows: "Reprinted (adapted) with permission from (COMPLETE REFERENCE CITATION). Copyright (YEAR) American Chemical Society." Insert appropriate information in place of the capitalized words.
- One-time permission is granted only for the use specified in your request. No additional uses are granted (such as derivative works or other editions). For any other uses, please submit a new request.

BACK | CLOSE WINDOW

VITA

Thenahandi Prasanthi Deepthika De Silva was born in Sri Lanka to Ananda De Silva and Elizabeth De Silva. She grew up in Colombo, the capital of Sri Lanka. Deepthika attended Visakha Vidyalaya, Colombo (high school), and entered the University of Kelaniya, Sri Lanka, to pursue her undergraduate studies in chemistry. After completing her undergraduate studies with the gold medal for chemistry, she started her Master's degree in polymer science and technology at the University of Sri Jayewardenepura, Sri Lanka, while working as a research and development scientist in a world-renowned natural rubber latex products manufacturing company (Dipped Products PLC, Sri Lanka). After receiving first Master's degree at the top of her class, she moved to the USA and enrolled in a second Master's program in chemistry at Sam Houston State University, TX. She graduated from SHSU with multiple prestigious awards for her performance, including research excellence and best thesis awards and at the top of her class. She started her PhD at Louisiana State University in 2013, under the supervision of Prof. Isiah M. Warner. During her PhD, Deepthika received several honors, including the Alumni Association International Student Scholarship for outstanding international student in the areas of academics, engagement, leadership, and diversity (2019), Kiran Allam Award for outstanding research/teaching (2018), and the honor of presenting her research at a number of professional conferences, including ACS, PITTCON, and NOBCChE. Presently, she is the co-inventor of a patent with one first author publication. Two manuscripts based on her research are in submission/preparation.

Publications

1. De Silva, T. P. D.; Sahasrabudhe, G.; Yang, B.; Wang, C.-H.; Chhotaray, P. K.; Nesterov, E. E.; Warner, I. M.: Influence of anion variations on morphological, spectral, and physical properties of the propidium luminophore. *Journal of Physical Chemistry A* **2019**, *123*, 111-119 (*Published as part of The Journal of Physical Chemistry virtual special issue "William M. Jackson Festschrift"*).

2. De Silva, T. P. D.; Sang G. Yuom.; Tamas, G. G.; Yang, B.; Wang, C.-H.; Fronczek, F. R.; Sahasrabudhe, G.; Sterling, S.; Quarels, R. D.; Chhotaray, P.; Nesterov, E. E.; Warner, I. M. Pyrenylpyridines: Sky-blue emitters for organic light emitting diodes (In submission).

3. De Silva, T. P. D.; Sang G. Yuom.; Fronczek, F. R.; Sahasrabudhe, G.; Nesterov, E. E.; Warner, I. M. Pyrene and benzimidazole hybrid multifunctional compounds as novel blue emitters for organic light emitting diodes (OLEDs) (In preparation).

Patents

1. Siraj, N.; Warner, I. M.; De Silva, D. Carbazole-based GUMBOS for highly efficient blue OLEDs. WO 2016112027 A1 (2018).